

AD \_\_\_\_\_

**Award Number:**

W81XWH-11-1-0070

**TITLE:**

Intra-operative Cerenkov Imaging for Guiding Breast  
Cancer Surgery and Assessing Tumor Margins

**PRINCIPAL INVESTIGATOR:**

Guillem Pratx, PhD

**CONTRACTING ORGANIZATION:**

Leland Stanford Junior University

Stanford, CA 94305-2004

**REPORT DATE:** Ráã'åÁG€FH

**TYPE OF REPORT:** N^^|á→ÁU|↑↑áã]

**PREPARED FOR:**

U.S. Army Medical Research and Materiel Command  
Fort Detrick, Maryland 21702-5012

**DISTRIBUTION STATEMENT:**

Approved for Public Release;  
Distribution Unlimited

The views, opinions and/or findings contained in this report are those of the author(s) and should not be construed as an official Department of the Army position, policy or decision unless so designated by other documentation.

REPORT DOCUMENTATION PAGE				Form Approved OMB No. 0704-0188	
Public reporting burden for this collection of information is estimated to average 1 hour per response, including the time for reviewing instructions, searching existing data sources, gathering and maintaining the data needed, and completing and reviewing this collection of information. Send comments regarding this burden estimate or any other aspect of this collection of information, including suggestions for reducing this burden to Department of Defense, Washington Headquarters Services, Directorate for Information Operations and Reports (0704-0188), 1215 Jefferson Davis Highway, Suite 1204, Arlington, VA 22202-4302. Respondents should be aware that notwithstanding any other provision of law, no person shall be subject to any penalty for failing to comply with a collection of information if it does not display a currently valid OMB control number. PLEASE DO NOT RETURN YOUR FORM TO THE ABOVE ADDRESS.					
1. REPORT DATE Rãã'ãAG€FH		2. REPORT TYPE N^^ á→ÁU ↑↑áã]		3. DATES COVERED FÁÇæ´ÁG€F€EËÁG€ÁS~{ÁG€FĞ	
4. TITLE AND SUBTITLE Intra-operative Cerenkov Imaging for Guiding Breast Cancer Surgery and Assessing Tumor Margins				5a. CONTRACT NUMBER	
				5b. GRANT NUMBER W81XWH-11-1-0070	
				5c. PROGRAM ELEMENT NUMBER	
6. AUTHOR(S)  Guillem Pratx, PhD  E-Mail: pratx@stanford.edu				5d. PROJECT NUMBER	
				5e. TASK NUMBER	
				5f. WORK UNIT NUMBER	
7. PERFORMING ORGANIZATION NAME(S) AND ADDRESS(ES)  Ieland Stanford Junior University  Stanford, CA 94305				8. PERFORMING ORGANIZATION REPORT NUMBER	
9. SPONSORING / MONITORING AGENCY NAME(S) AND ADDRESS(ES) U.S. Army Medical Research and Materiel Command Fort Detrick, Maryland 21702-5012				10. SPONSOR/MONITOR'S ACRONYM(S)	
				11. SPONSOR/MONITOR'S REPORT NUMBER(S)	
12. DISTRIBUTION / AVAILABILITY STATEMENT Approved for Public Release; Distribution Unlimited					
13. SUPPLEMENTARY NOTES					
14. ABSTRACT Breast-conserving surgery is standard treatment for breast cancer. However, to be effective, the surgery must remove all malignant tissue. Currently, a significant fraction of BCS patients require additional re-excision surgery to remove residual cancer. This grant aims to develop a system to assess tumor margins during surgery, with the eventual goal of reducing re-excision surgery. This new technology should provide accurate information about the status of the margins in real-time, and therefore guide decision-making during surgery. The system can help surgeons decide when to stop the excision, and, if any, where to remove additional malignant tissue. It is hypothesized that the proposed approach, based on Cerenkov luminescence imaging, will help visualize malignant tissue directly in the operating room by exploiting the specificity of 18F-labeled fluorodeoxyglucose for malignant tissues.					
15. SUBJECT TERMS Breast cancer, surgery, imaging, Cerenkov luminescence					
16. SECURITY CLASSIFICATION OF:			17. LIMITATION OF ABSTRACT	18. NUMBER OF PAGES	19a. NAME OF RESPONSIBLE PERSON USAMRMC
a. REPORT U	b. ABSTRACT U	c. THIS PAGE U			19b. TELEPHONE NUMBER (include area code)
			UU	43	

## Table of Contents

	<u>Page</u>
Introduction.....	4
Body.....	4
Key Research Accomplishments.....	10
Reportable Outcomes.....	10
Conclusion.....	12
References.....	12
Appendices.....	13

## 1. Introduction

Breast-conserving surgery (BCS) is standard treatment for breast cancer. However, to be effective, surgery must remove all malignant tissues. Currently, a significant fraction of BCS patients require additional re-excision surgery due to positive or close margins. This grant aims to develop a system to assess tumor margins during surgery, with the eventual goal of reducing re-excision surgery. This new technology should provide accurate information about the status of the margins in real-time, and therefore guide decision-making during surgery (**Fig. 1**). These technologies are designed to provide a rapid answer such that the surgeon can decide on the spot whether to remove additional tissue to ensure clear margins.

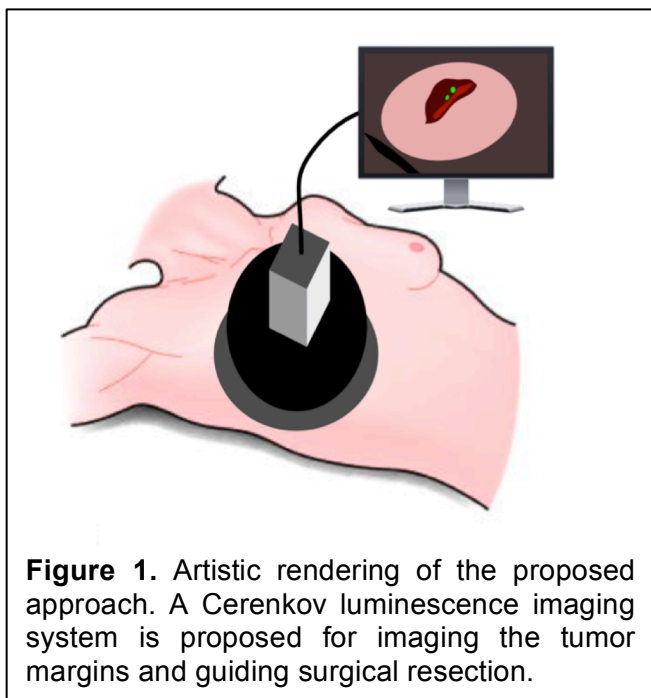


**Figure 1.** Artistic rendering of the proposed approach. A Cerenkov luminescence imaging system is proposed for imaging the tumor margins and guiding surgical resection.

The impact of the proposed research is in the avoidance of unnecessary re-excision breast surgeries, since it is hypothesized that the proposed approach will help visualize compromised margins directly in the operating room. The funded project investigates the use of Cerenkov luminescence imaging for providing sensitive and specific information about the cancer during surgery. Cerenkov luminescence is the natural emission of visible light from radiotracers such as F18-fluorodeoxyglucose (FDG), a positron emission tomography (PET) radiotracer used to identify highly metabolic tumors [1-3]. Since FDG is retained with high specificity by breast cancer tumors, it is hoped that Cerenkov luminescence imaging will provide a simple, sensitive, and inexpensive way to assess focal accumulations of FDG in the operating room, thereby allowing highly malignant tissues to be identified and resected.

## 2. Body

In the three years of this project, the following milestones have been achieved and the following tasks have been completed:

### **Task 1.** Set-up Cerenkov luminescence characterization and quantitation platform.

This first task involved the development of an imaging system for visualizing and measuring minute amounts of radioactive molecules. Two systems were set up and investigated. The first system was designed for imaging very small samples (e.g. tissue sections) and set up by retrofitting an existing bioluminescence microscope (LV200, Olympus) available to us (**Fig. 2a**). The LV200 is designed to image bioluminescence in living cells rather than radioactive tracers such as FDG. Hence, we modified some of the hardware and software on that system to allow for imaging of radioactive tracers. The LV200 is an inverted microscope, comprising an electron-multiplying charge-coupled device (EM-CCD) camera, a high-numerical-aperture lens (40X, 1.3 NA), and live cell imaging capabilities. It is equipped with various filters for fluorescence imaging. The entire microscope is shielded from room lights by a light-tight enclosure. Its hardware specifications allow it to resolve very low amounts of light, such as those produced by Cerenkov from radiotracers.

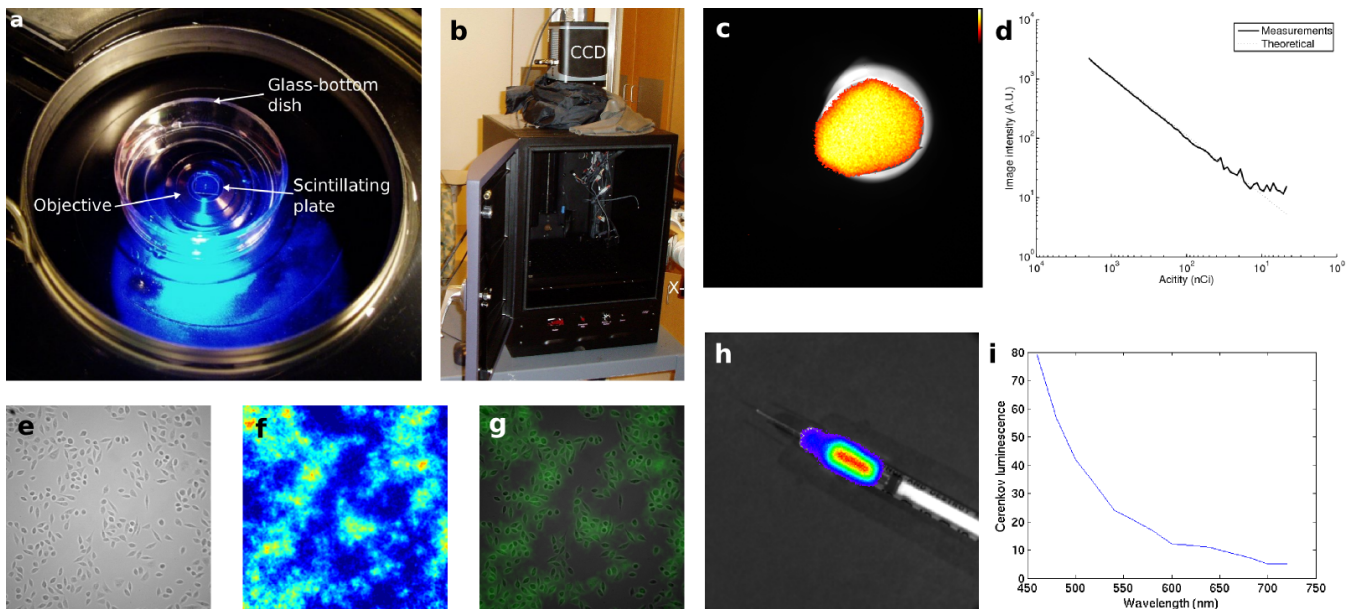


**Figure 2:** (a) Sensitive microscope for measuring Cerenkov luminescence and beta radiation at the cell level. (b) Imaging system for measuring Cerenkov luminescence in larger samples. (c) FDG drop, imaged with the microscope. The color overlay represents the Cerenkov emission while the grayscale image is the brightfield. (d) Image intensity in a region of interest for a drop of FDG as the activity undergoes radioactive decay. (e) Brightfield image of MDA-MB-231 breast cancer cell. (f) Distribution of FDG in the same cells measured using a novel technique, involving placing a scintillator plate in close contact to the cells. (g) Overlay. (h) Cerenkov signal (color) emanating from a syringe filled with FDG, acquired with a custom imaging system. (i) Emission spectrum of Cerenkov luminescence, measured using optical bandpass filters.

The second system was designed for imaging larger specimen, such as primary tumors or small animals. The system was custom-built and is composed of a large light-tight enclosure, a moveable stage, a set of LEDs for taking photographs, and a sensitive EM-CCD camera capable of measuring Cerenkov luminescence (**Fig. 2b**). Software was developed for operating the system, including the capability to move the stage, activate the LEDs, and take images with the camera.

A spectrograph attachment was also set-up for acquiring spectral measurements of Cerenkov luminescence.

## Task 2. Implement combined beta / Cerenkov detection capabilities

As a preliminary experiment, a small drop of FDG (2  $\mu\text{Ci}$ ) was deposited in a glass-bottom dish and imaged with the modified LV200 microscope. Cerenkov luminescence from FDG was clearly visible, showing that the instrument has enough sensitivity to detect Cerenkov luminescence (**Fig. 2c**). As the radioactivity decayed, further images were taken to establish the lowest amount of radioactivity detectable with this set-up, which was found to be approximately 1 nCi (**Fig. 2d**).

A question that arose from these preliminary measurements was what is the smallest resolvable object with this approach. More specifically, could single cells be resolvable using Cerenkov luminescence? To answer this question, breast cancer cells (MDA-MB-231) were cultivated in glass-bottom dishes and incubated with FDG (300  $\mu\text{Ci}$ ). However, no Cerenkov signal could be resolved. The experiments were repeated several times. A computer simulation, performed later, showed that indeed, a single cell could not be resolved with Cerenkov luminescence because (1) the beta particle can travel up to 100  $\mu\text{m}$  in tissue, spreading the signal over a substantial volume; and (2) the signal-to-noise ratio remains low because of the small number of photons emitted by Cerenkov luminescence (on average, 3 photons per decay).

Because of these limitations, we looked for an alternative approach that could visualize uptake of FDG in single cells. This requirement is critical to our research goal, that is, ensuring that no cancer is left after surgery. To solve the two aforementioned issues, we investigated the use of an indirect beta detection scheme. We hypothesized that an inorganic scintillator could (1) reduce the range of the beta particle due to the high density and high atomic number, and (2) increase the signal-to-noise ratio by amplifying the number of optical photons (on average, a beta particle can produce 10,000 photons in suitable scintillator materials). We investigated  $\text{CdWO}_4$  as a suitable material for detecting low amounts of radiotracers such as FDG in cells. To maintain close contact between the cell and the scintillator plate, we cultivated breast cancer cells directly on the scintillator plate. After incubation with FDG, the cells were imaged with the modified microscope. The images showed focal accumulation of FDG in single cells, co-localized with the cells position (**Fig. 2e-g**). This new technique, which we call radioluminescence microscopy, is unique and a significant advance: currently, no other approach can measure and quantify the uptake of a radiotracer in single living cells. These new methods and results were published in *PLOS One* (**Appendix 1**).

**Task 3.** In breast-tissue- and tumor-mimicking phantoms, characterize light and beta propagation and detection

To further characterize Cerenkov luminescence in biological tissues, we developed a computer simulation framework to model the propagation of Cerenkov photons in turbid media (i.e. with high scattering and absorbing properties). The simulation framework used Monte Carlo methods to simulate the history of individual photons. For accurate results, billions of photons need to be simulated, which can require very long run time on large computer clusters. Therefore, we use two different approaches to accelerate computer simulations and make them practical. The first approach used a “roulette” mechanism to keep photons alive even after they have been absorbed. In this scheme, the simulation models packets of photons rather than individual photons, which help reduce the computational requirements tremendously. Furthermore, we implemented a distributed computation software package to run these simulations in a cloud-computing environment. Cloud computing is a new paradigm that allows users of computing resources to rent these resources on demand, for a given amount of time, rather than purchase, install, and maintain large computer clusters on site. Because we did not have access to large computer clusters, cloud computing allowed us to run large optical simulations on 240 nodes in less than two hours. Such simulations would have taken more than a week on a single computer. These new methods and results were published as a research article in the *Journal of Biomedical Optics* (**Appendix 2**).

Using this simulation tool, we were able to better characterize the propagation of Cerenkov light in biological tissues. Using optical properties specific to breast adipose tissue, we simulated the emission of photons from a point source, using the wide spectrum characteristic of Cerenkov radiation. The depth of the emission source was varied from 0 to 1 cm. The photon detector was assumed to be ideal. We found that Cerenkov measurements could be performed up to a depth of approximately 5 mm, which is suitable for assessing disease margins.

The optical emission spectrum of Cerenkov luminescence was also measured using 2 ml of FDG in a syringe using our custom-built imaging system (**Fig. 2h**). The wavelength was found to be proportional to the inverse of the wavelength squared, which confirms the theoretical observations of previous investigators (**Fig. 2i**).

While year 1 was focused on modeling of light diffusion using computer models, in year 2 we performed experiments intended to demonstrate Cerenkov luminescence imaging in breast-mimicking

phantoms. We investigated several materials that have optical properties similar to breast tissue, and found the following mixture to have the best properties: 2% agarose for mechanical strength, 1% intralipid for optical scatter, 17  $\mu\text{M}$  hemoglobin for optical absorption, and 15  $\text{mM}$  NaN<sub>3</sub> for antibiotic and antifungal properties. Using high-melt agarose, we first fabricated a cancerous lesion that contained 200  $\mu\text{Ci}$  of FDG. The mixture was poured in a 1 cm diameter spherical mold, which we fabricated as well. We let the mixture cool down and solidify. We then embedded the lesion in a hemispherical breast-shaped mold filled with low melt agarose. The cancerous lesion is therefore entirely surrounded by “normal” tissue. A color photograph of the phantom is shown in **Fig. 3A**.

We then placed the phantom in a custom Cerenkov imaging system. The system was built in Year 1 and was reported in the 2011 summary report. First, we took a Cerenkov luminescence image of the intact phantom. No Cerenkov signal was detectable because the lesion was too deep. After incision of the phantom, we were able to visualize strong Cerenkov signal emanating from the exposed lesion (**Fig. 3B**). We used this information to surgically remove a piece of phantom tissue, which we believed was the lesion. By taking another Cerenkov image, we were able to verify that the excised

sample was indeed malignant due to the high Cerenkov signal (**Fig. 3C**). We also found that the lesion resection had not been complete: there was significant luminescence coming from the tumor bed. We therefore performed a second resection, after which no further Cerenkov luminescence could be observed in the tumor bed (**Fig. 3D**). We then cut the phantom open to ensure that the entire lesion had been removed. Those experiments were repeated three times to ensure statistical significance.

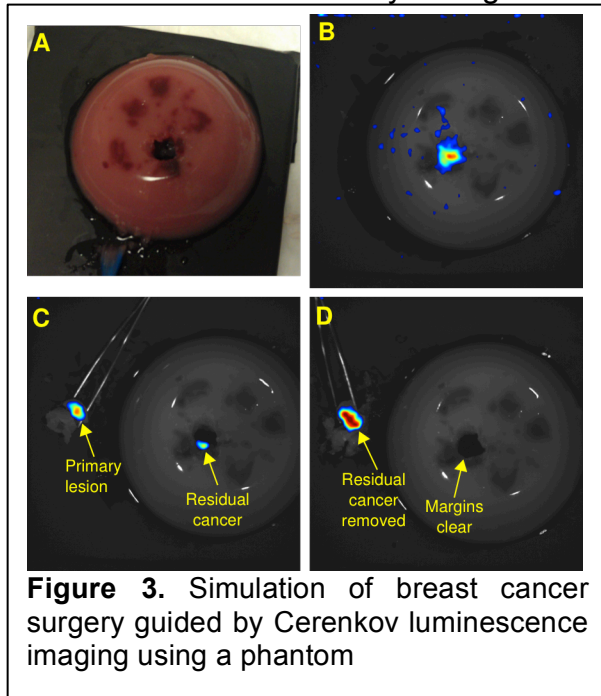


**Figure 3.** Simulation of breast cancer surgery guided by Cerenkov luminescence imaging using a phantom

This experiment helped show that Cerenkov luminescence imaging of FDG is a promising direction for guiding breast cancer surgery. However, we encountered a few difficulties. According to Dr Wapnir, an experienced breast surgeon who provided her expertise, the consistency and mechanical strength of the agarose-based phantoms was significantly different from human breast tissue. Furthermore, we noticed that some of the FDG was able to diffuse away from the

primary lesion and into the surrounding matrix. FDG does not diffuse in vivo because it is retained within the cells. We will investigate other materials that have optical and mechanical similar to breast tissue. In the meantime, we will also report the experiments described here in a biomedical optics journal.

**Task 4.** Design algorithm for estimating signal depth based on combined spectral Cerenkov and beta scintillation imaging

We investigated penetration depth for Cerenkov imaging and direct beta detection with a scintillator. Overall, due to the positron range, direct beta detection with a scintillator was limited to sources of radiation less than 200  $\mu\text{m}$  deep. This makes direct beta detection most suitable for probing shallow tissues, such as residual cancer in the surgical field. Cerenkov luminescence was detected up to a depth of 5 mm (in tissue-mimicking material, given 100  $\mu\text{Ci}$  of activity).

We found that one of the advantages of the direct detection approach was that, due to the physics of scintillation, more photons were produced compared to Cerenkov luminescence. To quantify this

effect, we measured the luminescence intensity using both methods (**Fig. 4A**) and found 30X stronger luminescence using a LSO scintillator.

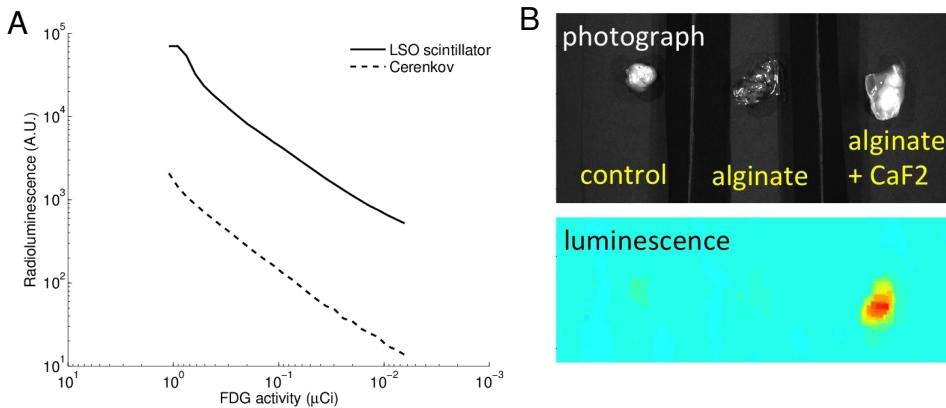


**Figure 4.** (A) Luminescence intensity shown for Cerenkov luminescence and LSO scintillator. The scintillator provides ~30X signal enhancement. (B) Luminescence enhancement shown for a flexible scintillator film, applied directly on an excised tumor specimen.

This effect suggests that we can use a scintillator to amplify low concentrations of FDG in malignant tissue. To this purpose, we fabricated thin, flexible alginate films that embed nano-sized scintillator powders (here,  $\text{CaF}_2\text{:Eu}$ ). To evaluate these scintillating films, we wrapped them around mouse xenograft tumors that were excised 1h after FDG injection. We found that the film lead to a 97% increase in luminescence intensity (**Fig. 4B**). We are planning to use these films to image FDG uptake in excised samples with higher sensitivity.

**Task 5.** Design algorithm for tomographic imaging of tracer distribution in a tissue sample from several projection, using the combined spectral Cerenkov and beta scintillation signal

In the past two years, several methods for performing Cerenkov tomographic reconstructions have

been presented [4,5]. Since these algorithms are well adapted to the final goal of this project, we did not develop new reconstruction algorithms for tomographic reconstruction. We have evaluated one of these algorithms on phantom datasets and have achieved satisfying reconstructions.

**Task 6.** Determine the biodistribution of FDG in breast-cancer mouse xenografts at various time points, and correlate with Cerenkov imaging, autoradiography and pathology

In a preliminary study, we implanted two mice with MDA-MB-231 human xenografts. The mice were injected with FDG, and imaged using standard PET/CT (**Fig. 5A**). After euthanasia, the mice were imaged with Cerenkov luminescence before and after excision of the tumors (**Fig. 5B**). The specimens were frozen and sectioned, then imaged with standard autoradiography (**Fig. 5C**). Last, slices from the same specimen were also imaged using the high-spatial-resolution imaging system (called radioluminescence microscope) developed in year 1 of this project. A full report on this imaging

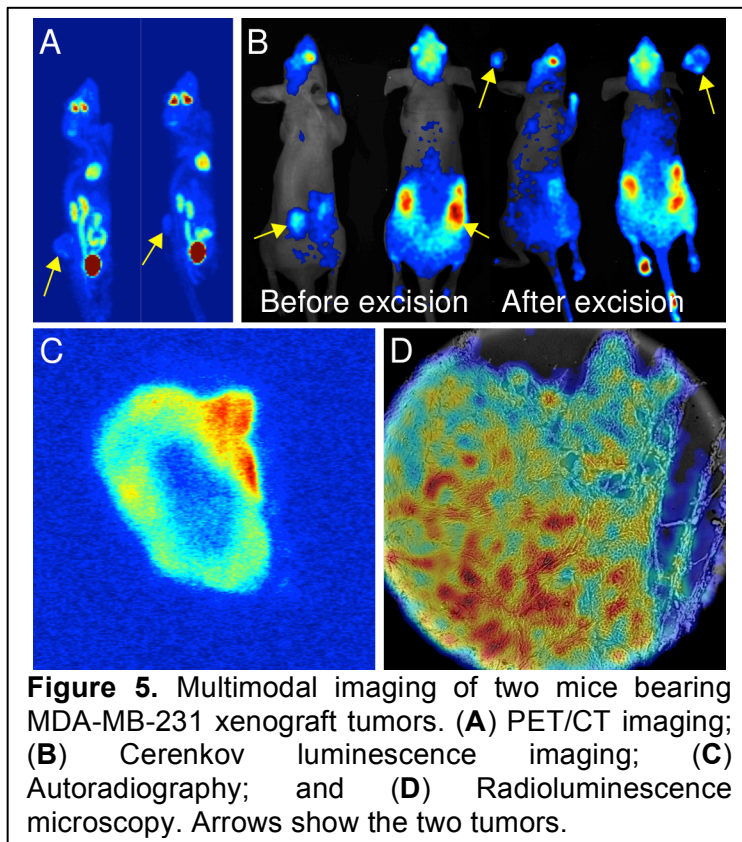


**Figure 5.** Multimodal imaging of two mice bearing MDA-MB-231 xenograft tumors. (A) PET/CT imaging; (B) Cerenkov luminescence imaging; (C) Autoradiography; and (D) Radioluminescence microscopy. Arrows show the two tumors.

radioluminescence microscope) developed in year 1 of this project. A full report on this imaging

system was recently published [6] and is attached as **Appendix 1**. The results of this experiment suggest that Cerenkov luminescence is best adapted for surveying the surgical field, because it allows the visualization of a large area (e.g. **Fig. 1**). The radioluminescence microscope is more suitable to analyzing small excised specimen with high spatial resolution. It can simultaneously visualize radionuclide probe distribution and tissue morphology for accurate assessment of tumor margins with very high spatial resolution. FDG uptake in single cancer cells can be visualized to ensure that the outer rim of tissue on the excised specimen (i.e. the margin) is cancer-free.

In year 2 of this project, we have also developed a new image acquisition method for the radioluminescence microscope system that is more accurate. Rather than using a long exposure (e.g. 5 min), the new method takes thousands of images, each with a short exposure (e.g. 100 ms). This allows single molecules of FDG to be visualized as they decay. This particle counting scheme has two advantages: (1) the spatial resolution is improved because each individual radioactive decay event can be localized with greater precision; and (2) the images have higher quantitative accuracy because each decay event is counted as “one” and not a random quantity. This new imaging scheme was described in a new journal article published in the *Journal of Nuclear Medicine* (**Appendix 3**).

#### **Task 7. Develop bedside tissue characterization platform**

As a first step toward translation, we developed an endoscopic Cerenkov imaging system that is more applicable to clinical human imaging [7]. This system is based on a fiber bundle connected to a sensitive image-intensified CCD camera via an optical coupler (**Fig. 6**). This fiber bundle system is flexible and can be used to visualize Cerenkov luminescence signal at various body sites, including inside cavities such as the gastrointestinal tract. In order to achieve sensitivity, the ICCD camera is run in single photon mode by thresholding individual photon packets. We were the first group to report the possibility of imaging Cerenkov luminescence through an endoscopic device in an article published in the *Journal of Nuclear Medicine* (**Appendix 4**).

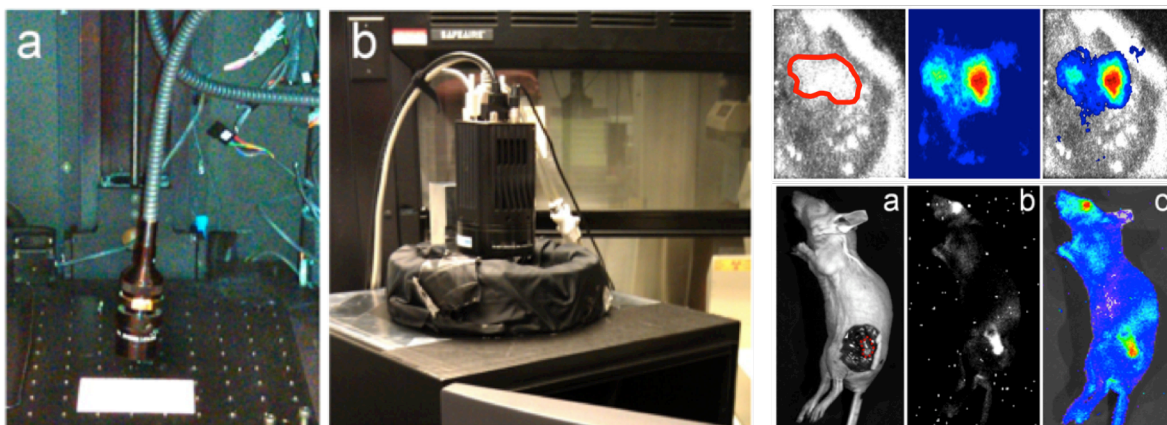


**Figure 6.** Fiberscopic prototype system for clinical imaging of tissue samples. The system (shown on the left) comprises a flexible endoscope that can be brought close to the sample. the system was sued to image a glioma xenograft mouse model (top right) and was compared to a commercial small-animal imaging system (bottom right).

In order to further evaluate the performance of the endoscopy system in living system, we developed murine models of human cancer. We selected a C6 glioma cancer model for this study because cancer xenografts based on this model are more infiltrative and more representative of actual breast cancer, at least from a physical perspective. The C6 glioma model is more likely to result in residual cancer after surgery, which makes it an ideal model for evaluating Cerenkov luminescence imaging. Five mice bearing G6 xenografts were injected with FDG (1 mCi) and imaged with both the

fiberscopic system and a commercial optical imaging system (IVIS 200). The mice were sacrificed prior to starting surgery. The new fiberscopic probe showed that it was possible to visualize Cerenkov luminescence emanating from FDG in the tumor. The boundaries of the xenograft tumor were clearly delineated and displayed some heterogeneity. The image quality obtained with this set-up was comparable to that achievable with a commercial, small animal imaging system. However, it should be noted that small-animal imaging systems do not offer the same flexibility as the new fiberscopic system, which can be bent to access internal cavities. In conclusion, we were able to design and build a prototype imaging system that could one day be used in the clinic for assessment of surgical margins of resection.

**Training:** As part of the comprehensive training plan, I have attended various events to increase my knowledge of breast cancer research. While conducting the research, I have learned how to conduct the following experimental procedures: cancer tissue culture, live cell microscopy, modeling of light in biological tissues, use of radiopharmaceuticals such as FDG, optical instrumentation, EM-CCD cameras, and scintillator physics. Furthermore, during the course of the research, I was able to interact with various researchers with a very diverse set of background and skills. The interactions with my co-mentor Dr. Irene Wapnir (breast cancer surgeon) were particularly useful and productive. I was given the unique opportunity to observe various breast cancer procedures. I also took advantage of the exceptional educational resources available to postdocs on the Stanford campus. For instance, I took several classes highly relevant to this proposal research aims, including “Biophotonics: Light in Medicine and Biology” (EE 331), the Stanford Comprehensive Cancer Research Training Program (see attached certificate), and “Multi-modality molecular imaging” (BIOE 222). Furthermore, I attended a number of conferences on molecular imaging, medical physics, biophysics, and personalized medicine.

### *3. Key Research Accomplishments*

- Development and characterization of two platforms for imaging Cerenkov luminescence both in small and large samples.
- Cerenkov luminescence was observed from decay of FDG in millimeter-sized samples, but could not resolve single cells due to poor spatial resolution and efficiency.
- A new approach, called radioluminescence microscopy, was developed to measure and quantify radiotracer concentration in single cells. The new approach uses a scintillator plate to improve spatial resolution and efficiency compared to Cerenkov luminescence.
- The new approach was used to investigate uptake of FDG by single breast cancer cells.
- A new computer simulation framework was developed for accurately modeling emission and propagation of Cerenkov luminescence in biological tissues.
- Phantom study simulating breast cancer surgery guided by Cerenkov luminescence imaging
- Investigation of Cerenkov imaging at different depths
- New method developed to image single radionuclide decay events with cellular resolution, resulting in higher image quality and accuracy for radioluminescence microscopy
- First demonstration of radioluminescence microscopy for tissue samples, such as tumor specimen excised during breast cancer surgery
- Imaging of breast cancer xenograft models using multiple modalities: PET/CT, Cerenkov luminescence imaging, autoradiography, and radioluminescence microscopy

### *4. Reportable Outcomes*

- Four journal articles published, four currently under preparation / review

**Pratx G** & Xing L, "Monte Carlo simulation of photon migration in a cloud computing environment with MapReduce", *J. Biomed. Opt.* 16(12) pp. 125003, Dec. 2011

**Pratx G**, Chen K, Sun C, Martin L, Carpenter CM, Olcott PD & Xing L, "Radioluminescence microscopy: Measuring the heterogeneous uptake of radiotracers in single living cells", *PLOS One* 7(10), e46285 (2012)

Liu HG, Carpenter CM, Jiang H, **Pratx G**, Sun C, Buchin MP, Gambhir SS, Xing L, & Cheng Z, "Intraoperative imaging of tumors using Cerenkov luminescence endoscopy: A Feasibility Experimental Study", *J. Nucl. Med.* 53(10), pp. 1579-1584 (2012)

**G. Pratx**, K. Chen, C. Sun, C. Carpenter, & L. Xing, "High-resolution radioluminescence microscopy of FDG uptake by reconstructing the beta ionization track", *J. Nucl. Med.*, 54(10) pp.1841-1846 (2013)

CM Carpenter, C Sun, **G Pratx**, K Chen, SS Gambhir, L Xing, "Multiscale PET/Cerenkov Image-Guidance to aid Oncological Resection in an Invasive Prostate Tumor Mouse Model", submitted to Radiology

C.M. Carpenter, X. Ma, H. Liu, Conroy Sun, **G. Pratx**, J. Wang, S.S. Gambhir, L. Xing, Z. Cheng, "Improved Cerenkov Molecular Sensitivity with Beta (minus) Emitting Radiotracers", submitted to J. Nucl. Med.

S. Turkcan, Andrew Ceballos & **G. Pratx**, "First demonstration of 10  $\mu$ m resolution imaging of 18F-FDG", under preparation

A. Natarajan, S. Turkcan & **G. Pratx**, "Multiscale and multimodality imaging of radionuclide probes", under preparation

- Three conference presentations (oral)

**Pratx G**, "Pushing PET imaging to the cellular level: Development of a radioluminescence microscope", *AAPM annual meeting*, August 2013

Carpenter CM, Sun C, **Pratx G** & Xing L, "Multiscale PET/Cerenkov image-guided surgery: Demonstration in an invasive mouse tumor model", *AAPM Annual Meeting*, 2013

**Pratx G**, Chen K, Sun C, Martin LM, Carpenter CM & Xing L, "A new method to measure radiotracer uptake in single living cells", oral presentation, WMIC, 2012 (Selected as a Young Investigator Award semi-finalist)

- One US patent application

Imaging the Heterogeneous Uptake of Radiolabeled Molecules in Single Living Cells, US patent application, 13/492,606

- One travel award to attend WMIC in Dublin (2012)
- One class taught as lead instructor (Mechatronics system)
- Three classes taken (Photonics in Biomedicine, Molecular Imaging, and comprehensive cancer research training program)
- On April 1<sup>st</sup> 2013, started tenure-track position in Radiation Oncology at Stanford University

## 5. Conclusions

The first phase of this project showed that Cerenkov luminescence could be easily detected from FDG, a radiotracer that is preferentially taken up by malignant tumors. We were not able, however, to detect this effect from single isolated cells. To solve this issue, we developed a new technique, termed radioluminescence microscopy, that can visualize, measure, and quantify uptake of radiotracers in single cells. Unlike Cerenkov imaging, radioluminescence microscopy uses a scintillator plate to amplify the ionization signals. Currently, much research effort is dedicated to the characterization of the parameters of single cells, as opposed to large cell populations. This new technique will fill a critical need and reveal the mechanisms that govern the uptake of radiotracers by single cells. Furthermore, this significant advance demonstrates that it may be possible to detect individual cancer cells, which should provide the most sensitive assessment of residual disease.

In the second phase of this project, we have further developed a fiberoptic system designed to image FDG uptake during breast cancer surgery. The strategy for assessing residual disease during breast surgery consists of three steps: before surgery, standard PET/CT is used to evaluate how extensive the disease is, based on the distribution. Then, during surgery, Cerenkov luminescence is used to survey the tumor bed and assess the presence of residual disease. Last, the surface of the excised specimen is imaged with radioluminescence microscopy, which has the ability to visualize cancer down to single cells. The proposed approach will therefore provide real-time assessment of the disease extent at different stages of breast-conserving surgery, i.e. before, during, and after resection of the primary tumor. This multimodal strategy was demonstrated for a phantom study as well as for a murine breast cancer xenograft model.

Following three years of research on Cerenkov luminescence, we can draw the following conclusions. Cerenkov luminescence is a practical and inexpensive way of measuring FDG uptake during surgery. When used with a scintillator, the technique allows sensitive detection of tracer uptake, down to a single cell. Thus this may be a practical strategy for precise assessment of the margins of disease. Sensitivity is limited to approximately 5 mm depth, which means that Cerenkov luminescence imaging is only sensitive to superficial malignancies, which is an advantage for assessing the status of the tissue margins. Last, FDG is a clinically approved radiotracer, which greatly facilitates translation of this proposed imaging technique.

Although Cerenkov luminescence imaging is a promising new path for guiding surgical resection, there are two main issues that remain. The first one is that the method requires the administration of a radioactive tracer and thus it exposes the patient and staff to low level ionizing radiation. Doctors and patients may therefore be reluctant to undergo such procedures (although the use of radiotracers is standard for sentinel lymph node biopsy). The other issue is that  $^{18}\text{F}$  decays with a half-life of 2h, thus imaging is only possible within a 2-3 hour window, which could be problematic for some of the longer surgeries.

## 6. References

- [1] Cerenkov, Pavel A. (1934). "Visible emission of clean liquids by action of  $\gamma$  radiation". *Doklady Akademii Nauk SSSR* 2:451
- [2] Ross HH, "Measurement of beta-emitting nuclides using Cerenkov radiation", *Analytical Chemistry* 41 (10) pp. 1260-1265, 1969
- [3] R Robertson, M S Germanos, C Li, G S Mitchell, S R Cherry and M D Silva, "Optical imaging of Cerenkov light generation from positron-emitting radiotracers", *Phys. Med. Biol.* 54 pp. N355, 2009

- [4] C. Li, G. Mitchell, and S. Cherry, "Cerenkov luminescence tomography for small-animal imaging," *Opt. Lett.* 35, 1109-1111 (2010).
- [5] Z. Hu, J. Liang, W. Yang, W. Fan, C. Li, X. Ma, X. Chen, X. Ma, X. Li, X. Qu, J. Wang, F. Cao, and J. Tian, "Experimental Cerenkov luminescence tomography of the mouse model with SPECT imaging validation," *Opt. Express* 18, 24441-24450 (2010).
- [6] **Pratx G**, Chen K, Sun C, Martin L, Carpenter CM, Olcott PD & Xing L, "Radioluminescence microscopy: Measuring the heterogeneous uptake of radiotracers in single living cells", *PLOS One* 7(10), e46285 (2012)
- [7] Liu HG, Carpenter CM, Jiang H, **Pratx G**, Sun C, Buchin MP, Gambhir SS, Xing L, & Cheng Z, "Intraoperative imaging of tumors using Cerenkov luminescence endoscopy: A Feasibility Experimental Study", *J. Nucl. Med.* 53(10), pp. 1579-1584 (2012)

## 7. Appendices

Attachment 1: **Pratx G**, Chen K, Sun C, Martin L, Carpenter CM, Olcott PD & Xing L, "Radioluminescence microscopy: Measuring the heterogeneous uptake of radiotracers in single living cells", *PLOS One* 7(10), e46285 (2012)

Attachment 2: **Pratx G** & Xing L, "Monte Carlo simulation of photon migration in a cloud computing environment with MapReduce", *J. Biomed. Opt.* 16(12) pp. 125003, Dec. 2011

Attachment 3: **G. Pratx**, K. Chen, C. Sun, C. Carpenter, & L. Xing, "High-resolution radioluminescence microscopy of FDG uptake by reconstructing the beta ionization track", *J. Nucl. Med.*, 54(10) pp.1841-1846 (2013)

Attachment 4: Liu HG, Carpenter CM, Jiang H, **Pratx G**, Sun C, Buchin MP, Gambhir SS, Xing L, & Cheng Z, "Intraoperative imaging of tumors using Cerenkov luminescence endoscopy: A Feasibility Experimental Study", *J. Nucl. Med.* 53(10), pp. 1579-1584 (2012)

# Radioluminescence Microscopy: Measuring the Heterogeneous Uptake of Radiotracers in Single Living Cells

Guillem Pratx<sup>1\*</sup>, Kai Chen<sup>1</sup>, Conroy Sun<sup>1</sup>, Lynn Martin<sup>1</sup>, Colin M. Carpenter<sup>1</sup>, Peter D. Olcott<sup>2</sup>, Lei Xing<sup>1</sup>

<sup>1</sup> Department of Radiation Oncology, Stanford University School of Medicine, Stanford, California, United States of America, <sup>2</sup> Department of Radiology, Stanford University School of Medicine, Stanford, California, United States of America

## Abstract

Radiotracers play an important role in interrogating molecular processes both *in vitro* and *in vivo*. However, current methods are limited to measuring average radiotracer uptake in large cell populations and, as a result, lack the ability to quantify cell-to-cell variations. Here we apply a new technique, termed *radioluminescence microscopy*, to visualize radiotracer uptake in single living cells, in a standard fluorescence microscopy environment. In this technique, live cells are cultured sparsely on a thin scintillator plate and incubated with a radiotracer. Light produced following beta decay is measured using a highly sensitive microscope. Radioluminescence microscopy revealed strong heterogeneity in the uptake of [<sup>18</sup>F]fluorodeoxyglucose (FDG) in single cells, which was found consistent with fluorescence imaging of a glucose analog. We also verified that dynamic uptake of FDG in single cells followed the standard two-tissue compartmental model. Last, we transfected cells with a fusion PET/fluorescence reporter gene and found that uptake of FHBG (a PET radiotracer for transgene expression) coincided with expression of the fluorescent protein. Together, these results indicate that radioluminescence microscopy can visualize radiotracer uptake with single-cell resolution, which may find a use in the precise characterization of radiotracers.

**Citation:** Pratx G, Chen K, Sun C, Martin L, Carpenter CM, et al. (2012) Radioluminescence Microscopy: Measuring the Heterogeneous Uptake of Radiotracers in Single Living Cells. PLoS ONE 7(10): e46285. doi:10.1371/journal.pone.0046285

**Editor:** Xiaoyuan Chen, NIH, United States of America

**Received:** May 29, 2012; **Accepted:** August 28, 2012; **Published:** October 3, 2012

**Copyright:** © 2012 Pratx et al. This is an open-access article distributed under the terms of the Creative Commons Attribution License, which permits unrestricted use, distribution, and reproduction in any medium, provided the original author and source are credited.

**Funding:** Funding for this work was provided by the Department of Defense under grant W81XWH-11-1-0070 and by the National Institutes of Health, ICMIC P50CA114747. The funders had no role in study design, data collection and analysis, decision to publish, or preparation of the manuscript.

**Competing Interests:** The authors have declared that no competing interests exist.

\* E-mail: pratx@stanford.edu

## Introduction

The use of radiotracers to probe biological processes has several advantages over other approaches: radiotracers can be synthesized with chemical composition nearly identical as a given compound of interest; their concentration measured with exquisite sensitivity [1]; and their distribution imaged *in vivo* with positron emission tomography (PET) or single photon emission computer tomography (SPECT) [2,3,4,5]. With the widespread use of radionuclide imaging in research and in hospitals, we need to better understand how properties specific to individual cells (e.g. gene expression, cell cycle, cell damage, and cell morphology) affect the uptake and retention of radiotracers. In particular, disease and therapy can alter cellular mechanisms in a heterogeneous manner; how these alterations affect radiotracer uptake at the single-cell level is currently unknown and of critical importance.

The averaging effect of measuring radiotracer uptake in pooled cell populations can mask important differences between cells belonging to the same population. However, current approaches lack the ability to distinguish radiotracer uptake in individual living cells. For instance, film autoradiographs can be examined with light [6] or electron microscopy [7] to visualize radioactive decay within individual cells but the method is limited to fixed tissues and low energy radionuclides (e.g. <sup>14</sup>C and <sup>3</sup>H). Digital autoradiography techniques (e.g. storage phosphor [8], electronic detection [9,10], thin phosphor layer [11], scintillator [12], and gaseous

chamber [13]) offer higher detection efficiency and dynamic range but poorer spatial resolution (>30 μm), insufficient to resolve individual cells. Likewise, *in vivo* radiotracer imaging and scintillation counting can only measure signals from large cell populations.

Here a new method, termed radioluminescence microscopy, is proposed to measure radiotracer uptake in single living cells. Radioluminescence is the physical process by which ionizing charged particles produce light in certain materials. Due to the short range of beta particles (electrons or positrons), radioluminescence occurs near the location of the radioactive emitter. The range of these particles is further reduced in dense, high-atomic-number materials such as inorganic scintillators. Following this observation, we hypothesized that the radioactivity of single cells could be measured by placing these cells in contact with a scintillator plate and imaging the resulting optical signal using a sensitive microscope with high numerical aperture (NA) and high photon sensitivity. Furthermore, we envisioned that this technique could be applied concurrently with standard fluorescence microscopy because scintillator materials are optically clear in the visible range.

The proposed radioluminescence microscopy set-up consists of a 100 μm-thin CdWO<sub>4</sub> scintillator plate, on which cells have adhered, immersed in a glass-bottom dish filled with cell culture medium (**Figure 1A&B**). The dish is imaged using an inverted

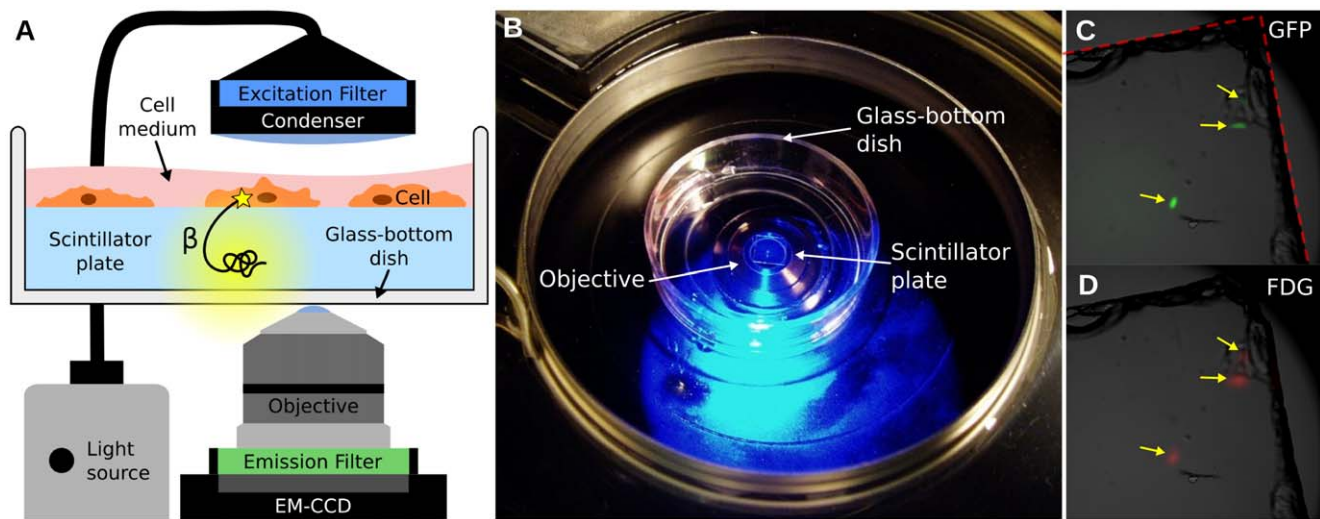


**Figure 1. Overview of the radioluminescence microscope.** (A) Radioluminescence is produced within a scintillator plate following the emission of a beta particle from a radiotracer within a cell (yellow glow). The optical photons are captured by a high-numerical-aperture objective coupled to a deep-cooled EM-CCD camera. Emission and excitation filters used in combination with a light source allow for concurrent fluorescence and brightfield microscopy. (B) Photograph of the system showing a glass-bottom dish containing a scintillator plate immersed in cell culture medium and placed into the inverted microscope. (C) Three GFP-expressing HeLa cells located near the corner of a scintillator plate were localized using fluorescence microscopy (arrows). The edge of the scintillator plate is outlined in red. (D) After incubation with FDG (400  $\mu$ Ci, 1 h), these three cells also produced focal radioluminescence signal coincident with the fluorescent emission. doi:10.1371/journal.pone.0046285.g001

microscope fitted with a high-NA objective and an electron-multiplying charge-coupled device (EM-CCD).

As an illustration of the methods, human ovarian cancer cells (HeLa) expressing the green fluorescent protein (GFP) were imaged after incubation with [ $^{18}$ F]fluorodeoxyglucose (FDG; 400  $\mu$ Ci). Three isolated cells were localized near the corner of a scintillator plate, which is clearly visible on the brightfield micrograph (Figure 1C, dashed red line). Both fluorescence and radioluminescence images displayed focal signal at the locations of the three cells (arrows, Figure 1C&D).

## Results

### Radioluminescence Imaging of FDG uptake in Single Cells

FDG is preferentially taken up and retained within tissues with high glucose metabolism such as malignant tumors [14,15,16]. Measuring FDG uptake in a heterogeneous cell population is of great interest as it may help better understand the heterogeneous metabolic alterations displayed by tumors, and the impact that the tumor microenvironment has on these alterations [17,18]. However, there does not exist a standard method for measuring radiotracer uptake at the single cell level. Therefore, to validate the use of radioluminescence microscopy for FDG imaging, we used a fluorescent glucose analog as a surrogate for FDG uptake in single cells.

After a 1 h glucose fasting period, we incubated human breast cancer cells (MDA-MB-231) for 1 h at 37°C with FDG (400  $\mu$ Ci) and 2-[N-(7-nitrobenz-2-oxa-1,3-dioxol-4-yl)amino]-2-deoxyglucose (2-NBDG; 100  $\mu$ M) [19,20]. After washing the cells, we acquired brightfield, radioluminescence and fluorescence micrographs. We observed good co-localization between the radioluminescence intensity and the cell outline seen on brightfield images (Figure 2A). Furthermore, the radioluminescence intensity varied significantly from cell to cell, indicating heterogeneous uptake of FDG. The single-cell radioluminescence signal was correlated with

2-NBDG fluorescence (Figure 2B,  $p < 10^{-5}$ ,  $r = 0.74$ ). An exact correlation between FDG and 2-NBDG is not expected due to (i) possibly distinct transport mechanisms [21]; and (ii) the inability of 2-NBDG to fluoresce after being metabolized [22]. A line profile through the fluorescence and radioluminescence images confirms co-localization of FDG and 2-NBDG signals (Figure 2C).

### Pharmacokinetic Analysis of FDG Metabolism in Single Cells

The transport and retention of FDG in a cell is influenced by multiple factors, such as the expression of various genes, the density of glucose transporters on the cell surface, the cell size, and the levels and activities of hexokinase and phosphatase enzymes [15]. Under steady-state conditions, the intracellular and extracellular FDG concentrations are in equilibrium. However, rapid changes in the extracellular environment induce a transient response characteristic of the cell's glucose metabolism parameters. These parameters can be estimated using pharmacokinetic modeling techniques. The ability to manipulate a cell's environment is unique to an *in vitro* setting and cannot be easily replicated *in vivo*. Furthermore, pharmacokinetic modeling from PET or gamma counting measurements requires assumptions such as uniform radiotracer concentration and homogeneous rate parameters for each compartment [23]. These assumptions may not be satisfied in practice because each cell in the compartment is characterized by unique parameters. Pharmacokinetic modeling at the single-cell level may provide more optimal characterization of cellular parameters.

To investigate the utility of radioluminescence microscopy for single-cell pharmacokinetic studies, we monitored the uptake of FDG in breast cancer cells (MDA-MB-231) over 8 h. After depriving cells of glucose for 1 h, we added FDG (5  $\mu$ Ci) to their medium and acquired serial brightfield and radioluminescence images every 6 min for 8 h (Figure 3A & Video S1). Although FDG uptake varied significantly from cell to cell, all cells displayed

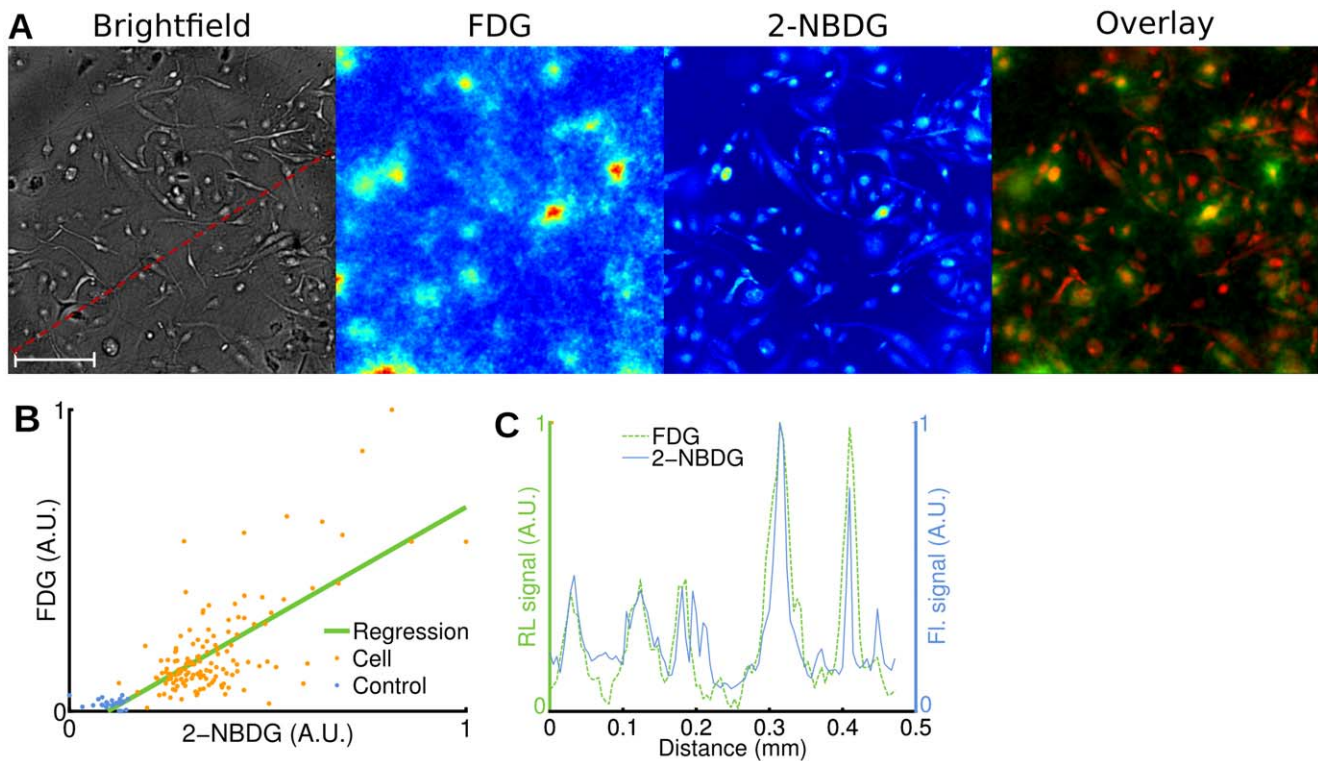


**Figure 2. Radioluminescence imaging of FDG uptake in single cells.** Human breast cancer cells (MDA-MB-231) were deprived of glucose for 1 h, incubated for 1 h with FDG (400  $\mu$ Ci) and 2-NBDG (100  $\mu$ M), and then washed. **(A)** Brightfield (scale bar, 100  $\mu$ m.), radioluminescence (FDG), and fluorescence (2-NBDG) micrographs (Objective: 40X/1.3 NA). Overlay, showing co-localized radioluminescence (green) and fluorescence (red). **(B)** Scatter plot comparing FDG and 2-NBDG uptake, computed over 140 cells (light red dots) and 26 control ROIs (blue dots). The green line was obtained by linear regression (correlation,  $r=0.74$ ). Arbitrary units (A.U.). **(C)** Radioluminescence (FDG) and fluorescence (2-NBDG) intensity shown along a line profile [red dashed line in (A)].  
doi:10.1371/journal.pone.0046285.g002

the same linear increase in radioactivity, followed by a plateau and a slow decrease after 3 h (**Figure 3D**).

We performed two other sets of experiment to highlight efflux of FDG from a cell. Toward this goal, we next subjected breast cancer cells (MDA-MB-231) to conditions known to minimize FDG influx, i.e. competition from glucose (**Figure 3B & Video S2**) and withdrawal of FDG (**Figure 3C & Video S3**). The addition of glucose to the medium (25 mM) at 2 h lead to a strong decline in cell radioactivity (**Figure 3E**) as FDG and glucose competed for the same glucose transporters. Withdrawing FDG from the media of cells that had previously been incubated with FDG (400  $\mu$ Ci, 1 h) also resulted in a similarly fast decrease in cell radioactivity (**Figure 3F**).

The uptake and metabolism of FDG can be mathematically modeled using a two-tissue compartmental model (**Figure 4A**), whose rate constants  $K_1$ ,  $k_2$ ,  $k_3$  and  $k_4$  represent the influx, efflux, phosphorylation, and dephosphorylation of FDG, respectively. Influx of FDG in cells (as shown in **Figure 3A**) was quantified by Patlak analysis. Single-cell time-activity curves measured by radioluminescence microscopy were found consistent with Patlak's model, at least in the early time points: After a short transient period, equilibrium was established and the intracellular concentration of FDG increased linearly with time due to the irreversible trapping of FDG into the cell (e.g. **Figure 4B**). The slope of the linear rise is the product of two terms, namely  $K_1$ , the influx rate, and  $k_3/(k_2+k_3)$ , the fraction of the intracellular FDG irreversibly metabolized.

We found large variations in the Patlak coefficients across the cells that were imaged, indicating that seemingly identical cells process glucose heterogeneously. Furthermore, solving for the pharmacokinetic coefficients  $K_1$ ,  $k_2$  and  $k_3$  showed that  $K_1$  (influx) and  $k_2$  (efflux) were correlated ( $p < 10^{-5}$ ,  $r = 0.89$ , **Figure 4C**) but  $K_1$  and  $k_3$  (phosphorylation) were not ( $p = 0.6$ ,  $r = -0.08$ , **Figure 4D**). Also, the majority of cells stopped accumulating FDG at approximately 3 h and a slow decrease in cell FDG concentration was observed (**Figure 3D**). The non-negligible rate of FDG dephosphorylation ( $k_4$ ) is likely the main factor contributing to that effect. However, dephosphorylation alone should result in the FDG concentration reaching a steady plateau due to equilibration of phosphorylation and dephosphorylation. The slow decrease that was observed instead may have been caused by increased competition from unlabeled 2DG (a byproduct of FDG synthesis) as FDG concentration diminished due to radioactive decay.

We also derived a mathematical model to represent FDG efflux from a cell after withdrawal of FDG (as shown in **Figure 3C**), composed of the sum of a slow and a fast exponential decay. The model was found to be in agreement with radioluminescence measurements of single cells (e.g. **Figure 4E**), confirming that two processes are occurring concurrently at different rates. The first process describes the rapid diffusion of unbound FDG out of the cell (rate  $\lambda_1$ ), whereas the second process involves the slow dephosphorylation of FDG-6-phosphate (rate  $\lambda_2$ ). While the efflux rate was heterogeneous over the cell population studied, we found

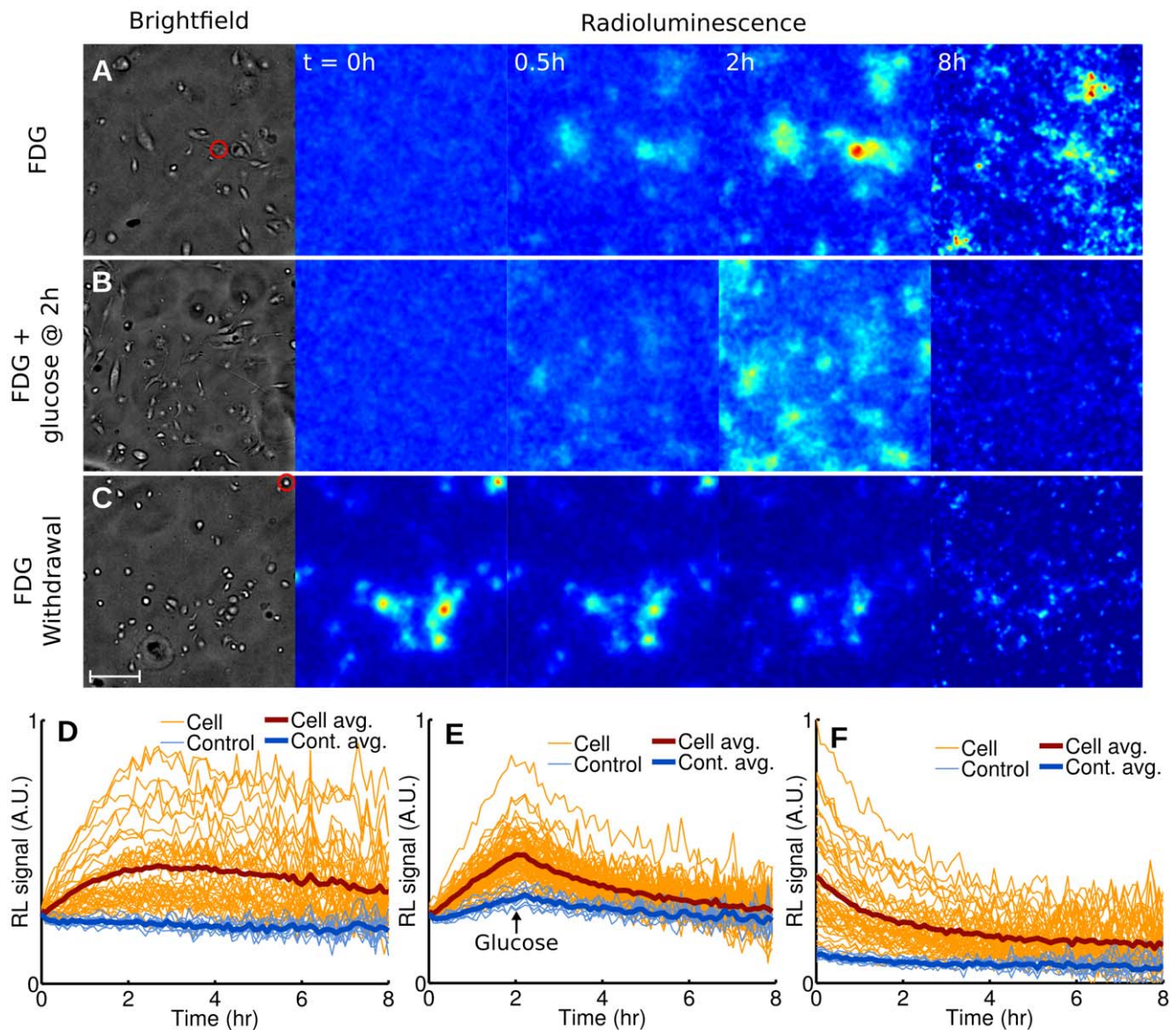


**Figure 3. Dynamic radioluminescence imaging of FDG in single cells.** Micrographs (brightfield and radioluminescence) were acquired every 6 min for 8 h for three experiments. (A) MDA-MB-231 cells are imaged while being incubated with FDG (5  $\mu$ Ci). (B) Glucose (25 mM) is added 2 h after the beginning of the incubation with FDG (5  $\mu$ Ci). (C) FDG is withdrawn at the start of imaging after incubation (1 h, 400  $\mu$ Ci). Scale bar: 100  $\mu$ m. (E–F) Time-activity curves plotted for individual cells (light red lines) and 10 control ROIs manually selected in the background (light blue lines), for all three experiments. The thick red and blue lines represent the average for cells and control ROIs, respectively.  
doi:10.1371/journal.pone.0046285.g003

no significant correlation between the fast and slow components of the decay ( $p=0.9$ ,  $r=-0.02$ , **Figure 4F**).

### Single-cell Characterization of Transgene Expression with a PET Probe

To further validate radioluminescence microscopy, we investigated the uptake of 9-(4-[ $^{18}$ F]Fluoro-3-hydroxymethylbutyl)-guanine (FHBG) in cancer cells that were heterogeneously transfected to express the mutant herpes simplex virus type 1 truncated thymidine kinase (HSV1-ttk). HSV1-ttk can selectively metabolize and trap radiolabeled substrates such as FHBG [24]. Because FHBG has low affinity for mammalian thymidine kinases (TK) and high affinity for viral HSV1-TK, it can be used to image cell trafficking in living subjects with PET [25]. To assess the

expression of the HSV1-ttk transgene with fluorescence microscopy, we built a fusion reporter that also encodes the monomeric red fluorescent protein 1 (mrfp1).

We transfected human cervical cancer cells (HeLa) with the fusion reporter vector encoding HSV1-ttk and mrfp1. Radioluminescence microscopy of FHBG (incubation 2h with 300  $\mu$ Ci) demonstrated focal radiotracer uptake, with individual cells clearly resolvable under 100X magnification (**Figure 5A**). Using fluorescence microscopy, we estimated that 88% of the cells (217/245) had been successfully transfected with the fusion transgene. All of those cells were also clearly distinguishable on the radioluminescence fluorescence image (**Figure 5B**). We also found that 9% of the cells (21/245) had not been transfected and did not produce any fluorescence. These cells did not present a radioluminescence signal, which suggest that they did not retain FHBG. The

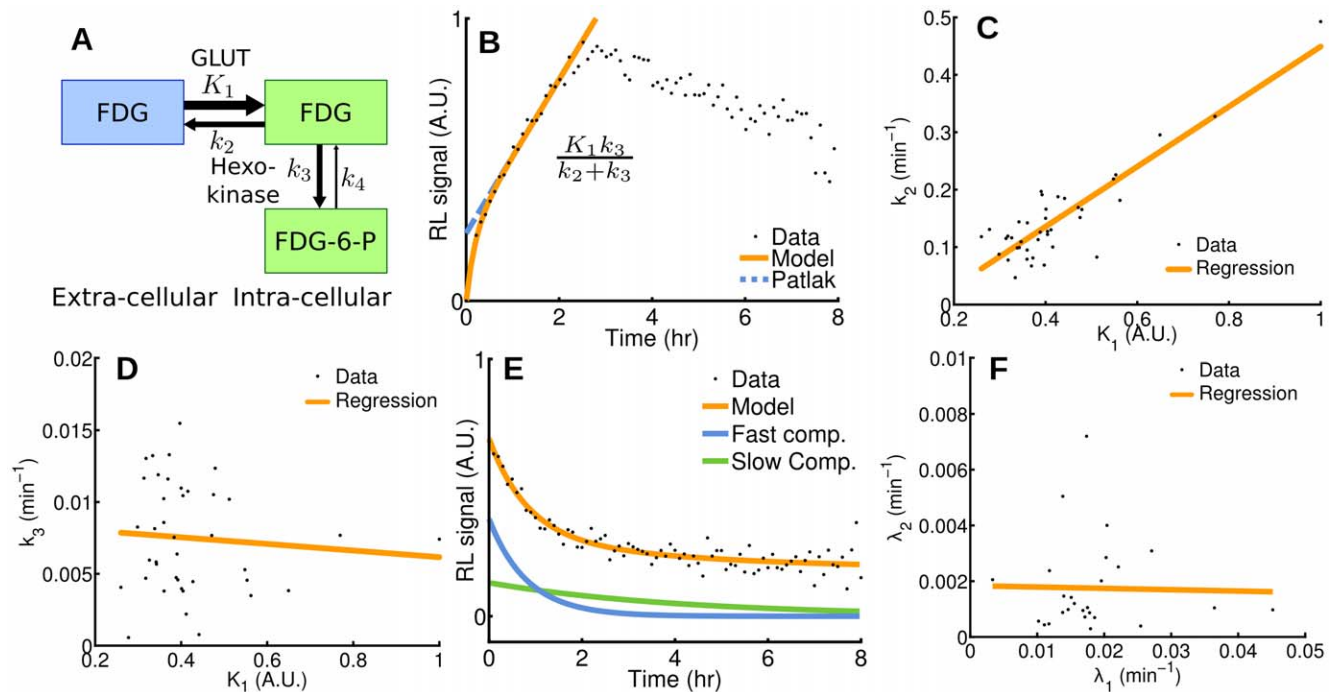


**Figure 4. Pharmacokinetics analysis in single cells.** (A) Two-tissue compartmental model describing FDG pharmacokinetics, including influx ( $K_1$ ), efflux ( $k_2$ ), phosphorylation to FDG-6-phosphate ( $k_3$ ), and dephosphorylation ( $k_4$ ). (B) Patlak analysis modeling FDG influx kinetics for a single cell (highlighted by a red circle in Figure 3A). (C,D) Rate of efflux ( $k_2$ ) and phosphorylation ( $k_3$ ) plotted as a function of rate of influx ( $K_1$ ) for all the cells in the microscope's field of view. (E) Compartmental analysis modeling FDG efflux kinetics from a single cell (highlighted by a red circle in Figure 3C) after withdrawal of FDG, presenting a fast and a slow component. (F) The model for FDG efflux is the sum of a fast and a slow component (rates  $\lambda_1$  and  $\lambda_2$ , respectively), which are plotted for all the cells in the field of view.  
doi:10.1371/journal.pone.0046285.g004

remaining 5% of the cells (7/245) were excluded from the analysis due to ambiguous radioluminescence intensity, mostly due to the proximity of one or more strongly positive cells (e.g. **Figure 5B**, green arrow). Generally, in our system, radioluminescence signals for FHGB-positive and negative cells were more distinctly separated than fluorescence signals for RFP-positive and negative cells (**Figure 5B**, white arrows). A line profile passing through four cells showed good co-localization of RFP and FHGB (**Figure 5D**).

While uptake of FHGB was coincident with RFP fluorescence, fluorescence intensity was not strongly predictive of radioluminescence intensity (**Figure 5C**; correlation,  $r=0.34$ ), indicating that although the HSV1-tk reporter gene expression is required for FHGB uptake, the level of transgene expression is not solely responsible for the extent of FHGB uptake. In a separate experiment, the FHGB substrate displayed no affinity for mammalian TK enzyme: wild-type HeLa cells incubated with FHGB (300  $\mu\text{Ci}$ , 2h) showed no measureable radioluminescence signal (**Figure 5E**).

### Performance Characterization

To investigate the spatial resolution of the imaging set-up, dry FDG aggregates were imaged with the radioluminescence microscope. Brightfield and radioluminescence images displayed good correlation ( $r=-0.79$ ,  $p<10^{-5}$ ; **Figure 6A–G**). From these measurements, we estimated the microscope spatial resolution to be 5  $\mu\text{m}$  (full-width half-maximum).

The sensitivity of the microscope was measured by imaging the decay of a uniform distribution of FDG (2.6  $\mu\text{Ci}$  initially) over 24 hours. The average pixel intensity (expressed as a percentage of the pixel intensity in the first frame) decreased exponentially with time with a half-life consistent with the decay of  $^{18}\text{F}$  (**Figure 6H**).

The relationship between the average pixel intensity and the average activity per area remained linear all the way down to approximately 0.1 fCi/ $\mu\text{m}^2$ . The signal-to-noise ratio (SNR) also decreased with decreasing activity (**Figure 6I**). To visualize image features, a SNR of at least five is required (Rose criterion [26]), which corresponds to a minimum activity area density of 4 fCi/ $\mu\text{m}^2$ . This is equivalent to 1.4 molecules of FDG per  $\mu\text{m}^2$ .

### Discussion

For the first time, radioluminescence microscopy enables the quantification of radiotracer uptake and pharmacokinetics at the single-cell level. Because a similar method does not currently exist, we validated the new approach by comparing single-cell radiotracer measurements against surrogate quantities. Hence, we found FDG uptake to be consistent with fluorescence imaging of a glucose analog (**Figure 2**), with pharmacokinetics characteristic of a two-tissue compartmental model (**Figure 3** and **Figure 4**). Furthermore, in a cell population heterogeneously transfected with a fusion PET/fluorescence reporter, we verified that FHGB uptake was concordant with fluorescence imaging of mrfp1 (**Fig. 5**).

Although radioluminescence microscopy is not yet capable of visualizing intracellular radiotracer distributions, it can measure the radioactivity of single cells provided that those cells are spatially separated on the scintillator plate. Accurate measurements can be achieved with cell-to-cell separation of 10  $\mu\text{m}$  or more. Radioluminescence micrographs can be acquired in 5 min or less using mostly off-the-shelf instrumentation. Commonly used beta emitters such as  $^{18}\text{F}$ ,  $^{131}\text{I}$ , and  $^{64}\text{Cu}$  can be used to produce such images.

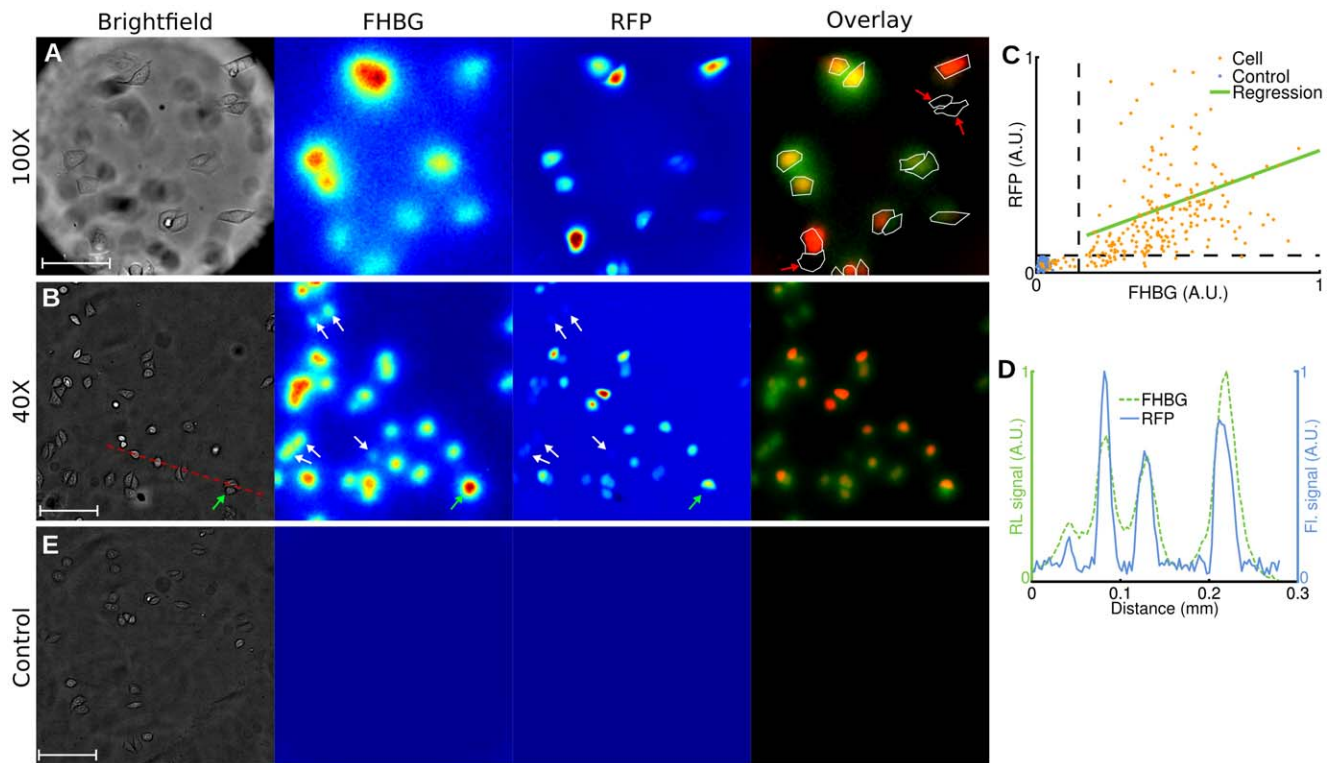


**Figure 5. Radioluminescence imaging of gene expression in single cells.** Human cervical cancer cells (HeLa) transfected with a fusion PET/fluorescence reporter gene were incubated with FHBG (300  $\mu$ Ci, 2 h). (A) Brightfield (scale bar, 50  $\mu$ m), radioluminescence (FHBG), and fluorescence (RFP) micrographs (objective, 100X/1.35 NA). Overlay shows FHBG radioluminescence (green), RFP fluorescence (red), and cell outline segmented from brightfield. Cells negative for RFP are also negative for FHBG (red arrows). (B) Same as (A), but with a 40X/1.3 NA objective (scale bar, 100  $\mu$ m). White arrows indicate cells with weak fluorescence intensity but substantial radioluminescence intensity. The green arrow points to a cell with no RFP expression but ambiguous radioluminescence intensity. (C) Scatter plot of FHBG vs. RFP uptake, computed for 245 cells (light red dots) and 100 control ROIs (blue dots). Arbitrary units. (D) Radioluminescence and fluorescence shown along a line profile [red dashed line in (A)]. (E) Same experiment as (A,B), but using control wild-type HeLa cells (scale bar, 100  $\mu$ m). doi:10.1371/journal.pone.0046285.g005

While radioluminescence microscopy is mainly intended to image tissue culture cells, the method may be applicable to imaging solid tissue sections. However, in the current configuration, it may not provide single-cell resolution for dense tissue section. One solution to this problem is to dissociate the tissue prior to imaging to ensure sufficient separation between cells [27]. We are also currently investigating several approaches to further improve the spatial resolution of the system.

We expect that radioluminescence microscopy will become a useful technique for the precise characterization of radiotracer uptake and pharmacokinetics at the single-cell level. New developments in scintillator research will undoubtedly improve the performance of the technique. Thinner scintillator plates with higher density and light yield will provide better spatial resolution and signal-to-noise ratio. Progress in image processing and calibration techniques will also allow for more quantitative measurements of radiotracer concentration in single cells.

## Materials and Methods

### Microscopy Set-up

Adherent cancer cells were seeded sparsely on 5 mm  $\times$  5 mm  $\times$  0.1 mm plates made of CdWO<sub>4</sub>, a non-hygroscopic inorganic scintillator, with both sides polished (Figure 1A). CdWO<sub>4</sub> has relatively high light yield (12,000–15,000 photon/MeV), high effective atomic number ( $Z_{\text{eff}} = 64$ ), high density (7.9 g/cm<sup>3</sup>), and no significant afterglow. The scintillator plates, loaded with cells,

were placed in microscopy dishes (#0 cover glass, 0.085–0.115 mm, In Vitro Scientific) filled with fresh media (Figure 1A&B). The use of thin scintillator plates and thin-bottom imaging dishes is required to accommodate the short working distance of the microscope objective (200  $\mu$ m).

The imaging dishes were placed in a bioluminescence microscope (LV200, Olympus) outfitted with either a 40X/1.3 NA oil objective (UPLFLN40XO, Olympus) or a 100X/1.35 NA oil objective (UPLAPO00XOI3, Olympus), and a deep-cooled electron-multiplying charge-coupled device (EM-CCD; ImageEM C9100-14, Hamamatsu) (Figure 1 A&B). The C9100-14 CCD is a back-thinned frame transfer device, with a 1024 $\times$ 1024 array of 13  $\mu$ m $\times$ 13  $\mu$ m pixels. The LV200 is also equipped with temperature, humidity, and CO<sub>2</sub> regulation for extended live cell imaging.

Brightfield images were acquired with no EM gain, a neutral-density filter on the excitation, and the emission shutter open. For the 40X magnification, radioluminescence images were taken with an exposure time of 5 min, an EM gain of 251/1200, 2 $\times$ 2 pixel binning, the excitation shutter closed, and the emission shutter open. For the 100X magnification, the exposure time was 20 min and the EM gain 505/1200. We used the brightfield mode to set the microscope into focus. Optimal radioluminescence focus was achieved when the cells displayed sharp positive contrast in the corresponding brightfield image. For fluorescence microscopy, we used a 460 nm/535 nm filter set for 2-NBDG imaging (Chroma

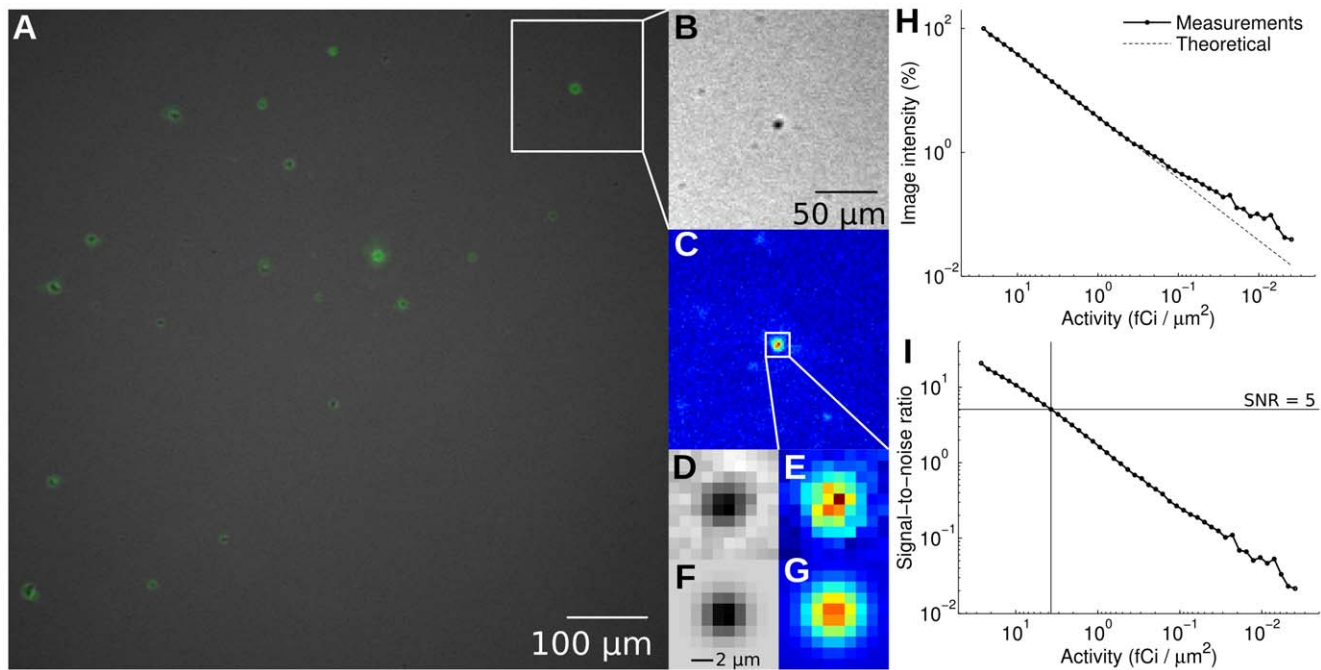


**Figure 6. Performance characterization.** FDG aggregates were obtained by evaporating an aqueous solution of FDG between a scintillator and a glass-bottom imaging dish. **(A)** Fused radioluminescence and brightfield images; **(B)** Brightfield and **(C)** radioluminescence images, magnified; **(D)** Brightfield and **(E)** radioluminescence images, further magnified, focusing on one particular FDG aggregate; **(F,G)** 2-D Gaussian fit of **(D)** and **(E)**, respectively. **(H)** Radioluminescence microscope sensitivity, obtained by imaging the decay of a drop of FDG (2.6  $\mu\text{Ci}$ ) over time. *Solid line*: mean pixel intensity; *Dashed line*: ideal exponential decay for  $^{18}\text{F}$ . **(I)** Per-pixel signal-to-noise ratio, defined as the ratio of the average pixel intensity to the noise standard deviation. The sensitivity of the system is defined here as the amount of activity required per area to achieve a SNR of 5 (Rose criterion). doi:10.1371/journal.pone.0046285.g006

Technology Corp., filter ref. D460/50x and D535/40 m) and a 540 nm/600 nm filter set for RFP imaging (Chroma Technology Corp., filter ref. HQ540/40x and HQ600/50 m).

### Samples Preparation

MDA-MB-231 human breast cancer cells were purchased from the American Type Culture Collection (ATCC, Manassas, VA) and cultured in Leibovitz's L15 medium supplemented with 10% fetal bovine serum. One side of the scintillator plate was coated with fibronectin (10  $\mu\text{g}/\text{ml}$ ) to allow the cells to attach. After the plate had dried, the cells were seeded by placing a 50  $\mu\text{l}$  drop containing  $10^4$  cells on the fibronectin-coated plate. Imaging was performed the following day.

PCR amplification and standard cloning techniques were used to insert the mrfp and tk genes from plasmid pCDNA3.1-CMV-hrl-mrfp-ttk. A lentiviral EF1-gfp vector was purchased from System Biosciences (SBI, Mountain view, CA). The gfp fragment was removed from the vector and replaced with mrfp-ttk. For PCR amplification, different 5' and 3' end primers were used to generate the fusion vector (EF1-mrfp-ttk).

HeLa human cervical cancer and 293T human embryonic kidney cells were purchased from ATCC and cultured in high-glucose Dulbecco's modified eagle medium supplemented with 10% fetal bovine serum. 293T cells were used to produce the lentivirus following standard procedures. HeLa cells were transfected with concentrated lentivirus for 48 h, then trypsinized and seeded onto a scintillator plate coated with fibronectin (10  $\mu\text{g}/\text{ml}$ ) one day before imaging.

### Imaging Protocol

For static imaging of glucose metabolism using combined fluorescence and radioluminescence microscopy, MDA-MB-231 cells were deprived of glucose in Leibovitz's L-15 medium 1 h before incubation with FDG (400  $\mu\text{Ci}$ ) and 2-NBDG (Invitrogen, 100  $\mu\text{M}$ ). FDG was produced at the Stanford radiochemistry facility using an on-site cyclotron. Experiments were conducted shortly after synthesis of FDG to achieve high specific activity.

For dynamic imaging of glucose metabolism, three experiments were conducted: In the first experiment ("FDG"), MDA-MB-231 cells were deprived of glucose for 1 h, after which 5  $\mu\text{Ci}$  of FDG was added to their medium. Imaging started a few minutes later. In the second experiment ("FDG+glucose"), the same procedures were followed. Additionally, 25 mM of glucose was added to the medium at 2 h. In the third experiment ("FDG withdrawal"), the cells were preliminarily incubated in FDG (400  $\mu\text{Ci}$ , 1 h), and imaging started approximately 15 minutes after cell washing.

For imaging of transgene expression with FHBG and RFP, transfected HeLa cells were incubated for 2 h with 300  $\mu\text{Ci}$  of  $^{18}\text{F}$ -FHBG. The FHBG substrate was produced at the Stanford radiochemistry facility using an on-site cyclotron. To gather sufficient cell numbers, five fields were imaged at 40X using radioluminescence, fluorescence and brightfield microscopy. One field was also imaged with a 100X objective.

### Image Corrections and Analysis

Image correction and analysis were performed using MATLAB R2010a (Mathworks, Natick, MA). Radioluminescence micrographs were corrected by subtraction of a dark image, taken with

the same exposure time but with a non-radioactive sample in the microscope. These images were further corrected for field flatness using a flat-field calibration map acquired using a uniform distribution of FDG. Gaussian filtering was applied where appropriate to reduce noise. During long exposures, high-energy photons (gamma rays and annihilation photons) interacted with the CCD and produced hot spots in the image. These hot spots were removed by applying a custom algorithm that can detect sharp features well above neighboring pixels. All radioluminescence images were corrected for radioactive decay. The timestamp of the first acquired image was used as the reference time point.

Fluorescence micrographs were corrected for background effects (filter bleed-through and camera dark noise) by subtracting a dark image taken with a non-fluorescent sample. Field flatness was corrected using a flat-field calibration map.

To measure radiotracer uptake in single cells, circular regions of interest (ROIs; diameter, 24  $\mu\text{m}$ ) were manually placed on the cells using the brightfield micrograph. Similar ROIs were placed in the background as controls. Cell radiotracer uptake was defined as the mean pixel intensity within the ROI of the corrected radioluminescence image. The same ROI analysis procedure was also applied to fluorescence micrographs.

The range of cell motion occurring during the exposure of a single frame is typically too small to result in any significant blurring. However, for extended timelapse imaging studies (1 h or longer), cell motion can no longer be neglected and must be accounted for when analyzing the images. We therefore manually placed circular ROIs on the each cell every 10 frames (i.e. every hour). In between these key frames, we assumed that the cells moved in a straight line.

### Radiotracer Kinetic Modeling

Influx of FDG into glucose-deprived cells was described using the following two-tissue compartmental model:

$$\frac{C(t)}{C_a} = \frac{K_1 k_2}{(k_2 + k_3)^2} (1 - e^{-(k_2 + k_3)t}) + \frac{K_1 k_3}{k_2 + k_3} t$$

where  $C_a$  is the extracellular FDG concentration (assumed to be fixed);  $C(t)$  is the time-dependent intracellular FDG concentration (including free FDG and bound FDG-6-P); and  $K_1$ ,  $k_2$  and  $k_3$  are the rate constants representing influx, efflux, and irreversible phosphorylation of FDG, respectively [23]. For  $t > 1/(k_2 + k_3)$ , the exponential term is becomes negligible. The intracellular and extracellular compartments are then in equilibrium, with the intracellular concentration of FDG rising linearly with time due to irreversible trapping. The slope and intercept of this linear rise are the Patlak coefficients [28]. We used non-linear weighted least-squares curve fitting to estimate the parameters of the model. The fitting weights were adjusted to decrease the contribution of later time points, which have higher noise due to radioactive decay.

Efflux of FDG from cells was modeled using a two-tissue compartmental model:

$$C(t) = a_1 e^{-\lambda_1 t} + a_2 e^{-\lambda_2 t}$$

where  $a_1$  and  $a_2$  are positive coefficients that depend on the initial conditions, and  $\lambda_1$  and  $\lambda_2$  are the eigenvalues of the differential system of equations describing transport of FDG between compartments. The rate constant  $k_4$ , which models the possible dephosphorylation of FDG-6-phosphate (FDG-6-P), was included in this model but assumed to be much smaller than  $k_3$ . Furthermore, due to the large extracellular volume (0.2 ml), the

concentration of FDG in the cell culture medium was assumed to remain negligible after withdrawal of FDG. Under these assumptions, the eigenvalues can be approximated as

$$\lambda_1 = k_2 + k_3 + \frac{k_2 k_4}{k_2 + k_3}$$

and

$$\lambda_2 = \frac{k_2 k_4}{k_2 + k_3}.$$

These rate parameters were estimated by fitting the efflux model to the measured time-activity curves. For cells for which the solution of the fit yielded  $\lambda_1 \approx \lambda_2$  or  $\lambda_2 < 1 \text{ min}^{-1}$ , the efflux curve was fitted with a single exponential function. In the special case of irreversible trapping ( $k_4 = 0$ ), the model is described by a single exponential decay with rate  $\lambda_1 = k_2 + k_3$ .

### Statistical Analysis

Correlation between fluorescence and radioluminescence ROI measurements was computed using the Pearson product-moment correlation coefficient. A p-value of less than 0.01 was considered statistically significant.

### Spatial Resolution Characterization

To evaluate the performance of the radioluminescence microscope, we placed a drop of FDG (10  $\mu\text{Ci}$ ) between the imaging dish and a scintillator plate. Upon evaporation of the aqueous solvent, FDG precipitated into small solid aggregates that could be seen both on brightfield and radioluminescence images. We measured the size of these aggregates by fitting them with 2-D Gaussian functions.

### Sensitivity Characterization

The overall sensitivity of the system was evaluated by imaging the decay of a mixture of glycerol and FDG (2.6  $\mu\text{Ci}$  initially), placed between an imaging dish and a scintillator plate. Radioluminescence images were acquired every 31 min, using an EM gain of 251/1200 and an exposure time of 30 min. Within a large region of interest (370,000 pixels), pixel intensities were normalized to correct for field flatness using the first frame as a reference. The standard deviation of the noise, found to be Gaussian-distributed, was computed in each frame. The per-pixel signal to noise ratio was then defined as the ratio of the average pixel intensity to the standard deviation of the noise. The sensitivity of the system was defined as the activity (area density) required to achieve a signal-to-noise ratio of 5 (Rose criterion [26]).

### Supporting Information

**Video S1 Timelapse imaging of FDG influx kinetics in MDA-MB-231 cells using radioluminescence (left) and brightfield (right) microscopy.** The cells were deprived of glucose one hour prior to imaging. Serial image acquisition was started after adding FDG (5  $\mu\text{Ci}$ ) to the cell culture medium. (MP4)

**Video S2 Timelapse imaging of competition between FDG and glucose uptake in MDA-MB-231 cells using**

**radioluminescence (left) and brightfield (right) microscopy.** The cells were deprived of glucose one hour prior to imaging. Serial image acquisition was started after adding FDG (5  $\mu$ Ci) to the cell culture medium. Additionally, 25 mM of glucose was added to the medium at 2 h. (MP4)

**Video S3 Timelapse imaging of FDG efflux kinetics in MDA-MB-231 cells using radioluminescence (left) and brightfield (right) microscopy.** The cells were preliminarily incubated in FDG (400  $\mu$ Ci, 1 h), and imaging started approximately 15 minutes after cell washing. (MP4)

## References

- Yalow RS, Berson SA (1960) Immunoassay of endogenous plasma insulin in man. *J Clin Invest* 39: 1157–1175.
- Phelps ME (2000) PET: The merging of biology and imaging into molecular imaging. *J Nucl Med* 41: 661–681.
- Nordberg A, Rinne JO, Kadir A, Langstrom B (2010) The use of PET in Alzheimer disease. *Nat Rev Neurol* 6: 78–87.
- Gambhir SS (2002) Molecular imaging of cancer with positron emission tomography. *Nat Rev Cancer* 2: 683–693.
- Dobrucki LW, Sinusas AJ (2009) PET and SPECT in cardiovascular molecular imaging. *Nat Rev Cardiol* 7: 38–47.
- Paltsyn AA, Tumanov VP, Serov GG (1990) Autoradiographic study of cell cultures. *B Exp Biol Med* 110: 1731–1734.
- O'Brien RT, George LA (1959) Preparation of autoradiograms for electron microscopy. *Nature* 183: 1461–1462.
- Johnston RF, Pickett SC, Barker DL (1990) Autoradiography using storage phosphor technology. *Electrophoresis* 11: 355–360.
- Ott RJ, MacDonald J, Wells K (2000) The performance of a CCD digital autoradiography imaging system. *Phys Med Biol* 45: 2011–2027.
- Mettivier G, Montesi MC, Russo P (2003) First images of a digital autoradiography system based on a Medipix2 hybrid silicon pixel detector. *Phys Med Biol* 48: 173–181.
- Chen L, Gobar LS, Knowles NG, Liu Z, Gmitro AF, et al. (2008) Direct imaging of radionuclide-produced electrons and positrons with an ultrathin phosphor. *J Nucl Med* 49: 1141–1145.
- Kanno S, Rai H, Ohya T, Hayashi Y, Tanoi K, et al. (2007) Real-time imaging of radioisotope labeled compounds in a living plant. *J Radioanal Nucl* 272: 565–570.
- Charpak G, Dominik W, Zaganidis N (1989) Optical imaging of the spatial distribution of beta-particles emerging from surfaces. *Proc Natl Acad Sci USA* 86: 1741–1745.
- Cairns RA, Harris IS, Mak TW (2011) Regulation of cancer cell metabolism. *Nature Rev Cancer* 11: 85–95.
- Jadvar H, Alavi A, Gambhir S (2009) 18F-FDG uptake in lung, breast, and colon cancers: Molecular biology correlates and disease characterization. *J Nucl Med* 50: 1829–1827.
- Reivich M, Kuhl D, Wolf A, Greenberg J, Phelps M, et al. (1979) The [18F] fluorodeoxyglucose method for the measurement of local cerebral glucose utilization in man. *Circ Res* 44: 127–137.
- Heimberg H, De Vos A, Vandercammen A, Van Schaftingen E, Pipeleers D, et al. (1993) Heterogeneity in glucose sensitivity among pancreatic beta-cells is correlated to differences in glucose phosphorylation rather than glucose transport. *EMBO J* 12: 2873–2879.
- Pugachev A, Ruan S, Carlin S, Larson SM, Campa J, et al. (2005) Dependence of FDG uptake on tumor microenvironment. *Int J Radiat Oncol* 62: 545–553.
- Yoshioka K, Takahashi H, Homma T, Saito M, Oh KB, et al. (1996) A novel fluorescent derivative of glucose applicable to the assessment of glucose uptake activity of *Escherichia coli*. *Biochim Biophys Acta* 1289: 5–9.
- Yamada K, Saito M, Matsuoka H, Inagaki N (2007) A real-time method of imaging glucose uptake in single, living mammalian cells. *Nature Protoc* 2: 753–762.
- Tseng JC, Wang Y, Banerjee P, Kung A (2012) Incongruity of imaging using fluorescent 2-DG conjugates compared to 18F-FDG in preclinical cancer models. *Mol Imaging Biol* (in press).
- Yoshioka K, Saito M, Oh K, Nemoto Y, Matsuoka H, et al. (1996) Intracellular fate of 2-NBDG, a fluorescent probe for glucose uptake activity, in *Escherichia coli* cells. *Biosci Biotech Biochem* 60: 1899–1901.
- Carson RE (2005) Tracer Kinetic Modeling in PET. In: Bailey DL, Townsend DW, Valk PE, Maisey MN, editors. *Positron Emission Tomography*. London: Springer. 127–159.
- Ray P, De A, Min JJ, Tsien RY, Gambhir SS (2004) Imaging tri-fusion multimodality reporter gene expression in living subjects. *Cancer Res* 64: 1323.
- Yaghoubi S, Barrio JR, Dahlbom M, Iyer M, Namavari M, et al. (2001) Human pharmacokinetic and dosimetry studies of [18F] FHBG: a reporter probe for imaging herpes simplex virus type-1 thymidine kinase reporter gene expression. *J Nucl Sc.* 42: 1225–1234.
- Leidholdt EM, Bushberg JT, Seibert JA, Boone JM (2006) The essential physics of medical imaging 2nd edn. Philadelphia: Lippincott Williams & Wilkins.
- Ensley J, Maciorowski Z, Pietraszkiewicz H, Hassan M, Kish J, et al. (1987) Solid tumor preparation for clinical application of flow cytometry. *Cytometry A* 8: 488–493.
- Patlak CS, Blasberg RG, Fenstermacher JD (1983) Graphical evaluation of blood-to-brain transfer constants from multiple-time uptake data. *J Cerebr Blood F Met* 1: 1–7.

## Acknowledgments

The authors gratefully acknowledge the help of Stanford Nuclear Medicine technologists Christine Fujii, Shawna Kinsella, Luan Nguyen, Matthew Gabriele, and Lincoln Sanders for providing FDG; Stanford postdoctoral fellows Irfan Ali-Khan and Steven Sensarn for assistance with the instrumentation; the Stanford small-animal imaging facility; the Olympus Corporation for providing the LV200; and Dr. Sam Gambhir for providing the vector containing the mrfp-ttk sequence.

## Author Contributions

Conceived and designed the experiments: GP PO LX. Performed the experiments: GP KC CS LM. Analyzed the data: GP CC. Wrote the paper: GP.

# Monte Carlo simulation of photon migration in a cloud computing environment with MapReduce

Guillem Pratx and Lei Xing

Stanford University School of Medicine, Department of Radiation Oncology, 875 Blake Wilbur Drive, Stanford, California 94305

**Abstract.** Monte Carlo simulation is considered the most reliable method for modeling photon migration in heterogeneous media. However, its widespread use is hindered by the high computational cost. The purpose of this work is to report on our implementation of a simple MapReduce method for performing fault-tolerant Monte Carlo computations in a massively-parallel cloud computing environment. We ported the MC321 Monte Carlo package to Hadoop, an open-source MapReduce framework. In this implementation, Map tasks compute photon histories in parallel while a Reduce task scores photon absorption. The distributed implementation was evaluated on a commercial compute cloud. The simulation time was found to be linearly dependent on the number of photons and inversely proportional to the number of nodes. For a cluster size of 240 nodes, the simulation of 100 billion photon histories took 22 min, a  $1258 \times$  speed-up compared to the single-threaded Monte Carlo program. The overall computational throughput was 85,178 photon histories per node per second, with a latency of 100 s. The distributed simulation produced the same output as the original implementation and was resilient to hardware failure: the correctness of the simulation was unaffected by the shutdown of 50% of the nodes. © 2011 Society of Photo-Optical Instrumentation Engineers (SPIE). [DOI: 10.1117/1.3656964]

Keywords: parallel processing; Monte Carlo; optical photon migration; MapReduce; cloud computing.

Paper 11309RR received Jun. 20, 2011; revised manuscript received Sep. 29, 2011; accepted for publication Oct. 10, 2011; published online Nov. 22, 2011.

## 1 Introduction

Researchers have long relied on single-threaded programming for solving computational problems. However, in many applications, the growth of scientific data has outpaced the performance of single-core processors. Furthermore, multicore processors and many-core graphics processing units (GPUs) are now the industry standard for high-performance computing. As a result, scientific computing is inexorably shifting to parallel architectures.

In biomedical applications, the need for high-performance computing is growing as technology evolves toward more accurate imaging and treatment delivery methods. Monte Carlo simulation is the gold standard for modeling complex physical systems, such as photon migration in biological tissue.<sup>1–3</sup> Yet the use of Monte Carlo methods is still hampered by the high computational cost. For instance, it is still not practical to conduct Monte Carlo simulations for planning of photodynamic therapy,<sup>4</sup> especially when using inhomogeneous tissue models.<sup>5,6</sup>

Several distributed approaches have been proposed and implemented to accelerate Monte Carlo simulation of photon transport. Monte Carlo simulation belongs to a class of problems referred to as “embarrassingly parallel”, because little effort is required to split the problem into parallel tasks. Several high-energy Monte Carlo packages have been ported onto computer clusters using tools such as MPI (Refs. 7, 8, and 9) and shell scripting.<sup>10</sup> Light transport in turbid medium has also been ac-

celerated using computer clusters,<sup>11</sup> multiprocessor systems,<sup>12</sup> and field-programmable gate arrays.<sup>13</sup>

In recent years, the graphics processing unit has become a popular platform for running distributed biomedical computations.<sup>14</sup> For simple homogeneous media, GPU computing can dramatically accelerate Monte Carlo simulation of photon migration.<sup>15</sup> Very high acceleration can also be achieved for voxelized and multilayer geometries.<sup>16,17</sup> Acceleration is more modest for complex mesh-based geometries<sup>18</sup> because the distributed calculation of the intersection of a set of rays with a triangular mesh is challenging on the GPU. Monte Carlo simulation for high-energy physics has also been investigated on the GPU.<sup>19,20</sup> Because high-energy particles can undergo a wide range of physical interactions with matter, these implementations use complex optimization strategies for efficient processing.<sup>21</sup>

While parallel processing techniques can accelerate Monte Carlo simulations, practical considerations can be an obstacle to porting existing single-threaded codes onto parallel architectures. To utilize parallel resources efficiently, programmers must be skilled in parallel programming and spend substantial effort optimizing the parallel portion of their code. Parallel code is also harder to debug and maintain. Last, large computer clusters are not always available at a medical institution for running massively parallel applications. All these practical issues are important drawbacks to the development and use of distributed algorithms.

Recently, Internet-scale computation has emerged as a major driver for new parallel processing technologies. Internet companies routinely process very large datasets such as log files,

Address all correspondence to: Guillem Pratx, Stanford University, Radiation Oncology, 875 Blake Wilbur Drive, Stanford, California 94305; Tel: 650 736-0619; E-mail: pratx@stanford.edu

user information, pictures, or videos. Most of these processing tasks are quite simple; however, the size of the input data is large and the computation has to be distributed to hundreds of nodes for practical processing times. Usually, porting these simple tasks onto parallel architectures requires far more effort than required for a single-thread implementation. To address this issue, MapReduce was developed at Google as a new framework to facilitate the development of parallel algorithms.<sup>22</sup>

MapReduce can hide the complexity of parallelization, data distribution, fault-tolerance, and load balancing to the developer, which can focus on developing the actual algorithm. In this programming model, the developer specifies simple tasks which are applied in a distributed fashion to large datasets. MapReduce is also well integrated with existing commercial cloud computing infrastructure. Cloud computing refers to the outsourcing of one's compute resources to third-party companies. Cloud computing providers offer services such as web-based software, data warehousing, and scalable clusters of virtual nodes. In a cloud computing environment, hardware resources are often virtual: computer nodes can be allocated on demand with custom specifications, and can migrate from one physical host to another. In a cluster, the number of nodes can also be scaled in real-time, according to demand for computation.

MapReduce and cloud computing technologies are already widely used in applications such as web crawling and analytics,<sup>23,24</sup> data mining,<sup>25</sup> machine learning,<sup>26</sup> and bioinformatics.<sup>27–30</sup> In this paper, we investigate the use of MapReduce for biomedical Monte Carlo simulation. As a proof-of-concept, we ported an existing photon migration Monte Carlo code to Hadoop, an open-source MapReduce framework, and characterized the performance of this new implementation in a cloud computing environment.

## 2 MapReduce

MapReduce is a programming model for processing large data sets.<sup>22</sup> In this framework, the user specifies two functions called Map and Reduce, respectively. Although neither function is explicitly parallel, many instances of these functions are executed concurrently by the framework. Input data, stored on a distributed storage system, are split by MapReduce into chunks

and distributed to parallel Map tasks for processing (Fig. 1). No communication is possible between Map tasks; however, the outputs of Map tasks can be combined by Reduce tasks.

Data communication between Map and Reduce tasks is handled using key/value pairs (KVPs). In MapReduce, keys and values can be stored in any format, provided that keys can be compared to one another and sorted. While processing input data, Map tasks emit a sequence of intermediary records formatted as KVPs (Fig. 1). Intermediary records that share a common key are assigned to the same Reduce task. A partition function determines how keys are assigned to Reduce tasks.

The role of the Reduce step is to combine intermediary records into the final output. Each Reduce task sequentially reads records associated with a given key. The user specifies how these records are combined. For example, the user can sum the values associated with a common key. The output of the Reduce function is automatically written in KVP format to a distributed storage system, from which it can be retrieved.

Conceptually, Map and Reduce functions can be described as

$$\begin{aligned} \text{map: } v_1 &\rightarrow \text{list}(k_2, v_2) \\ \text{reduce: } (k_2, \text{list}(v_2)) &\rightarrow \text{list}(v_3). \end{aligned} \quad (1)$$

The number of Map and Reduce tasks is set by the user. In general, the number of tasks should be larger than the number of nodes for fine processing granularity. The user can also specify how input data are split and how intermediary records are partitioned.

A feature of MapReduce is its tolerance for hardware failures. In a large cluster, the probability that one or more nodes fail is non-negligible. When a node fails, MapReduce reschedules the compromised tasks onto other nodes in the cluster. A related issue is the heterogeneous performance of worker nodes. For instance, a node in the cluster might be crippled by a defective hardware component and run slowly. Such straggling nodes can substantially reduce the performance of the entire cluster. MapReduce uses a technique called speculative execution to overcome this type of situation. Worker nodes that finish their workload early can attempt to execute clones of tasks in progress

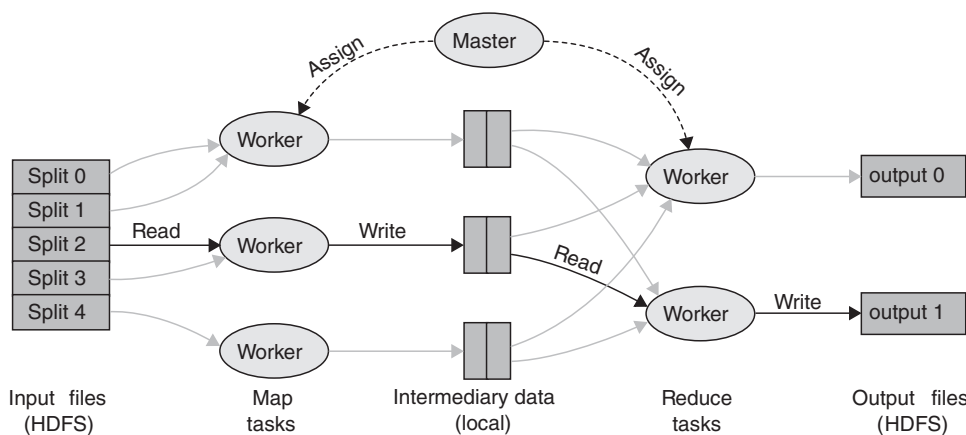


**Fig. 1** An overview of the MapReduce framework. A master node assigns Map and Reduce tasks to worker nodes. Input files are split into chunks, that are processed by independent Map tasks, producing a stream of intermediary key/value records. These records are selectively read by Reduce tasks according to their key, and combined finally into multiple outputs.

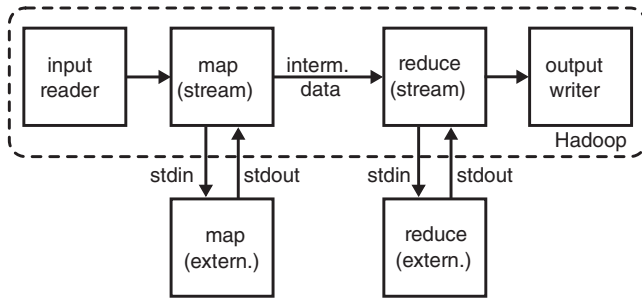


**Fig. 2** A depiction of Hadoop Streaming, a utility that allows users to specify external applications as Map and Reduce functions.

elsewhere in the cluster. A task is considered completed when either its original or clone completes.

The original MapReduce software framework developed by Google is not publicly available but several open-source alternatives exist. Hadoop,<sup>31</sup> maintained by the Apache Software Foundation, is used by Internet companies for large-scale data processing, financial simulations and bioinformatics calculations. Hadoop set a record in 2009 by sorting 1 Petabyte of data in 16.3 h on 3658 nodes.<sup>32</sup>

The Hadoop project includes the Hadoop distributed file system (HDFS), designed for storing extremely large data files (Petabytes and up) on a distributed network of computers, and Hadoop MapReduce, the parallel computation engine. Although Hadoop is written in Java, developers can write jobs in any other programming language using a utility called Hadoop Streaming. Hadoop Streaming implements Map and Reduce functions as interfaces to external user-specified applications (Fig. 2). External Map and Reduce applications communicate with Hadoop Streaming through standard Unix streams. They read input KVPs via standard input (stdin) and write back their output via standard output (stdout). KVPs can be formatted as Text or TypedBytes, which are sequences of bytes in which the first byte is a type code.

### 3 Methods

#### 3.1 Monte Carlo

MC321, a steady-state optical Monte Carlo package for simulating photon migration in homogeneous turbid media,<sup>2</sup> was implemented using Hadoop. In this package, photons are launched in packets with a virtual weight initially set to 1. As the photon packet propagates in the medium, it can scatter or be absorbed. The step size is sampled randomly based on the probability density function of free path. Once the photon packet has reached an absorption site, a fraction of its weight is absorbed and scored into a  $256 \times 256$  detection grid. Next, the photon packet direction is updated by sampling the deflection angle in a manner consistent with anisotropic light scattering. Once the weight of a photon packet drops below 0.01, a Russian roulette test with a 10% survival probability is performed. If the packet survives, its weight is renormalized and the simulation continues. If the roulette test fails, the packet is terminated and a new photon packet may be initiated. No index mismatch or boundary conditions are considered in this simple simulation. Photons that reach the phantom's boundary escape the medium and are automatically terminated.

The MC321 package is a simplified Monte Carlo method that has been utilized to study treatment planning for photodynamic therapy<sup>2</sup> and x-ray luminescence imaging.<sup>33</sup> MC321 cannot model heterogeneous media with spatially-varying optical properties, or photon propagation through material boundaries. However, MC321 shares common features with more accurate packages, such as MCML (Ref. 3) or tMCimg.<sup>5</sup>

#### 3.2 MapReduce Implementation

We propose two novel distributed implementations of MC321 using MapReduce. The first method, termed Monte Carlo event-based processing (MC-EP), splits the production and aggregation of photon histories into Map and Reduce steps, respectively. In this scheme, Map tasks run parallel Monte

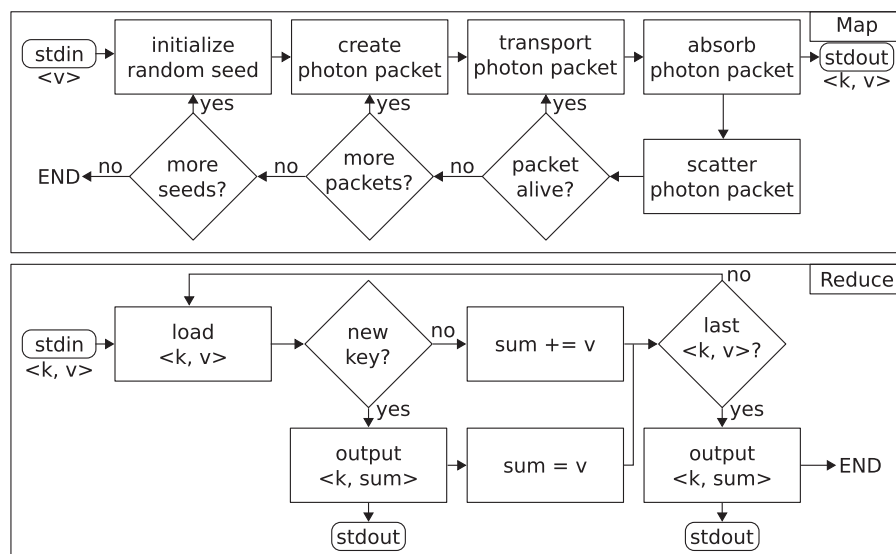


**Fig. 3** An overview of the MC-EP implementation. (Map) For each random seed loaded from stdin, N photon packets are simulated. Individual photon events are written to stdout. (Reduce) The stream of photon events, now sorted by key, are aggregated such that the total photon weight absorbed at every location is computed and written out to stdout.

Carlo simulations, emitting intermediary KVPs every time a photon packet deposits a fraction of its weight into the medium (Fig. 3, top panel). In these intermediary records, the key is an integer index to the nearest two dimensional (2D) detection bin, and the value a floating-point number representing the photon weight absorbed in that bin. These intermediary records are then aggregated by parallel Reduce tasks in the following way: records that share the same key are sequentially read while the corresponding values are accumulated in a local variable. Once all the records for a given key have been processed, the Reduce tasks outputs the cumulated photon weight absorbed in the corresponding detection bin (Fig. 3, bottom panel).

The MC-EP approach is highly flexible because it separates the production and the aggregation of photon histories. In general, little modification is required to implement the MC-EP scheme using an existing single-threaded Monte Carlo code. Streaming photon events to stdout using the KVP format requires minimal code change. (Typically, only a few fwrite statements need to be added to the code.) However, a drawback of the MC-EP approach is that large amounts of intermediary data are produced. To decrease the amount of data exchanged between Map and Reduce steps, intermediary KVPs can be partially aggregated within the Map stage prior to being transferred to the Reduce stage.

In this scheme, termed Monte Carlo histogram-based processing (MC-HP), each Map task outputs a partial scoring array corresponding to the photon histories it has computed. In turn, Reduce tasks accumulate these partial outputs into a complete scoring array. In the MC-HP scheme, intermediary KVPs consist of a unique key (arbitrarily set to 1) and an array of floating-point values representing partial 2D scoring arrays. Most Monte Carlo packages (including MC321) score photon events using a local array, which they write to a disk once the simulation completes. To implement the MC-HP scheme, the developer only needs to write the scoring array to stdout instead of a local file.

For both implementations, Mapper and Reducer are written as standalone C applications. To ensure that Monte Carlo simulations performed in parallel are uncorrelated, a text file containing 10,000 distinct seeds is used as the input of the MapReduce job. The large number of seeds allows Hadoop to execute up to 10,000 parallel Map tasks for fine processing granularity. We also ensure that the Map function, given the same input, always produces the same output. Random number generators (RNGs) that use a system-wide state are problematic with MapReduce because re-execution and speculative execution assume deterministic functions. All communications through UNIX streams use the TypedBytes data format.

The MapReduce implementation of the MC321 Monte Carlo package described in this paper is available for research purpose. The codes can be downloaded from <http://xinglab.stanford.edu/research/downloads.html>.

### 3.3 Computing Environment

Two different Hadoop clusters were used. To develop and debug MapReduce jobs, we set up a pseudo-distributed cluster by installing Hadoop 0.21 on a quad-core computer. Input and output data were stored on a local installation of HDFS. To run and profile large jobs, we allocated a remote Hadoop cluster on Amazon's Elastic Compute Cloud (EC2), using the Elas-

tic MapReduce (EMR) service. EMR is an implementation of Hadoop 0.20 tightly integrated with other Amazon web services, such as the Simple Storage Service (S3).

Map and Reduce applications were compiled remotely on an EC2 node using GCC version 4.3.2, and uploaded onto S3 together with the input random seeds. EMR jobs were submitted from a local computer using a freely-available command-line tool.

### 3.4 System Evaluation

For benchmarking purposes, we simulated the diffusion of a 633 nm laser beam within a turbid 5-cm radius cylinder filled with a 5% milk/95% water mixture.<sup>34</sup> The phantom properties were set as follows: the absorption and scatter coefficients were  $\mu_a = 0.0025 \text{ cm}^{-1}$  and  $\mu_s = 7.8 \text{ cm}^{-1}$ , respectively; the index of refraction was  $n = 1.3$ ; and the anisotropy coefficient was  $g = 0.9$ . The photons were initialized at a single point on the surface of the phantom and directed toward its center. For simplicity, only the  $x$  and  $y$  coordinates of each absorbed photon were scored.

In a first experiment, we compared the original MC321 code against the MC-EP and MC-HP implementations. The benchmark consisted in simulating 100 million photon packets. The original Monte Carlo code was run single-threaded on an Intel Core2 Q9650 CPU with 4 GB of memory. The MapReduce implementations were run on EC2 using 20 high-memory nodes (code-named m2.xlarge). The m2.xlarge node configuration is specially adapted for tasks with large memory requirements, which we found was necessary for the MC-EP implementation. A single m2.xlarge node comes with 17.1 GB of memory, two 64-bit virtual cores with 3.25 EC2 compute units each, and 420 GB of local storage. The output data were downloaded back to a local computer and analyzed with MATLAB.

In a second experiment, the total simulation time was recorded for a variable number of photon packets, ranging from 10 million to 100 billion. At this point, we focused our investigation on the more efficient MC-HP implementation. Twenty high-CPU nodes (codename c1.medium) were used in these tests. These nodes have 1.7 GB of memory, two 32-bit virtual cores with 2.5 EC2 compute units each, and 350 GB of local storage. Each c1.medium node is configured for running four MapReduce tasks simultaneously.

In a third experiment, 100 billion photon packets were simulated using MC-HP on a variable number of nodes, ranging from 1 to 240. The c1.medium node configuration was used. Five thousand Map tasks and one Reduce task were run, providing very fine task granularity and good load balancing. The total run time was recorded and the output of the simulations compared. Because we were not authorized to allocate more than 240 EC2 nodes, we additionally ran the same simulation on the high-CPU extra-large node configuration (c1.xlarge). These nodes have 8 virtual cores with 2.5 EC2 compute unit each, 7 Gb of memory, and 1.7 Tb of local storage. A cluster of 240 c1.xlarge nodes is roughly equivalent to 960 c1.medium nodes.

In a fourth experiment, a 4-node Hadoop cluster was allocated on EC2 and profiled using built-in tools while simulating 300 million photons. The number of Map and Reduce tasks was set to 100 and 1, respectively. Disk I/O, network I/O, and CPU utilization were recorded every minute.

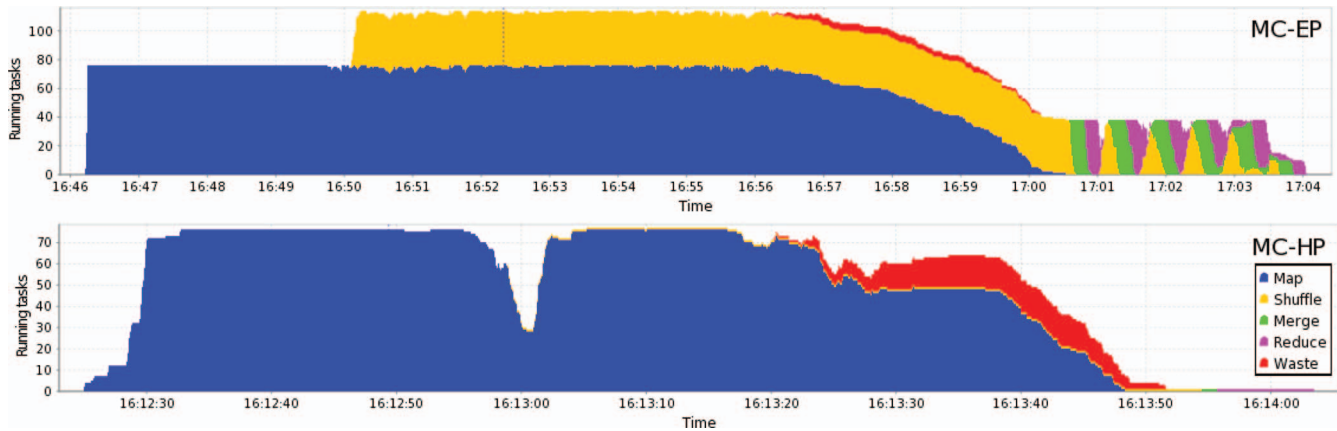


**Fig. 4** MapReduce execution timeline for the MC-EP and MC-HP implementations, showing the number of active tasks at each time point. The MC-EP timeline spans 18 min 09 s, versus 1 min 54 s for the MC-HP timeline. Waste denotes speculative execution.

In a last experiment, 100 million photon packets were simulated with MC-HP on 20 nodes of type c1.medium. After 3 min, a set number of worker nodes were terminated to mimic node failure and test Hadoop's fault tolerance.

## 4 Results

The simulation time for 100 million photon packets is reported for the original and distributed implementations (Table 1). For MapReduce, processing time is defined as the duration of the Hadoop job, not including cluster initialization. For both MapReduce jobs, a timeline was generated from Hadoop log files using Karmasphere Studio (Fig. 4). Overall, MC-EP is slower than MC-HP because MC-EP transfers many intermediary records between Map and Reduce tasks. In MC-EP, shuffle, merge, and reduce tasks represent a significant portion of all tasks (Fig. 4, top). In contrast, MC-HP runs a single reduce task (Fig. 4, bottom).

The output of the MC-HP simulation is compared for a variable number of simulated photon packets, ranging from 10 million to 100 billion [Figs. 5(a)–5(e)]. The output of the MC-HP simulation is virtually identical to that of the original MC321 package. For 10 million photon packets, the relative root-mean-square error between the two photon absorption distributions is lower than  $4.1 \times 10^{-7}$  [Fig. 5(f)]. The discrepancy between the two outputs is due to round-off errors during the conversion of the Reduce output to 10 digit ASCII in the final file. The simulation time also increases linearly with the number of photon packets [Fig. 6(a)]. Note that the curvature of the linear fit is due to the logarithmic scale on both axes.

**Table 1** Simulation time comparison.

	No. Nodes	No. Maps	No. Red.	Node Type	Sim. Time
MC321	1	N/A	N/A	Q9650	28 min 39 s
MC-EP	20	200	200	m2.xlarge	18 min 09 s
MC-HP	20	200	1	m2.xlarge	1 min 54 s

For 100 billion photon packets, the simulation time scaled inversely with the number of nodes [Fig. 6(b)]. On a single dual-core EC2 node, simulating 100 billion photons took 11.2 days, a  $1.8 \times$  speed-up compared with the single-threaded MC321 implementation. The same simulation took only 22 min on 240 c1.xlarge nodes, a  $1258 \times$  speed-up. Nodes based on the c1.xlarge (8 cores) configuration ran the MC-HP simulation 3.3 times faster than c1.medium nodes (2 cores).

To better understand the use of resources, a 4-node Hadoop cluster was profiled while simulating 300 million photons (Fig. 7). The total runtime for this experiment was 20 min. It can be observed that the execution of the simulation was clearly compute-bound because the CPU utilization was maximized on all three slave nodes. Only the CPU capacity of the master node was not fully utilized. The pattern of network I/O was different for nodes running Map tasks only and nodes running both Map and Reduce tasks. In MC-HP, Map tasks are data producers; they input little data (the random seeds) but output large amounts of

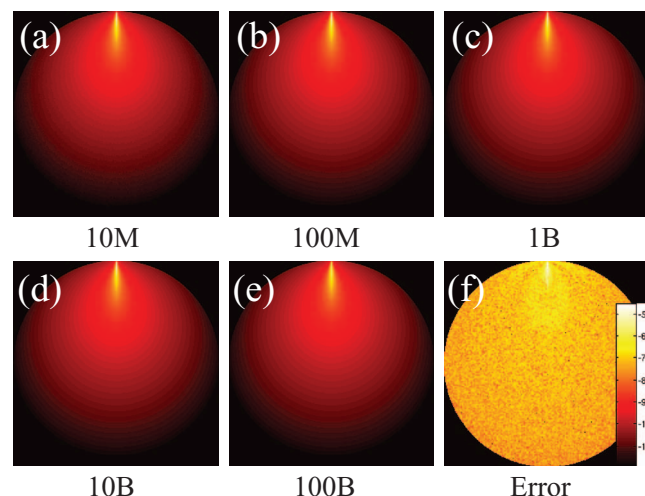


**Fig. 5** (a)–(e) Output of the MC-HP simulation for a variable number of photon histories ranging from 10 million to 100 billion, shown on a base-10 logarithmic scale. (f) Error between the original Monte Carlo package and the MapReduce implementation, shown for 10 million photon histories on a base-10 logarithmic scale.

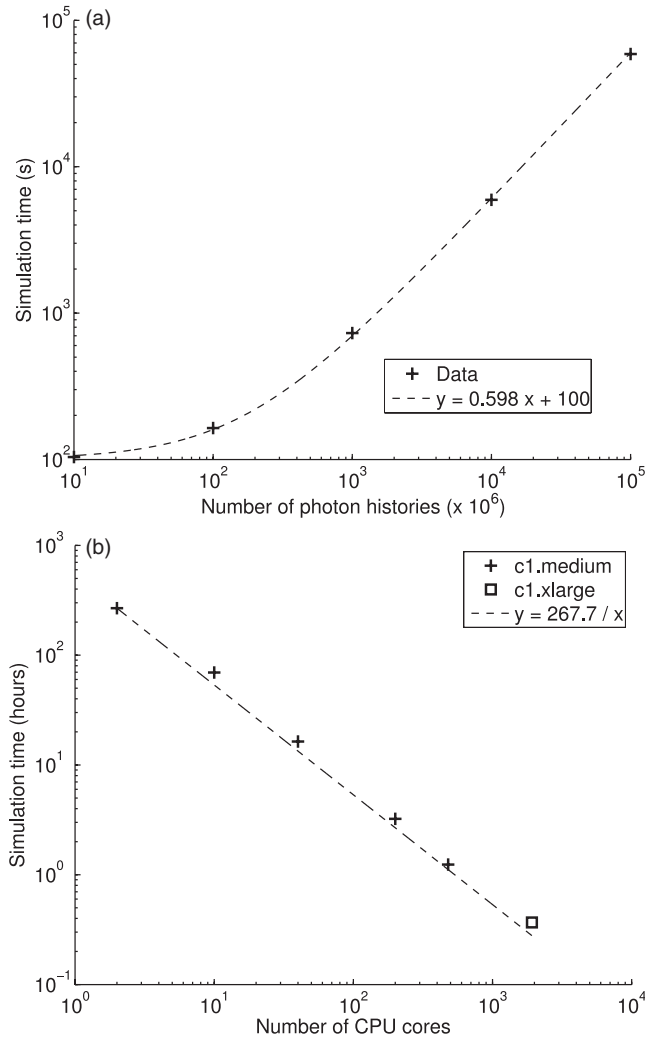


**Fig. 6** (a) MC-HP simulation time for a varying number of photon histories. Dashed line: least-square linear regression ( $r^2 = 0.9998$ ). The curvature of the linear fit is due to the logarithmic scale. (b) MC-HP simulation time for a varying number of CPU cores. Dashed line: ideal inverse scaling of the single-node simulation time ( $r^2 = 0.98$ ).

data (the scoring arrays). In contrast, Reduce tasks are data consumers: they continuously receive data from Map tasks, which they only write to HDFS at the end of the simulation.

Hadoop's fault tolerance was also evaluated by shutting down 1 and 10 worker nodes, respectively, during the simulation of 100 million photons on 20 nodes. The termination of these nodes did not prevent Hadoop from successfully completing its job, provided that the master node was kept alive. Upon node failure, EMR allocated new nodes dynamically and relaunched failed Map and Reduce tasks. The output of the Hadoop simulation with some nodes terminated was identical to that obtained by running the simulation with no failure. The failure of 1 and 10 nodes lengthened the total simulation by 15 and 18 min, respectively.

## 5 Discussion

While MapReduce is often used to crunch large datasets such as website logs, we demonstrated that it is also well suited for



**Fig. 7** Resource profile showing I/O and computing during simulation of 300 million photons on a 4-node Hadoop cluster.

computationally-demanding Monte Carlo simulations. MapReduce's architecture is largely decentralized for efficient data processing on large clusters. Even with 240 nodes, the performance of the MC-HP implementation scales linearly with the number of CPU cores [Fig. 6(b)], showing few signs of diminishing returns. On average, the simulation times were within 12% of the ideal inverse scaling [Fig. 6(b), dashed line]. This result suggests that, if needed, the MC-HP implementation could run on many more nodes without suffering from interconnect latencies and limited network throughput.

The MC-HP simulation also scaled linearly with the number of photon packets simulated. When the number of photons was incremented from 10 million to 100 billion, the simulation time followed a linear trend [Fig. 6(a),  $r^2 = 0.9998$ ]. Each incremental one million photons can be simulated on 20 nodes in 0.6 s. Furthermore, the computation overhead, which consists of cluster initialization, task distribution, and data reduction, is on the order of 100 s, which is negligible when billions of photon packets are simulated [Fig. 6(a)].

By combining the information from the first and second experiment, the performance of the MC-HP implementation can be better characterized. The throughput and latency were found to be 85,178 photons per node per second, and 100 s, respectively. In a separate experiment (data not shown), latency was found to be independent of the number of nodes.

Hadoop also proved to be a highly reliable framework that could withstand the accidental failure of 50% of the worker nodes. Upon node failure, EMR allocates new nodes to replace failed ones. Currently, the process of resizing a running Hadoop cluster on EC2 is rather slow, requiring around 15 min, but a substantial effort is under way to improve the efficiency of the process. There also exist simpler implementations of MapReduce that do not resize the cluster, but rather redistribute failed tasks to nodes not affected by the failure.

A drawback of cloud computing is that a virtual cluster must be allocated on the cloud before running a job, a process that involves deploying a large number of operating system images on physical computers. Such initialization contributes to the overall execution time by increasing the latency, especially for very large cluster configurations. The solution we adopted consisted in keeping our virtual Hadoop cluster alive after the completion of its first job, such that it would remain available for other jobs.

A word should also be said about the cost of performing Monte Carlo simulation in a commercial cloud computing environment. As of August 2011, the price of Amazon's EC2 nodes ranges from \$0.025/h for micronodes to \$2.28/h for quadruple extra-large nodes. Most of the simulations presented in our study were performed on high-CPU medium nodes, which are priced at \$0.19/h. Hence, large-scale simulations, such as those with  $10^{11}$  photon packet histories [Fig. 6(b)], can cost a few hundred dollars to run. Cloud computing is ideal for research institutions that do not have a sufficient demand to maintain a full-size cluster on site. Furthermore, cloud resources have very low downtime. The main alternatives to cloud computing is the operation of a dedicated cluster, a solution currently used by many research groups. This approach has a few advantages, namely the absence of a virtualization layer and better control over the hardware. However, energy, maintenance, and storage costs can be significantly higher. Furthermore, the lack of elastic scaling results in under- or overutilization of compute resources.

MapReduce is highly optimized for data-intensive processing tasks, such as indexing web pages or mining large datasets. It uses a loosely-coupled distributed memory system, which does not allow parallel tasks to communicate with one another directly. By its design, MapReduce is suboptimal for compute-bound tasks or for tasks that require frequent internode data exchange, such as, for instance, iterative image reconstruction. In MapReduce, internode communication can be achieved by reducing the Map outputs with Reduce tasks, and splitting these data again using a new set of Map tasks. For tasks with a large amount of internode communication, this mechanism may be less efficient than a shared memory approach. For instance, GPUs provide on-chip memory shared by threads in a same block, and global memory shared by all threads. As a result, GPU threads can exchange data efficiently. Many scientific computation strategies have used the GPU's fast shared memory to achieve impressive performance.<sup>33</sup> Furthermore, GPU can access global memory with nearly 5-fold higher bandwidth than state-of-the-art CPUs: For instance, the memory bandwidth of a Tesla C2050 GPU is 144 GB/s, versus 32 GB/s for an Intel Xeon X5650 CPU. However, the peak performance of the two architectures should be compared with caution because the GPU's peak memory bandwidth is only achieved when memory transfers are fully coalesced (i.e., they occur in continuous 128-bit chunks). For random memory accesses (such as scoring

during a Monte Carlo simulation), this is seldom the case and the achieved bandwidth can be lower than the peak theoretical value. At this time, the use of a distributed memory system such as MapReduce for scientific applications other than Monte Carlo is still being investigated.<sup>35</sup>

The performance of the MC-HP implementation can be put into perspective by comparing it against other published simulations of photon migration in homogeneous media (Table 2). These performance figures should be compared with caution because of the diverse set of parameters used in these studies. The speed of the simulation can be affected by a number of parameters, including the RNG, the optical properties, the size of the scoring grid, and the roulette parameters. With this caveat in mind, the cloud-based approach provides speed-up of the same order of magnitude as its GPU-based counterparts (Table 2). A GPU platform has several advantages for Monte Carlo simulation, such as built-in hardware-accelerated arithmetic functions, no thread-switching overhead, a compact form factor, and the relatively low price of the hardware.<sup>14</sup>

However, one issue with GPU computing is that many threads share access to the same memory. Hence, race conditions may arise when two or more threads attempt to write to the same grid element, since only one thread can write to a given memory location on a clock cycle. This situation occurs most frequently in high fluence regions, such as near the light source, and is less problematic in low-fluence regions.<sup>16</sup> GPU atomic operations can be used to serialize the memory writes when needed, at the cost of slower memory access. For instance, the MCX package is four times slower when such atomic operations are used (Table 2). A variant of MCX (mcx\_cached) and the GPU-MCML package use a different approach to mitigate race condition issues: The high-fluence region of the scoring array is cached in fast shared memory and accessed atomically, while the low-fluence region is stored in global memory. Use of fast shared memory reduces the penalty associated with atomic operations since fewer threads access the grid at any time, and shared memory has much lower latency than global memory. In our MapReduce implementation, each task allocates its own detection grid locally, which avoids data write hazards. Local detection grids are combined using parallel Reduce tasks.

Additionally, MapReduce offers better scalability than GPUs. To achieve higher photon throughput, multiple GPUs must be employed and integrated into a cluster.<sup>17</sup> The software must be adapted to provide inter-GPU and intercomputer communications, which adds another layer of complexity. In contrast, the number of nodes in a MapReduce cluster can be scaled by modifying a single parameter. However, if used intensively, a GPU cluster can be more economical over time than computing capacity purchased on demand from a cloud computing operator.

In the context of a Monte Carlo simulation, a loosely-coupled parallel architecture such as a Hadoop cluster has some advantages over a GPU. The GPU architecture is based on a single-program multiple-data programming model which penalizes diverging threads. Briefly, a GPU is composed of several multiprocessors, each of which processes parallel threads in batches called warps. Even though threads within a warp can follow diverging paths, a GPU multiprocessor can only issue one instruction per clock cycle. Hence, the execution of diverging threads is serialized: only those threads programmed to

**Table 2** Comparison of various photon migration Monte Carlo codes, according to the following parameters: RNG; the absorption and scatter coefficients  $\mu_a$  and  $\mu_s$ , respectively; the size of the scoring grid; the acceleration platform; the photon throughput  $T_{\text{acc}}$  and  $T_{\text{ref}}$ , expressed in photons/ms, for the accelerated and reference (CPU) platform, respectively; and the speed up achieved.

Implementation	RNG	$\mu_a(\text{cm}^{-1})$	$\mu_s(\text{cm}^{-1})$	Scoring grid	Platform	Threads	$T_{\text{acc}}$	$T_{\text{ref}}$	Speed-up
MC-HP	RAN3	0.0025	7.8	$256 \times 256$	EC2 cloud	3,840	75,471	60	1258
MCX (atomic) (Ref. 16)	LL5	0.05	10.1	$60 \times 60 \times 60$	G92	512	900 <sup>a</sup>	12	75
MCX (approx.) (Ref. 16)	LL5	0.05	10.1	$60 \times 60 \times 60$	G92	1792	3,800 <sup>a</sup>	12	325
WMC-GPU (Ref. 15)	MWC	0	90	200 <sup>a</sup>	8800GT	26,880	1,747	1.6	1080
GPU-MCML (Ref. 17)	MWC	0.015	708	$100 \times 100$	GTX 480	13,440	384	0.4	870

<sup>a</sup>Estimated.

execute the current instruction can advance to the next instruction; others must wait for the multiprocessor to execute their instruction. In a Monte Carlo simulation, particle paths can diverge. For instance, high-energy photons can undergo a wide range of physical interactions with matter. Furthermore, a comprehensive model of dose deposition in matter requires simulation of the electrons induced by Compton scatter and photoelectric absorption. Because of these effects, naive GPU implementations result in high thread divergence and modest efficiency.<sup>10,20</sup> Simulation of photon migration in turbid media can also lead to thread divergence: within one iteration, some photons may traverse a boundary or be reflected; others may be scattered or absorbed. Unlike GPU cores, CPU cores have dedicated instruction units. Therefore, each parallel thread can issue its own instruction on a clock cycle, independently of the other threads. In a MapReduce job, parallel tasks are executed as independent processes by CPU cores, and are not penalized if they diverge and follow different code branches. It should be noted that the cores in a modern CPU can also issue special streaming SIMD extension (SSE) instructions, which are applied simultaneously to up to four single-precision floating-point registers. This lower level of parallelism cannot be automatically utilized by MapReduce and requires the developer to specifically use SSE instructions when developing the Map and Reduce tasks.

The Monte Carlo code used in this paper was intended as a case study of MapReduce for a biomedical application. The simplicity of the Monte Carlo code helped focus our presentation on the mechanisms of task distribution. The principles described in this paper can be applied to more complex photon migration simulations, such as those that include a three dimensional (3D) map of the optical coefficients<sup>5</sup> or a multilayered geometry.<sup>3</sup> Hadoop has a distributed cache that can make a set of files available to all the nodes in the cluster. This mechanism can be used to broadcast the optical coefficient map to all the nodes prior to starting the simulation. In our implementation, the distributed cache was used to transfer the MC321 binaries (100 kB) to all the nodes. Once the optical coefficients are available on all the nodes, complex Monte Carlo simulations using heterogeneous geometries may be performed by parallel map tasks, with no internode communications. The outputs of these parallel simulations may be combined by simple reduced tasks, as demonstrated in this work. Apart from the initial broadcast of the optical coefficient map, the use of a more accurate

Monte Carlo package would require no additional data transfer between nodes. The present work suggests that these more complex Monte Carlo simulations would be accelerated by a factor approximately equal to the number of nodes in the cluster.

In the MC-HP implementation, a single Reduce task is used to aggregate the outputs from all Map tasks. This approach may not be fast enough to reduce large outputs (such as for instance a 3D photon fluence matrix) from many Map tasks. Network throughput may also be problematic since data are transferred from many nodes to a single node, creating a bottleneck. To alleviate this issue, parallel Reduce tasks can be generated by setting Map tasks to output their data block by block, using the key to encode the block index. The blocks may be composed of slices for a 3D matrix, or rows in a 2D matrix. This data transfer strategy has the advantage that it is decentralized: many data transfer can occur in parallel, increasing the total bandwidth of the cluster. For optimal efficiency, the number of Reduce tasks can be set to the number of such blocks. After the Reduce step, the blocks—which combine the computations of many Map tasks—are written to distributed storage, from which they can be downloaded.

Although it has its roots in text processing, Hadoop is an evolving technology, continuously adding new features to address the specific needs of a wider spectrum of users. As the framework evolves, we expect that it will become more general-purpose, and even better suited for scientific computation. For example, Hadoop currently requires worker nodes to sort intermediary records by key before applying the Reduce function. This sorting step is unnecessary in scientific applications that use keys as array indices. The open-source status of the Hadoop project allows any developer to modify the framework as needed, and possibly contribute back to the project.

## 6 Conclusion

The inexorable shift of computing to parallel architectures forces us to rethink how algorithms are implemented. Porting an application to a distributed environment is problematic because of the complexity of the software development and the cost of a large-scale computer cluster. For photon migration Monte Carlo simulation, MapReduce helps overcome these two challenges by providing a simple way to deploy massively-parallel applications in a cloud computing environment. The port of the MC321

package to MapReduce was rapid, taking only a week; yet, the code execution scaled to 1920 cores with few signs of diminishing returns. The new distributed code includes features such as fault tolerance and automated load balancing.

## Acknowledgments

Funding for this work was provided by the Stanford Dean's fellowship, the AAPM research seed grant, a DoD BCRP postdoctoral award (W81XWH-11-1-0070), and a NIH research grant (1R01 CA 133474). The authors would like to acknowledge the Oregon Medical Laser Center for making the MC321 package available online.

## References

1. B. C. Wilson and G. Adam, "A Monte Carlo model for the absorption and flux distributions of light in tissue," *Med. Phys.* **10**(6), 824–830 (1983).
2. S. Jacques, "Light distributions from point, line and plane sources for photochemical reactions and fluorescence in turbid biological tissues," *Photochem. Photobiol.* **67**(1), 23–32 (1998).
3. L. Wang, S. L. Jacques, and L. Zheng, "MCML—Monte Carlo modeling of light transport in multi-layered tissues," *Comput. Meth. Prog. Bio.* **47**(2), 131–146 (1995).
4. T. J. Dougherty, "Photodynamic therapy," *Photochem. Photobiol.* **58**(6), 895–900 (1993).
5. D. Boas, J. Culver, J. Stott, and A. Dunn, "Three dimensional Monte Carlo code for photon migration through complex heterogeneous media including the adult human head," *Opt. Express* **10**, 159–170 (2002).
6. Q. Fang, "Mesh-based Monte Carlo method using fast ray-tracing in Plücker coordinates," *Biomed. Opt. Express* **1**, 165–175 (2010).
7. N. Tyagi, A. Bose, and I. J. Chetty, "Implementation of the DPM Monte Carlo code on a parallel architecture for treatment planning applications," *Med. Phys.* **31**(9), 2721–2725 (2004).
8. J. Sempau, A. Sanchez-Reyes, F. Salvat, H. O. ben Tahar, S. B. Jiang, and J. M. Fernandez-Varea, "Monte Carlo simulation of electron beams from an accelerator head using PENELOPE," *Phys. Med. Biol.* **46**(4), 1163–1186, (2001).
9. H. Wang, Y. Ma, G. Pratx, and L. Xing, "Toward real-time Monte Carlo simulation using a commercial cloud computing infrastructure," *Phys. Med. Bio.* **56**(17), N175–N181 (2011).
10. A. Badal and J. Sempau, "A package of Linux scripts for the parallelization of Monte Carlo simulations," *Comput. Phys. Commun.* **175**(6), 440–450 (2006).
11. A. Page, S. Coyle, T. Keane, T. Naughton, C. Markham, and T. Ward, "Distributed Monte Carlo simulation of light transportation in tissue," *Proceedings of the 20th International Parallel and Distributed Processing Symposium*, p. 254 (2006).
12. A. Colasanti, G. Guida, A. Kisslinger, R. Liuzzi, M. Quarto, P. Riccio, and Giuseppe, "Multiple processor version of a Monte Carlo code for photon transport in turbid media," *Comput. Phys. Commun.* **132**(1–2), 84–93 (2000).
13. W. C. Y. Lo, K. Redmond, J. Luu, P. Chow, J. Rose, and L. Lilge, "Hardware acceleration of a Monte Carlo simulation for photodynamic therapy treatment planning," *J. Biomed. Opt.* **14**(1), 014019 (2009).
14. G. Pratx and L. Xing, "GPU computing in medical physics: A review," *Med. Phys.* **38**(5), 2685–2697 (2011).
15. E. Alerstam, T. Svensson, and S. Andersson-Engels, "Parallel computing with graphics processing units for high-speed Monte Carlo simulation of photon migration," *J. Biomed. Opt.* **13**(6), 060504 (2008).
16. Q. Fang and D. A. Boas, "Monte Carlo simulation of photon migration in 3D turbid media accelerated by graphics processing units," *Opt. Express* **17**, 20178–20190 (2009).
17. E. Alerstam, W. C. Y. Lo, T. D. Han, J. Rose, S. Andersson-Engels, and L. Lilge, "Next-generation acceleration and code optimization for light transport in turbid media using GPUs," *Biomed. Opt. Express* **1**, 658–675 (2010).
18. N. Ren, J. Liang, X. Qu, J. Li, B. Lu, and J. Tian, "GPU-based Monte Carlo simulation for light propagation in complex heterogeneous tissues," *Opt. Express* **18**(7), 6811–6823 (2010).
19. A. Badal and A. Badano, "Accelerating Monte Carlo simulations of photon transport in a voxelized geometry using a massively parallel graphics processing unit," *Med. Phys.* **36**(11), 4878–4880 (2009).
20. X. Jia, X. Gu, J. Sempau, D. Choi, A. Majumdar, and S. B. Jiang, "Development of a GPU-based Monte Carlo dose calculation code for coupled electron-photon transport," *Phys. Med. Bio.* **55**(11), 3077–3086 (2010).
21. S. Hissoiny, B. Ozell, H. Bouchard, and P. Despres, "GPUMCD: A new GPU-oriented Monte Carlo dose calculation platform," *Med. Phys.* **38**(2), 754–764 (2011).
22. J. Dean and S. Ghemawat, "MapReduce: Simplified data processing on large clusters," *Commun. ACM* **51**(1), 107–113 (2008).
23. P. Mika and G. Tummarello, "Web semantics in the clouds," *IEEE Intell. Syst.* **23**, 82–87 (2008).
24. R. Baeza-Yates, C. Castillo, F. Junqueira, V. Plachouras, and F. Silvestri, "Challenges on distributed web retrieval," in *International Conference on Data Eng.* 6–20 (2007).
25. C. Moretti, K. Steinhaeuser, D. Thain, and N. Chawla, "Scaling up classifiers to cloud computers," in *International Conference on Data Mining*, 472–481 (2008).
26. J. Wolfe, A. Haghighi, and D. Klein, "Fully distributed EM for very large datasets," in *Proceedings of International Conference on Machine Learning*, New York, pp. 1184–1191, ACM (2008).
27. E. Schadt, M. Linderman, J. Sorenson, L. Lee, and G. Nolan, "Computational solutions to large-scale data management and analysis," *Nat. Rev. Genet.* **11**(9), 647–657 (2010).
28. A. McKenna, M. Hanna, E. Banks, A. Sivachenko, K. Cibulskis, A. Kernysky, K. Garimella, D. Altshuler, S. Gabriel, M. Daly, and M. A. DePristo, "The Genome analysis toolkit: A MapReduce framework for analyzing next-generation DNA sequencing data," *Genome Res.* **20**(9), 1297–1303 (2010).
29. M. Schatz, "Cloudburst: highly sensitive read mapping with MapReduce," *Bioinformatics* **25**(11), 1363–1369 (2009).
30. F. Wang, V. Ercegovic, T. Syeda-Mahmood, A. Holder, E. Shekita, D. Beymer, and L. H. Xu, "Large-scale multimodal mining for healthcare with MapReduce," in *Proceedings of the ACM International Health Informatics Symp.* New York, pp. 479–483, ACM (2010).
31. T. White, *Hadoop: The Definitive Guide*, O'Reilly Media (2009).
32. O. O'Malley and A. Murthy, "Winning a 60 second dash with a yellow elephant," <http://sortbenchmark.org> (2009).
33. G. Pratx, C. Carpenter, C. Sun, and L. Xing, "X-ray luminescence computed tomography via selective excitation: A feasibility study," *IEEE Trans. Med. Imag.* **29**, 1992–1999 (2010).
34. Z. Zhao and R. Myllyla, "The effects of optical scattering on pulsed photoacoustic measurement in weakly absorbing liquids," *Meas. Sci. Technol.* **12**(12), 2172–2177 (2001).
35. B. Meng, G. Pratx, and L. Xing, "Ultra-fast and scalable cone-beam CT reconstruction using MapReduce in a cloud computing environment," *Med. Phys.* (in press).

# High-Resolution Radioluminescence Microscopy of $^{18}\text{F}$ -FDG Uptake by Reconstructing the $\beta$ -Ionization Track

Guillem Pratx, Kai Chen, Conroy Sun, Marian Axente, Laura Sasportas, Colin Carpenter, and Lei Xing

*Department of Radiation Oncology, Stanford University School of Medicine, Stanford, California*

Radioluminescence microscopy is a new method for imaging radionuclide uptake by single live cells with a fluorescence microscope. Here, we report a particle-counting scheme that improves spatial resolution by overcoming the  $\beta$ -range limit. **Methods:** Short frames (10  $\mu\text{s}$ –1 s) were acquired using a high-gain camera coupled to a microscope to capture individual ionization tracks. Optical reconstruction of the  $\beta$ -ionization track (ORBIT) was performed to localize individual  $\beta$  decays, which were aggregated into a composite image. The new approach was evaluated by imaging the uptake of  $^{18}\text{F}$ -FDG in nonconfluent breast cancer cells. **Results:** After image reconstruction, ORBIT resulted in better definition of individual cells. This effect was particularly noticeable in small clusters (2–4 cells), which occur naturally even for nonconfluent cell cultures. The annihilation and Bremsstrahlung photon background signal was markedly lower. Single-cell measurements of  $^{18}\text{F}$ -FDG uptake that were computed from ORBIT images more closely matched the uptake of the fluorescent glucose analog (Pearson correlation coefficient, 0.54 vs. 0.44, respectively). **Conclusion:** ORBIT can image the uptake of a radiotracer in living cells with spatial resolution better than the  $\beta$  range. In principle, ORBIT may also allow for greater quantitative accuracy because the decay rate is measured more directly, with no dependency on the  $\beta$ -particle energy.

**Key Words:** radionuclide imaging instrumentation; single-cell analysis; microscopy; autoradiography

**J Nucl Med 2013; 54:1841–1846**

DOI: 10.2967/jnumed.112.113365

**A**utoradiography is a well-established method for high-resolution imaging of radionuclide probes in tissues. Film and emulsion methods have the highest spatial resolution but poor sensitivity, dynamic range, and quantitative accuracy and require tedious sample preparation (1,2). Other autoradiography methods (e.g., storage phosphor (3), solid-state detection (4,5), gaseous detectors (6), and thin phosphor (7)) have higher sensitivity and dynamic range but spatial resolution worse than 50  $\mu\text{m}$ . Only a few methods have demonstrated the ability to visualize the uptake of radionuclide probes with single-cell resolution. One of these methods uses a  $\beta$ -sensitive avalanche photodiode to measure radionuclide uptake in small groups of cells, cultured in 16 microfluidic chambers (8). An experiment showed that the avalanche photodiode could measure

signal from a single cell in the chamber. Another device, the Micro-Imager, achieved 15- $\mu\text{m}$  spatial resolution for  $^{35}\text{S}$ , which was used to detect in situ hybridization in single neurons (9). A third device, the radioluminescence microscope, was developed to visualize radionuclide uptake in live cells during fluorescence microscopy (10). Radioluminescence microscopy can be used to measure fluorescent and radionuclide signals emanating from a collection of living cells, in a relatively short time. Here we propose a new particle-counting scheme for radioluminescence microscopy with higher spatial resolution and, in principle, quantitative accuracy.

The standard radioluminescence microscopy approach uses a scintillator plate, placed in contact with the cells of interest, to convert ionizing radiation from radioactive  $\beta$  decay into visible-range photons detectable with a fluorescence microscope (Fig. 1A). To ensure good contact, the cells are grown such that they adhere to the scintillator plate. The transparency of the plate in the visible range allows for conventional microscopy techniques (e.g., fluorescence and brightfield). Before imaging, the cells are incubated with a radionuclide probe and then washed to remove the excess probe. A radioluminescence image is acquired using a sensitive camera coupled to a high-numerical-aperture microscopy objective (Fig. 1A). A typical image requires an exposure time of several minutes and combines the contributions of thousands of  $\beta$  particles, each emitted with a random energy and direction.

Although radioluminescence microscopy can measure radiotracer uptake with single-cell resolution (10), this single-exposure approach is suboptimal for 2 reasons. First, as each  $\beta$ -particle travels through the scintillator plate, it leaves behind a track of optical photons. Since a  $\beta$ -particle may travel beyond the boundaries of the cell in which it was emitted, it may contribute radioluminescence signal to other surrounding cells, which makes it difficult to distinguish individual cells in the radioluminescence image. Second, the contribution of each individual positron decay event to the total luminescent signal varies greatly because each positron is emitted with a variable amount of kinetic energy and deposits a variable fraction of this energy in the scintillator at a variable depth. The inclusion in the signal of these random quantities results in higher statistical variance.

We report a new image acquisition scheme for radioluminescence microscopy that solves the 2 aforementioned problems. Rather than acquiring a single image with a long exposure time (e.g., 5 min), we take thousands of short frames with high-electron-multiplication gain. With this method, we can visualize the ionization tracks produced by individual  $\beta$  particles as they travel through the scintillator. We trace each track backward to the 2-dimensional location of the corresponding  $\beta$  decay. From the estimated locations of many radioactive decays, we synthesize a composite image that has improved spatial resolution compared with the single-exposure acquisition scheme (Fig. 1B). We have given this particle-counting

Received Sep. 20, 2012; revision accepted Apr. 12, 2013.

For correspondence or reprints contact: Guillem Pratx, 875 Blake Wilbur Dr., MC 5847, Stanford, CA 94305.

E-mail: pratx@stanford.edu

Published online Sep. 3, 2013.

COPYRIGHT © 2013 by the Society of Nuclear Medicine and Molecular Imaging, Inc.

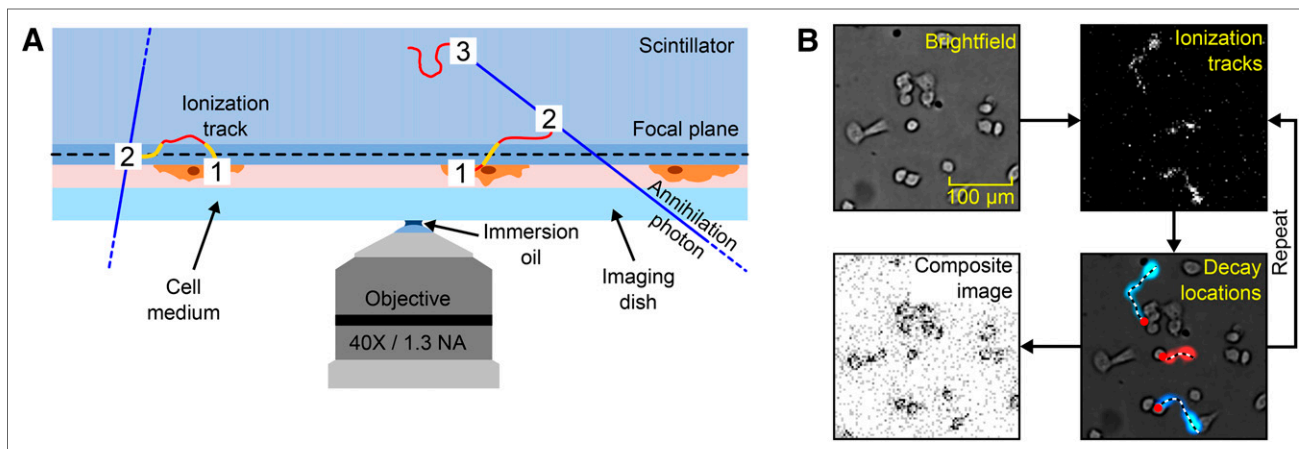


**FIGURE 1.** Radioluminescence microscopy using ORBIT. (A) Emission of positron from radiotracer bound to cell (1) is followed by positron-electron annihilation (2) and emission of 2 back-to-back 511-keV photons (blue lines), which may interact with electron in scintillator via Compton scatter or photoelectric absorption (3). Energetic charged particles (red lines) propagate through scintillator, producing light, which can be recorded by microscope. Because of shallow depth of field, system is sensitive only to events occurring near focal plane. (Drawing is not to scale: objective's field of view is 1.2 mm). (B) To acquire radioluminescence image with ORBIT, bright-field micrograph is first acquired to delineate cell boundaries. Sequence of short image frames is then acquired with high gain to capture ionization tracks produced by energetic charged particles. Those frames are processed to extract decay locations, which are then aggregated into composite image. (Each decay location is represented as a dot). NA = numerical aperture.

scheme the name *optical reconstruction of the  $\beta$ -ionization track* (ORBIT).

Although in principle similar to existing particle-counting autoradiography systems (5,9), ORBIT can image and reconstruct individual ionization tracks. In this regard, it is comparable to single-molecule fluorescence microscopy methods such as subdiffraction-limit imaging by stochastic optical reconstruction microscopy (11). This method uses bright light pulses to stochastically photoactivate a small number of fluorescent proteins, which are then fluorescently imaged. Because of their sparse distribution, individual activated proteins can be localized with precision greater than the diffraction limit. By repeating this process, different subsets of proteins can be activated and imaged. Similarly, ORBIT exploits the fact that radioactive decay is stochastic, and thus only a small number of randomly distributed ionization tracks are produced within a short time frame. The number of optical photons produced in a scintillator during a single radioactive decay event is large enough to be detected by a sensitive microscope. For instance, the kinetic energy of a positron emitted during the decay of  $^{18}\text{F}$  can be as high as 634 keV, which for a scintillator such as  $\text{CdWO}_4$  (15 photons/keV) would result in up to 9,500 photons emitted.

## MATERIALS AND METHODS

### Imaging System

The microscope setup used in this study has been described elsewhere (10). A 40X/1.3-numerical aperture oil-immersion objective (UPLFLN40XO; Olympus) was used for all experiments. We estimate that the microscope collects approximately 13% of the photons emitted near the focal plane, based on the objective light collection efficiency (25% for a 1.3 numerical aperture) and transmission (80%), the throughput of the tube lens (80%), and the quantum efficiency of the charge-coupled device (CCD) (80%). The light collection efficiency calculation does not account for the higher index of refraction of the scintillator ( $n = 2.3$ ). Experimentally, we found that the microscope could record 31% of the photons emitted by a bioluminescent light source (Supplemental Fig. 1; supplemental materials are available online at <http://jnm.snmjournals.org>). The discrepancy between these

2 values may be due to camera calibration factors, electron-multiplication gain nonlinearity, and the nonideal behavior of the microscope objective.

### Depth-Varying Point-Spread Function

We characterized the depth-varying point-spread function and modulation transfer function of the microscope objective using an analytic model (12). The model accounts for the immersion oil and the index of refraction of the scintillator. Using this model, we computed via convolution the response of the microscope to a small pointlike object placed at different depths. The object was a 3-dimensional gaussian function with a full width at half maximum of 6.5  $\mu\text{m}$ —that is, twice the camera pixel size (with  $2 \times 2$  binning).

### ORBIT Imaging

The general methodology for acquiring an ORBIT image is as follows. We first acquire a sequence of frames with a short exposure time, an electron-multiplication gain of 1,200, and  $2 \times 2$  binning. The exposure time must be set to maximize the system sensitivity. On the one hand, the exposure should be short enough to avoid spatiotemporal overlap between different ionization tracks. On the other hand, it should be longer than the camera readout time to allow for continuous imaging. For highly radioactive samples, these 2 conditions cannot be simultaneously satisfied; therefore, the exposure should be set to the highest value that causes no overlap between tracks. Typically, this value corresponds to an average of 10 ionization events per frame (Supplemental Fig. 2), but it may vary with the spatial distribution of the activity. Loss of sensitivity due to slow camera readout is spatially uniform. Given the range of camera exposures available (10  $\mu\text{s}$ –10 s), the microscope can image a wide range of radionuclide activities, from 0.2 Bq/ $\text{mm}^2$  to 20 kBq/ $\text{mm}^2$ . For a fixed exposure time, the event rate is also linear with activity concentration (Supplemental Fig. 3).

The automated extraction of  $\beta$  trajectories from the sequence of short frames involves a certain number of image processing steps. Briefly, each frame is first filtered with a gaussian kernel to reduce spatially uncorrelated shot noise. An H-maxima transform is then applied to suppress small local image maxima. The processed image is later segmented using a constant threshold set above the noise floor.

Morphologic operations are also applied to regularize the delineation of the segmented tracks.

For image processing purposes, we distinguish 3 types of ionization tracks. Long tracks ( $\leq 500 \mu\text{m}$ ) are produced by positrons with high initial kinetic energy and are traced backward to the decay origin using a custom algorithm (Fig. 2A). Because the direction of the particle along the track is ambiguous, the origin is defined as the end of the track closest to a cell (segmented from a bright-field micrograph). Shorter tracks are characteristic of positrons that either travel a short distance because of lower kinetic energy or travel orthogonally to the imaging plane (Fig. 2B). These tracks are directly assigned to the nearest cell. Last, annihilation photons are more likely to interact deep in the scintillator plate, away from the focal plane (Fig. 1A). These interactions sometimes appear as a diffuse, out-of-focus luminescence signal and are rejected during image processing (Fig. 2C). A more detailed description of the track reconstruction algorithm is presented as supplemental information.

The final ORBIT image is reconstructed by aggregating the decay locations estimated from the sequence of frames. The resulting image is then filtered with a gaussian kernel to account for the localization uncertainty.

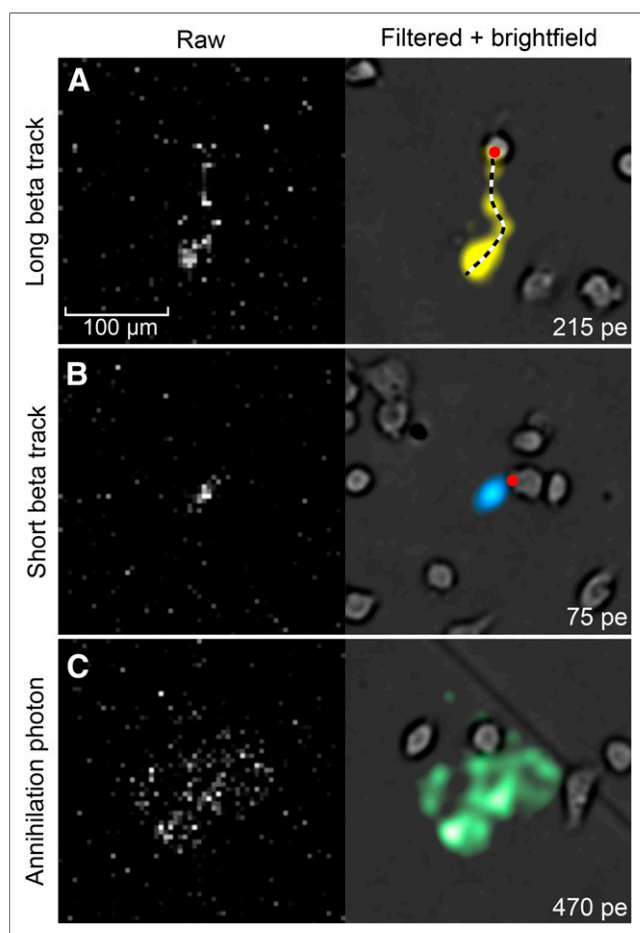


**FIGURE 2.** Examples of ionization tracks. (A) Long ionization track, originating from cell. Dashed line is estimated positron trajectory. (B) Shorter ionization track, likely produced by low-energy positron or positron traveling orthogonally to imaging plane. Red dot is estimated decay location. (C) Annihilation photon interacting deep in scintillator and producing diffuse, unfocused signal. Such signals are not used in final image. Number of photoelectrons (pe) recorded by CCD sensor for each event is indicated.

## Annihilation and Bremsstrahlung Photon Contamination

To evaluate the proportion of events that is produced by secondary annihilation and Bremsstrahlung photons, we imaged the ionization tracks produced by a thin layer of  $^{18}\text{F}$ -FDG ( $19 \text{ kBq/mm}^2$ ) while varying the focal plane depth. For each depth, we counted how many ionization tracks were in focus in 200 sequential images (27-ms exposure). Because the objective has a shallow depth of field, only ionization tracks near the focal plane are in focus. Because of the limited range of positrons, tracks observed deep in the scintillator are attributed to high-energy photons.

## Cell Imaging

As a demonstration, we imaged the uptake of  $^{18}\text{F}$ -FDG in human breast adenocarcinoma cells and compared it with an optical fluorescent glucose analog, 2-[*N*-(7-nitrobenz-2-oxa-1,3-dioxol-4-yl)amino]-2-deoxyglucose (2-NBDG). We seeded  $10^4$  MDA-MB-231 cells on a  $10 \times 10 \times 0.5 \text{ mm}$   $\text{CdWO}_4$  scintillator plate. The plate was immersed in RPMI 1640 supplemented with 10% fetal bovine serum and 1% penicillin/streptomycin and stored at  $37^\circ\text{C}$  in a humidified atmosphere with 5%  $\text{CO}_2$ . The next day, the cells were approximately 10% confluent and did not present signs of altered function (Supplemental Fig. 4). After keeping the cells fasting for 30 min in glucose-free RPMI, we incubated them for 1 h at  $37^\circ\text{C}$  with  $^{18}\text{F}$ -FDG (11 MBq) and 2-NBDG (100  $\mu\text{M}$ ) and washed them to remove the excess probe.

Imaging was performed by 2 methods. First, a single radioluminescence image was acquired with an exposure time of 5 min and an electron-multiplication gain of 201. Then, a sequence of 6,000 frames was acquired with an exposure time of 50 ms—effectively spanning 5 min—and an electron-multiplication gain of 1,200 and reconstructed into a single image using ORBIT. Image reconstruction took about 8 h using MATLAB (The MathWorks) on a recent computer, with most of the computation spent reconstructing long positron tracks.

## RESULTS

The point-spread function and modulation transfer function were found to depend strongly on the depth of the source (Supplemental Fig. 5). The Nyquist frequency for the camera (0.15 cycles/ $\mu\text{m}$  for  $2 \times 2$  binning) was attenuated by 50% at a 2- $\mu\text{m}$  depth and by 90% at 4  $\mu\text{m}$ . For a small point-source object, the response of the microscope decreased gradually with depth (Fig. 3), an effect known as optical sectioning. It follows from these results that the sensitive region of the scintillator spans approximately 5  $\mu\text{m}$  on either side of the focal plane. Therefore, when an energetic positron intersects the focal plane, the microscope can capture only the portion of its track that is in this sensitive region. The simulation of simple positron trajectories showed that the transition between the 2 regions is gradual (Supplemental Fig. 6). Because of optical sectioning, the microscope captures only a fraction of the total energy deposited by energetic positrons, which can travel up to 500  $\mu\text{m}$  in  $\text{CdWO}_4$ .

By varying the depth of the focal plane, we estimated that positrons constitute 92% of the events recorded at the scintillator edge (Fig. 4). The event counting rate was 1,010 cps for positrons and 90 cps for annihilation and Bremsstrahlung photons. Positrons rarely traveled more than 20  $\mu\text{m}$  from the scintillator edge, highlighting the need for precise focusing to maximize positron sensitivity.

An ORBIT radioluminescence image of cellular  $^{18}\text{F}$ -FDG uptake was synthesized from 33,253 events (110.8 cps). As a control, we also imaged a sample not incubated with  $^{18}\text{F}$ -FDG and measured a background rate of 1.2 cps, likely caused by cosmic radiation and background noise in the camera. On the basis of the

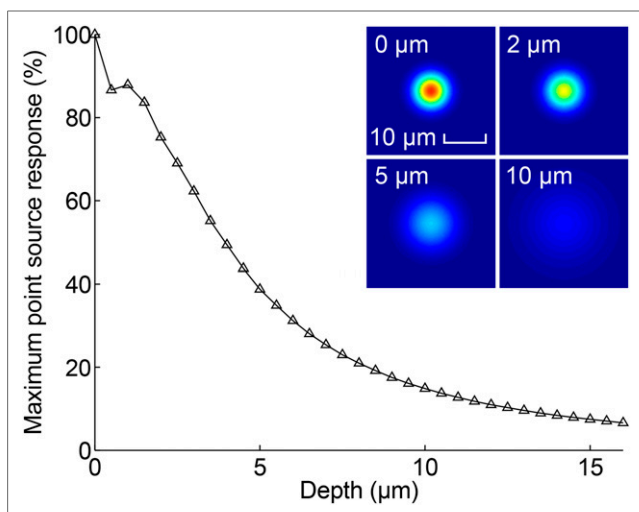


**FIGURE 3.** Maximum point-source response as function of depth. Maximum response of microscope to small object (gaussian distribution with a full-width half-maximum of  $6.5\ \mu\text{m}$ ) placed at various depths was computed using analytic model. Inset shows 2-dimensional point-spread function (depth, 0, 1, 1.5, and  $2\ \mu\text{m}$ ).

camera gain and calibration factor, we estimated that single ionization events created between 20 and 1,000 photoelectrons in the CCD sensor, with an average of 390 (Supplemental Fig. 7A). On the basis of the estimated optical sensitivity of the system and the light yield of the scintillator, these correspond to minimum, average, and maximum energy depositions of 10, 200, and 510 keV, respectively. These observed energy depositions reflect the diversity of positron energies and trajectories and represent only ionization occurring within  $5\ \mu\text{m}$  of the focal plane. This may be why the average measured energy was smaller than the average positron energy for  $^{18}\text{F}$  (250 keV).

For both imaging modes, the noise is dominated by shot noise and, for the high-gain acquisition, excess noise factor, with a negligible contribution from dark noise (0.001 electron/pixel/s) and read noise (0.01 electron/pixel at 11 MHz, relative to electron-multiplication gain). On average, a positron produced 0.6 photoelectrons per CCD pixel (before electron-multiplication and analog gain, but after  $2 \times 2$  pixel binning; Supplemental Fig. 7B). In comparison, a pixel receives approximately 150 photoelectrons for a 5-min exposure. As a result, single ORBIT frames have a low signal-to-noise ratio compared with longer exposures (Supplemental Table 1). Other sources of background signal include Cerenkov luminescence—approximately 1.4 photons per decay for  $^{18}\text{F}$  (13)—and scintillator afterglow (e.g., lutetium orthosilicate).

Although isolated cells are clearly distinguishable on the 5-min exposure image (Fig. 5A, red arrows), ORBIT provides better resolution of single cells in small clusters of 2–4 cells (Fig. 3A, yellow arrows). A line profile through the images confirms that peaks and valleys are better defined on the ORBIT image and coincide to a greater degree with the fluorescence image (Fig. 5B; Pearson correlation coefficient, 0.85 vs. 0.67). In contrast, the 5-min-exposure radioluminescence image presents a higher level of background signal between peaks, likely caused by annihilation and Bremsstrahlung photons, and a widening of the peaks, due to positron range blurring. In addition, ORBIT directly counts how many decays occur within each cell, with no dependence on the variable positron energy. Thus, a region-of-interest analysis found

that, on a cell-by-cell basis, 2-NBDG fluorescence was more highly correlated with  $^{18}\text{F}$ -FDG uptake measured with ORBIT than with a 5-min exposure (Fig. 5C). A perfect correlation between  $^{18}\text{F}$ -FDG and 2-NBDG is not achievable as the 2 probes are not strictly identical: 2-NBDG is degraded after cell internalization, becoming inactive, whereas  $^{18}\text{F}$ -FDG accumulates in the cell as FDG-6-phosphate. Physical differences between radionuclide decay and fluorescence emission can also account for discrepancies between the 2 signals.

## DISCUSSION

We found that ORBIT could visualize individual decay events and resulting ionization tracks. By processing those ionization tracks, we produced images of the distribution of  $^{18}\text{F}$ -FDG in living cells with spatial resolution greater than the positron range. Whereas a single-exposure radioluminescence image has arbitrary camera units, an ORBIT image has units of counting rate. In principle, a particle-counting approach such as ORBIT should be more quantitative than an integrating approach. That may be why ORBIT images provided measurements of  $^{18}\text{F}$ -FDG uptake in single cells that presented a stronger correlation to the uptake of a fluorescent glucose analog. A precise comparison between the 2 approaches will be the aim of future work.

We also found that because of the shallow depth of field of the objective, imaging of ionizing events is restricted to a  $10\text{-}\mu\text{m}$ -thick slab centered on the focal plane. This feature of the microscope allowed us to better discriminate between positrons, which travel short distances, and secondary photons, which interact more deeply in the scintillator.

ORBIT works best for nonconfluent cell cultures because each positron track can reliably be assigned to a cell delineated from a bright-field microscopy image. ORBIT is generally able to distinguish individual cells in small clusters (2–4 cells) that naturally occur during cell growth (Fig. 3A, yellow arrows). However, for more confluent cell distributions such as tissue sections, the bright-field image is less useful for estimating the positron direction along the track because more than one cell may be equally close to the

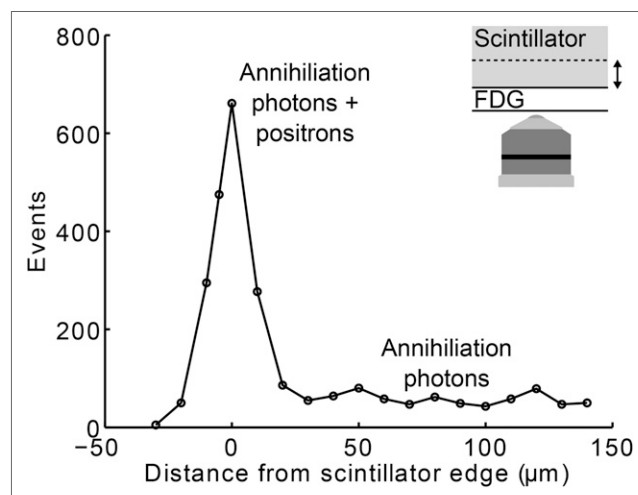


**FIGURE 4.** Annihilation and Bremsstrahlung photon contamination. A thin layer of  $^{18}\text{F}$ -FDG ( $19\ \text{kBq}/\text{mm}^2$ ) placed between scintillator and imaging dish was imaged by acquiring 200 frames (3-ms exposure). Events in focus—that is, that displayed high-frequency features—were counted at various focal depths.

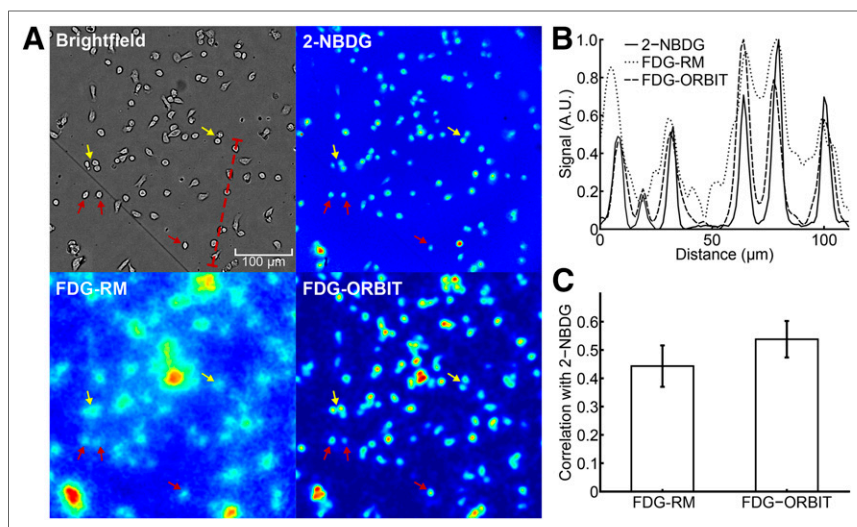


**FIGURE 5.** Radioluminescence microscopy of  $^{18}\text{F}$ -FDG uptake. Human breast cancer cells (MDA-MB-231) were deprived of glucose for 1 h, incubated for 1 h with  $^{18}\text{F}$ -FDG (11 MBq) and 2-NBDG (100  $\mu\text{M}$ ), and then washed. (A) Bright-field (scale bar, 200  $\mu\text{m}$ ), fluorescence (2-NBDG), single-exposure radioluminescence microscopy (FDG-RM), and ORBIT (FDG-ORBIT). Objective is  $40\times/1.3$  numerical aperture. (B) Radioluminescence and fluorescence intensity shown along line profile (red dashed line in A). (C) Correlation between cellular uptake of 2-NBDG and  $^{18}\text{F}$ -FDG, where  $^{18}\text{F}$ -FDG uptake was measured with conventional radioluminescence microscopy (FDG-RM) or ORBIT (FDG-ORBIT). Cellular uptake was computed by drawing circular region of interest around each cell on bright-field image.

ionization track. This is unfortunate because dense cell distributions are more representative of physiologic conditions. ORBIT can be adapted to imaging dense tissue in several ways. As the positron slows down, it becomes more ionizing and its ionization track becomes brighter. Furthermore, as the positron moves away from the focal plane, the ionization track becomes defocused. These properties may help determine the direction of the positron along its track. Alternatively, long ionization tracks may also be discarded in favor of shorter tracks that are easier to localize. Tissue dissociation techniques may also allow dense tissues to be physically separated for imaging (14).

The ORBIT method can readily be extended to dynamic studies. Short frames can be acquired for the desired duration of the study, retrospectively gated into time intervals, and independently reconstructed. However, the use of the bright-field image to delineate cells is not optimal in the presence of background activity. Positrons emitted from a free radionuclide probe will produce ionization tracks that should not be associated with a cell. Thus, to avoid bias,  $\beta$  particles should be localized without using the bright-field image when significant activity is present in the background.

Highly sensitive CCD cameras with high internal gain, comparable to the one used in this work, have in recent years found application in high-resolution SPECT imaging (15–18). These SPECT systems image the ionization track produced by low-energy  $\gamma$  rays interacting in a thin scintillator screen. Similar to our work, they apply image-processing algorithms to extract the position and energy of each individual  $\gamma$ -ray interaction. Such an imaging scheme enables spatial resolution on the order of 50–70  $\mu\text{m}$ , much higher than conventional SPECT systems. In a similar fashion, a digital autoradiography system was recently developed using a high-efficiency CCD sensor (19). By placing the tissue of

interest in direct contact with the CCD, this system can directly visualize the trajectories of positrons entering the silicon detector. The system achieved a spatial resolution of 86  $\mu\text{m}$  when imaging  $^{18}\text{F}$  in a 100- $\mu\text{m}$ -thick tissue section. However, it is not compatible with live cell imaging because the CCD sensor must be cooled to very low temperatures. Furthermore, unlike radioluminescence microscopy, it is unable to image the tissue optically.

## CONCLUSION

Because of limited spatial resolution, autoradiography and other methods can measure the uptake of a radiotracer only in a relatively large cell population. In contrast, radioluminescence microscopy is able to measure radiotracer uptake with single-cell resolution, in the familiar environment of a fluorescence microscope, using fluorescent probes to highlight biochemical features of interest. Dynamic studies can also shed light on radiotracer kinetics in vitro and at the single-cell level. The ORBIT scheme presented here makes those single-cell measurements more accurate with no increase in imaging time or hardware complexity. Future work will focus on applying this approach for imaging denser cell distributions such as tissue sections.

## DISCLOSURE

The costs of publication of this article were defrayed in part by the payment of page charges. Therefore, and solely to indicate this fact, this article is hereby marked “advertisement” in accordance with 18 USC section 1734. This work was supported by the National Institutes of Health under grant NIH ICMIC P50CA114747 and by the Department of Defense under grant W81XWH-11-1-0070. The Olympus Corporation provided the LV200. No other potential conflict of interest relevant to this article was reported.

## ACKNOWLEDGMENTS

The authors gratefully acknowledge the help of the Stanford nuclear medicine technologists, Stanford postdoctoral fellows Irfan Ali-Khan and Steven Sensarn for assistance with the instrumentation, and the Stanford Small-Animal Imaging and Radiochemistry Facility.

## REFERENCES

1. Kubota R, Yamada S, Kubota K, Ishiwata K, Tamahashi N, Ido T. Intratumoral distribution of fluorine-18-fluorodeoxyglucose in vivo: high accumulation in macrophages and granulation tissues studied by microautoradiography. *J Nucl Med.* 1992;33:1972–1980.
2. Nielsen JL, Halkjær Nielsen P. Advances in microscopy: microautoradiography of single cells. *Methods Enzymol.* 2005;397:237–256.
3. Johnston RF, Pickett SC, Barker DL. Autoradiography using storage phosphor technology. *Electrophoresis.* 1990;11:355–360.
4. Ott RJ, Macdonald J, Wells K. The performance of a CCD digital autoradiography imaging system. *Phys Med Biol.* 2000;45:2011–2027.

5. Mettievier G, Montesi MC, Russo P. First images of a digital autoradiography system based on a Medipix2 hybrid silicon pixel detector. *Phys Med Biol*. 2003;48:N173–181.
6. Charpak G, Dominik W, Zaganidis N. Optical imaging of the spatial distribution of beta-particles emerging from surfaces. *Proc Natl Acad Sci USA*. 1989;86:1741–1745.
7. Chen L, Gobar LS, Knowles NG, Liu Z, Gmitro AF, Barrett HH. Direct imaging of radionuclide-produced electrons and positrons with an ultrathin phosphor. *J Nucl Med*. 2008;49:1141–1145.
8. Vu NT, Zeta T, Comin-Anduix B, et al. A  $\beta$ -camera integrated with a microfluidic chip for radioassays based on real-time imaging of glycolysis in small cell populations. *J Nucl Med*. 2011;52:815–821.
9. Lanière P, Charon Y, Dumas S, et al. HRRI: a high resolution radioimager for fast, direct quantification in in situ hybridization experiments. *Biotechniques*. 1994;17:338–345.
10. Pratz G, Chen K, Sun C, et al. Radioluminescence microscopy: measuring the heterogeneous uptake of radiotracers in single living cells. *PLoS ONE*. 2012;7:e46285.
11. Rust MJ, Bates M, Zhuang X. Sub-diffraction-limit imaging by stochastic optical reconstruction microscopy (STORM). *Nat Methods*. 2006;3:793–795.
12. Gibson SF, Lanni F. Experimental test of an analytical model of aberration in an oil-immersion objective lens used in three-dimensional light microscopy. *J Opt Soc Am A*. 1992;9:154–166.
13. Mitchell GS, Gill RK, Boucher DL. In vivo Cerenkov luminescence imaging: a new tool for molecular imaging. *Phil Trans R Soc A*. 2011;369:4605–4619.
14. Hedley DW. Flow cytometry using paraffin-embedded tissue: five years on. *Cytometry*. 1989;10:229–241.
15. Meng LJ, Fu G, Roy EJ, Suppe B, Chen CT. An ultrahigh resolution SPECT system for I-125 mouse brain imaging studies. *Nucl Instrum Meth A*. 2009;600:498–505.
16. Soesbe TC, Lewis MA, Slavine NV, Richer E, Bonte FJ, Antich PP. High-resolution photon counting using a lens-coupled EMCCD gamma camera. *IEEE Trans Nucl Sci*. 2010;57:958–963.
17. Nagarkar VV, Shestakova I, Gaysinskiy V, Singh B, Miller BW, Bradford Barber H. Fast x-ray/ $\gamma$ -ray imaging using electron multiplying CCD-based detector. *Nucl Instrum Meth A*. 2006;563:45–48.
18. Miller BW, Barrett HH, Furenlid LR, Bradford Barber H, Hunter RJ. Recent advances in BazookaSPECT: real-time data processing and the development of a gamma-ray microscope. *Nucl Instrum Meth A*. 2008;591:272–275.
19. Peng Q, Holland SE, Choong WS, Budinger TF, Moses WW. Real-time quantitative ex vivo direct autoradiography with 10 $\mu$ m pixel resolution. *Conf Proc IEEE Eng Med Biol Soc*. 2011:6273–6276.

### Erratum

In the article “Assessment of Treatment Response in Patients with Glioblastoma Using *O*-(2-<sup>18</sup>F-Fluoroethyl)-L-Tyrosine PET in Comparison to MRI,” by Galldiks et al. (*J Nucl Med*. 2012;53:1048–1057), the abstract mistakenly stated, “Receiver-operating-characteristic analysis showed that a decrease of the TBR(max) between FET-1 and FET-2 of more than 20% predicted poor survival. . . .” However, such a decrease in fact predicted favorable survival, not poor survival. The authors regret the error.

---

# Intraoperative Imaging of Tumors Using Cerenkov Luminescence Endoscopy: A Feasibility Experimental Study

Hongguang Liu<sup>\*1</sup>, Colin M. Carpenter<sup>\*2</sup>, Han Jiang<sup>1</sup>, Guillem Pratx<sup>2</sup>, Conroy Sun<sup>2</sup>, Michael P. Buchin<sup>3</sup>, Sanjiv S. Gambhir<sup>1,4</sup>, Lei Xing<sup>2</sup>, and Zhen Cheng<sup>1</sup>

<sup>1</sup>Molecular Imaging Program at Stanford (MIPS), Department of Radiology and Bio-X Program, Canary Center at Stanford for Cancer Early Detection, Stanford University, Stanford, California; <sup>2</sup>Department of Radiation Oncology, Stanford University, Stanford, California; <sup>3</sup>Stanford Photonics, Inc., Palo Alto, California; and <sup>4</sup>Department of Bioengineering and Materials Science and Engineering, Stanford University, Stanford, California

Cerenkov luminescence imaging (CLI) is an emerging new molecular imaging modality that is relatively inexpensive, easy to use, and has high throughput. CLI can image clinically available PET and SPECT probes using optical instrumentation. Cerenkov luminescence endoscopy (CLE) is one of the most intriguing applications that promise potential clinical translation. We developed a prototype customized fiberoptic Cerenkov imaging system to investigate the potential in guiding minimally invasive surgical resection. **Methods:** All experiments were performed in a dark chamber. Cerenkov luminescence from <sup>18</sup>F-FDG samples containing decaying radioactivity was transmitted through an optical fiber bundle and imaged by an intensified charge-coupled device camera. Phantoms filled with <sup>18</sup>F-FDG were used to assess the imaging spatial resolution. Finally, mice bearing subcutaneous C6 glioma cells were injected intravenously with <sup>18</sup>F-FDG to determine the feasibility of in vivo imaging. The tumor tissues were exposed, and CLI was performed on the mouse before and after surgical removal of the tumor using the fiber-based imaging system and compared with a commercial optical imaging system. **Results:** The sensitivity of this particular setup was approximately 45 kBq (1.21  $\mu$ Ci)/300  $\mu$ L. The 3 smallest sets of cylindric holes in a commercial SPECT phantom were identifiable via this system, demonstrating that the system has a resolution better than 1.2 mm. Finally, the in vivo tumor imaging study demonstrated the feasibility of using CLI to guide the resection of tumor tissues. **Conclusion:** This proof-of-concept study explored the feasibility of using fiber-based CLE for the detection of tumor tissue in vivo for guided surgery. With further improvements of the imaging sensitivity and spatial resolution of the current system, CLE may have a significant application in the clinical setting in the near future.

**Key Words:** fiber-based imaging; Cerenkov luminescence endoscopy; Cerenkov luminescence imaging; radionuclides; optical imaging; PET

**J Nucl Med 2012; 53:1579–1584**

DOI: 10.2967/jnumed.111.098541

Cerenkov luminescence imaging (CLI) has recently attracted increasing interest in the field of molecular imaging (1,2). CLI is a new optical imaging modality in which images are obtained by monitoring the Cerenkov photons emitted from highly energetic moving charged particles ( $\beta^+$  or  $\beta^-$ ). Conventional nuclear imaging methods, such as PET and SPECT, are the most widely used clinical molecular imaging techniques. However, these modalities usually suffer from high cost, limited availability, relatively low spatial resolution, and low throughput (3). As a technique that bridges optical imaging and radionuclide imaging, CLI has shown many advantages such as high sensitivity, high resolution, low cost, wide availability, relatively high throughput, and commercially available radionuclide probes already approved by the Food and Drug Administration.

Since its discovery in 2009, CLI has quickly become a practical molecular imaging technique, and many new applications of CLI in preclinical research continue to emerge (1,2). Several research groups have demonstrated that CLI can be a powerful tool for tumor imaging using radionuclide probes such as <sup>18</sup>F-FDG. Important validation studies have also been performed, and it was reported that there is a good linear correlation between the tumor uptake quantified by PET and tumor CLI signals in subcutaneous xenograft models (4–7). CLI has also been found to be useful for imaging  $\alpha$  and pure  $\beta^-$  emitters such as <sup>90</sup>Y and <sup>225</sup>Ac, which are used for cancer treatment (4). Moreover, CLI can be applied in the monitoring of reporter gene expression. The herpes simplex virus type 1 thymidine kinase and the sodium iodide symporter reporter genes were recently successfully imaged by CLI in conjunction with

Received Nov. 1, 2011; revision accepted May 2, 2012.

For correspondence or reprints contact either of the following: Zhen Cheng, Molecular Imaging Program at Stanford, Department of Radiology, Bio-X Program, Canary Center at Stanford for Cancer Early Detection, 1201 Welch Rd., Lucas Expansion, P095, Stanford University, Stanford, CA 94305. E-mail: zcheng@stanford.edu

Lei Xing, Department of Radiation Oncology, Stanford University School of Medicine, 875 Blake Wilbur Dr., Stanford, CA 94305-5847. E-mail: lei@stanford.edu

\*Contributed equally to this work.

Published online Aug. 17, 2012.

COPYRIGHT © 2012 by the Society of Nuclear Medicine and Molecular Imaging, Inc.

appropriate radioactive reporter probes (4,8,9). Cerenkov photons have also been used to illuminate fluorescent dyes and nanoparticles for *in vivo* imaging (10–13). A recent study further showed that CLI could be used for monitoring tumor surgery in xenograft mouse models, highlighting the translational potential of the modality (14). CLI has also been used to measure the radiochemical purity of a radiolabeled compound and to image plant physiology (15). In addition to these applications, the recent advancement in CLI tomography makes this novel imaging modality even more powerful and promising for biomedical research including diagnostic imaging and therapeutic monitoring (16–19).

Because it can image clinically available radiotracers, CLI has the potential to be rapidly translated into clinical applications (4,18). However, all the studies described above have involved the use of conventional small-animal optical imaging systems, which are not compatible with routine clinical practice. In this study, we have built the first, to our knowledge, prototype system that is amenable to Cerenkov luminescence endoscopy (CLE) in the clinic. This system comprises an optical fiber bundle and an intensified charge-coupled device (CCD) camera. The small-diameter flexible endoscope is designed for minimally invasive monitoring of living tissues and organs, using a sensitive camera to produce images of the radionuclide probe. It is also expected that hollow organs (e.g., bladder and lung) or insufflated cavities (e.g., esophagus and colon) inside the body can provide natural and anatomic dark chambers for CLE. By overlaying conventional bright-field images commonly obtained from an endoscope with the Cerenkov luminescence images generated by radionuclide probes, CLE could be used to identify diseased tissues for diagnostic purposes and real-time monitoring of endoscopic surgery.

Therefore, we investigated the feasibility of CLE for guiding cancer surgical resection by performing sensitivity, spatial-resolution, and proof-of-concept experiments. The characteristic sensitivity of this system was evaluated using the natural decay of  $^{18}\text{F}$ -FDG. Imaging resolution was determined using a phantom with cylindric holes. Finally, imaging studies were performed to demonstrate surgical guidance in a small-animal tumor model. A well-known commercial optical imaging system was used to provide a comparison. The data presented herein outline the instrumentation and methodology; further steps that are needed to translate this modality into the clinic are also discussed.

## MATERIALS AND METHODS

$^{18}\text{F}$ -FDG was produced by the Radiochemistry Facility at Stanford University. The rat glioma cell line C6 was obtained from American Type Culture Collection. Female athymic nude mice (*nu/nu*) ( $n = 5$ ) obtained from Charles River Laboratories, Inc., were 4–6 wk old. A CRC-15R PET dose calibrator (Capintec Inc.) was used for all radioactivity measurements.

## Tumor Model

All animal studies were performed in compliance with federal and local institutional guidelines for the conduct of animal experimentation. C6 cells were cultured in Dulbecco modified Eagle medium supplemented with 10% fetal bovine serum and 1% penicillin/streptomycin (Invitrogen Life Technologies). The cell line was maintained in a humidified atmosphere of 5%  $\text{CO}_2$  at 37°C, with the medium changed every other day. A 75% confluent monolayer was detached with trypsin and dissociated into a single-cell suspension for further cell culture. Approximately  $1 \times 10^6$  C6 cells suspended in phosphate-buffered saline (0.1 M, pH 7.2; Invitrogen) were implanted subcutaneously in the left legs of nude mice. Tumors were allowed to grow to 150–200 mm<sup>3</sup> (2–3 wk), and the tumor-bearing mice were imaged *in vivo*.

## CLI

Validation CLI was performed with an IVIS Spectrum system (Caliper Life Sciences). For all *in vivo* studies, radionuclides were diluted in phosphate-buffered saline. Animals were placed in a light-tight chamber under isoflurane anesthesia. Each acquisition took 3 min for all studies without filters. Images were acquired and analyzed using Living Image 3.0 software (Caliper Life Sciences). The mice were kept fasting overnight before  $^{18}\text{F}$ -FDG imaging and anesthetized by inhalation of 2% isoflurane during the experiment.

## Fiber-Based CLE System

The fiber-based CLE system used an imaging optical fiber coupled to a highly sensitive intensified CCD camera. The application of this system for surgical oncology guidance is detailed in Figure 1. Specifically, a microimaging lens (Cinegon, F/1.4, 12-mm focal length; Schneider) was coupled at the distal end of an optical imaging fiber bundle that was 108 mm long, with a  $5 \times 6.7$  mm active area. The pixels of the fiber bundle are made of discrete 10- $\mu\text{m}$  fibers (IG154; Schott). At the proximal end, a Pentax (F/1.4) lens provided relay optics to the camera (Supplemental Fig. 1A; supplemental materials are available online only at <http://jnm.snmjournals.org>). The camera, an image-intensified

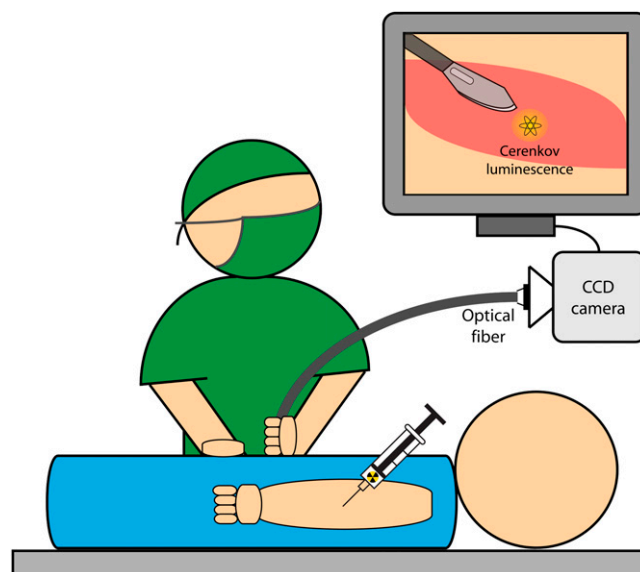


**FIGURE 1.** Suggested application of fiber-based system for endoscopic and laparoscopic CLI.

CCD (Turbo 640-Z; Stanford Photonics Inc.), had  $640 \times 480$  pixels and single-photon imaging capability (Supplemental Fig. 1B). To minimize background light and to emulate a light-tight anatomic cavity, all images were taken in a dark box. In addition, images were postprocessed with a software thresholding technique that removed pixel values below a manufacturer-recommended value; this optimal value was chosen to remove low-intensity pixels that corresponded to thermal and read noise on the CCD. These steps reduced the noise to approximately 20 counts per second.

### Imaging Using Fiber-Based System

Images were acquired at a high frame-rate of 120 Hz to allow for maximal reduction in noise. The noise-reduction step described above was performed for each frame. These frames were then accumulated for 5 min to form the raw data. The raw data were image-processed offline using an algorithm to remove cosmic and stray  $\gamma$ -events. This algorithm removed noisy pixels by thresholding the gradient around each pixel in its local area. An additional denoising step removed spurious bright pixels that appeared in sequential exposures.

The fiber-based CLE system was characterized for sensitivity by imaging 2 adjacent wells of a black 96-well plate (300  $\mu$ L per well). A glycerol and water mixture combined with 3.7 MBq (100  $\mu$ Ci) of  $^{18}\text{F}$ -FDG was in 1 well, and a glycerol and water mixture only was in a nearby well. Images were sequentially acquired over approximately 10 half-lives (19 h, 43 min), and each data point was formed from 5 min of photon accumulation.

The spatial resolution of the system was characterized using a standard PET/SPECT phantom (Micro Hot-Spot Phantom; Data Spectrum Corp.) filled with 15.2 MBq (410  $\mu$ Ci) of  $^{18}\text{F}$ -FDG; this phantom is also commonly used to evaluate the spatial resolution of PET systems. Both the 2.4- and the 1.6-mm cylindrical holes were used to form line profiles, taken from the fiber-based images. An ambient-light image and a functional Cerenkov luminescence image were acquired. The exposure time for all ambient images was less than 1 s, and the functional image acquisition time was 5 min. The subject was 5 cm from the optical system.

### Fiber-Based CLE System for Surgery Monitoring

Five mice were injected with 37 MBq (1 mCi) of  $^{18}\text{F}$ -FDG via the tail vein. The tracer was allowed to accumulate for 60–70 min, and the mice were imaged in the IVIS system to verify tumor uptake of  $^{18}\text{F}$ -FDG. Tumors were then imaged with the IVIS and fiber-based CLE systems after removal of the skin covering the subcutaneous tumor and after excision of the tumor. To simulate an environment mimicking surgical resection, and to validate the origin of the signal, the excised tumor was also imaged after being placed adjacent to the surgical cavity. Two images were acquired for each of these steps: 1 ambient image and 1 functional Cerenkov luminescence image. The exposure time for all ambient images was less than 1 s, and the functional image acquisition time was 5 min.

### Statistical Methods

Quantitative data were expressed as mean  $\pm$  SD. Means were compared using the Student *t* test. A 95% confidence level was chosen to determine the significance between groups, with *P* values of less than 0.05 indicating significant differences.

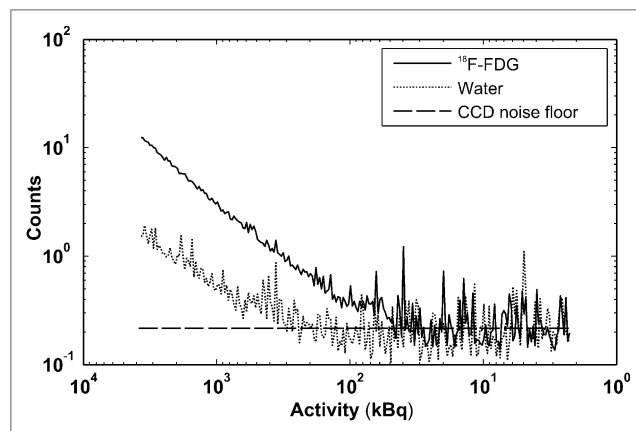


**FIGURE 2.** System sensitivity via sequential imaging of 3.7 MBq (100  $\mu$ Ci) of  $^{18}\text{F}$ -FDG for approximately 20 h. Optical signals from  $^{18}\text{F}$ -FDG and control sample were plotted.

## RESULTS

### System Characterization

Figure 2 shows the reduction in signal during  $^{18}\text{F}$ -FDG decay over time for 2 wells: 1 filled with  $^{18}\text{F}$ -FDG and 1 filled with a water and glycerol mixture only. With a 5-min integration time, a minimum of approximately 45 kBq (1.21  $\mu$ Ci) of activity can be identified as different from the control well containing the water and glycerol solution (signal-to-noise ratio  $> 1$ ). There was a decrease in signal in the control well due to stray  $\gamma$ -photons from the  $^{18}\text{F}$ -FDG well interacting with the optical fiber and creating scintillation background light in the image.

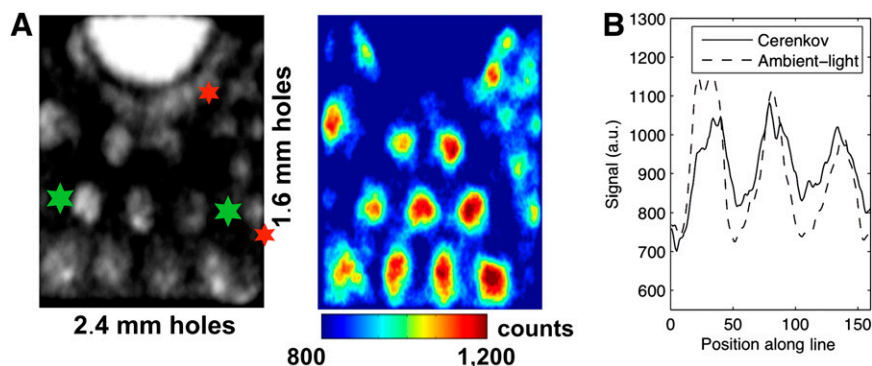
Visually, the photographic and Cerenkov images taken using the standard IVIS imaging system (Supplemental Fig. 2) are similar to the photographic and Cerenkov images taken with the fiber-based system (Fig. 3A). The line profiles demonstrate a high correlation between the Cerenkov and photographic line profiles. For the 2.4-mm holes (Fig. 3B), the line profile limits depicted by the large green stars in Figure 3A had a Pearson correlation coefficient of 0.78 (significance,  $P < 1e-5$ ). For the 1.6-mm holes (Supplemental Fig. 3), the line profile limits depicted by the smaller red stars had a Pearson correlation coefficient of 0.71 (significance,  $P < 1e-5$ ). The peaks were also in near-identical locations; the difference in peak locations between the holes for the line profiles of the photographic and Cerenkov-emission images was 3.8%, a difference of only a few pixels.

### System Demonstration

The images comparing both systems before removal of the tumor for mouse 1 are shown in Figure 4 (IVIS system [Fig. 4A] and fiber-based CLE system [Fig. 4B]). Figure 5A shows the images produced by the IVIS system, and Figure 5B shows images from the fiber-based CLE system after removal of the tumor in mouse 1.

Comparing images in Figure 5B quantitatively, we determined the tumor-to-background ratio for the Cerenkov signal by computing the ratio of the median value in the

**FIGURE 3.** Characterization of fiberoptic system spatial resolution. (A) Respective ambient (left) and Cerenkov images (right) of PET/SPECT phantom (4.3-cm inner diameter). (B) Quantitative line profiles of ambient and Cerenkov images for 2.4-mm holes; line sampled is indicated by green stars in A. a.u. = arbitrary units.



region of interest encircling the excised tumor to the median value in the cleared tumor cavity. This ratio was 1.28 (for comparison, the tumor-to-background ratio from the IVIS system was 1.16 for the 3-min scan). For mice 2, 3, 4, and 5, the tumor-to-background ratios for the removed tumor were 1.41, 1.21, 1.02, and 1.17, respectively. Tumor tissue light emission was significantly higher than the exposed cavity for all mice (Student *t* test for paired samples,  $P < 0.05$  for all). Much of the low tumor-to-background value in mouse 4 can be explained by the reflection of the light emitted from the tumor by the tumor cavity, which was directly adjacent. Residual tumor tissue after surgery is also possible.

## DISCUSSION

In this study, we demonstrated the methodology and performance of an optical fiber system built to image tumor margins during surgical resection. Cerenkov imaging has been proposed for small-animal drug discovery and surgical guidance, yet previous studies have used an imaging box with a lens-mounted imaging system; this setup is not realistic for subjects that are larger (e.g., large animals and humans). We recently demonstrated the feasibility of endoscopic imaging of Cerenkov light using conventional optical fiber bundle/clinical endoscopes, an optical imaging lens system, and a sensitive low-noise CCD camera (20). Hereby, for the first time we investigated a Cerenkov endoscope for surgical resection. We have shown that this system is capable of imaging 1.2-mm structures, using phantom experiments. We determined the sensitivity of the system for  $^{18}\text{F}$ -FDG ( $\sim 45 \text{ kBq}$  [ $1.21 \mu\text{Ci}$ ]/ $300 \mu\text{L}$ ). We then demonstrated the ability to visualize the accumulation of  $^{18}\text{F}$ -FDG in a tumor using this system and could track the contrast as the tumor was excised from the mouse.

A benefit of a Cerenkov endoscope is that it provides higher image spatial resolution than PET and SPECT cameras, because the optical photons emitted from the tissue surface are detected with optical lenses and a high-resolution CCD chip. Cho et al. demonstrated a limit of  $350 \mu\text{m}$  (in full width at half maximum) with a system designed for visualizing a microfluidic chip setup (21). This resolution is affected by the imaging system, the range of the  $\beta$ -particles in the tissue, and tissue optical

scatter. Levin and Hoffman showed that the mean  $\beta$ -particle track of  $^{18}\text{F}$ -FDG had a full width at half maximum value of  $102 \mu\text{m}$  in water (22), which determines the physical resolution limit of a Cerenkov scope when imaging  $^{18}\text{F}$ -FDG. Improved resolution may be achieved using a radioisotope with a  $\beta$ -particle decay of lower energy, such as  $^{131}\text{I}$ , although this would result in lower sensitivity because there is an inverse relationship between resolution and sensitivity. We do note some inconsistency in the image of the 1.2-mm holes, but many of these holes are clearly visualized. The high spatial resolution of the system requires accurate focus of the optics both at the distal fiber-lens junction and at the proximal fiber-camera junction—an optical focus that will be improved in our further

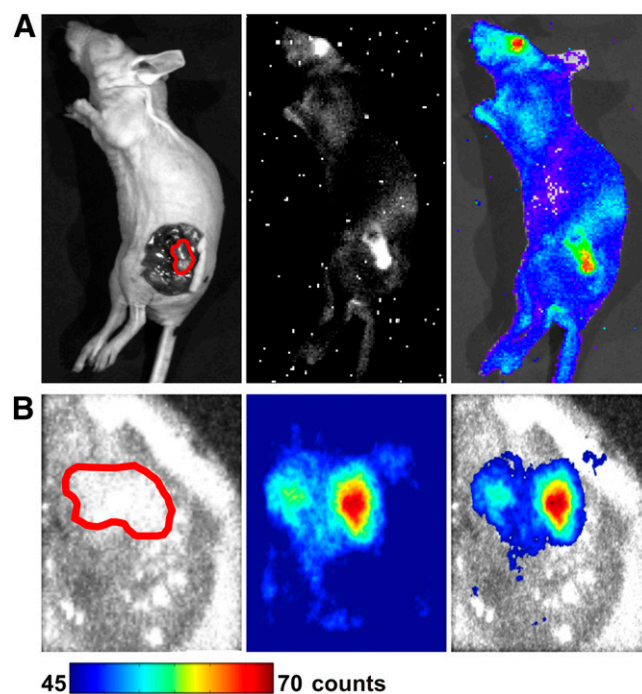


**FIGURE 4.** Mouse 1 bearing C6 glioma after tail-vein administration of  $37 \text{ MBq}$  ( $1 \text{ mCi}$ ) of  $^{18}\text{F}$ -FDG. (A) Mouse was imaged by commercially available optical IVIS system, and images were compared with those from prototype fiber-based system (B). Tumor tissues are outlined by red lines. Ambient-light images are on left, luminescent images are in middle, and fused images are on right.

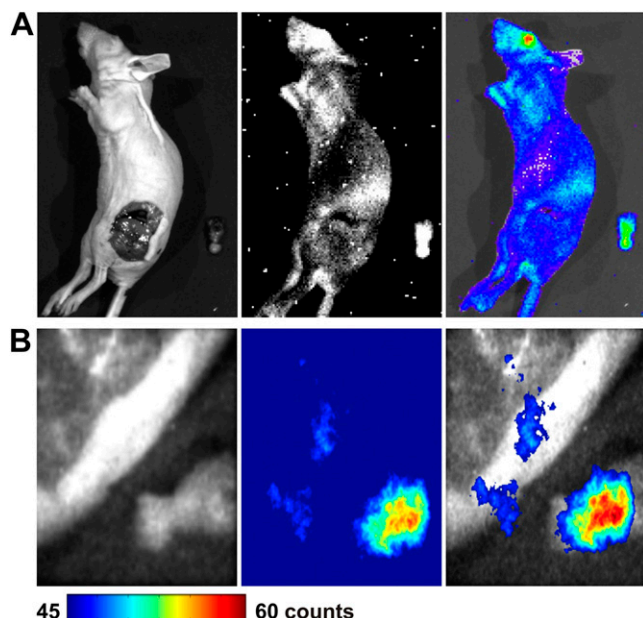


**FIGURE 5.** Mouse 1 was imaged by IVIS optical system (A) and fiber-based system (B) after surgery to remove tumor tissues. Ambient-light images are on left, luminescent images are in middle, and fused images are on right.

studies. In the case of our phantom, the resolution of the Cerenkov luminescence images was also degraded by reflections within the translucent phantom and the signal-to-noise ratio of the single-photon-counting camera, which was not entirely optimized. The signal-to-noise ratio of our ambient-light image was also affected by a slightly imperfect focus and the suboptimal settings of the illumination source and camera. Thus, although we demonstrated the ability to visualize many of these 1.2-mm cylindric holes in a phantom with this endoscope-based system, we expect to be able to image submillimeter lesions with a more optimized system.

The sensitivity limit of this system was 45 kBq (1.2  $\mu$ Ci)/300  $\mu$ L with  $^{18}\text{F}$ -FDG. To put this in a practical perspective, if this system were used for head and neck tumors of the oropharynx (with a standardized uptake value of 5.17), 2.1 GBq (54 mCi) would have to be injected intravenously into a 70-kg patient to have enough activity to visualize a 300- $\mu$ g tumor (23) in a 5-min scan; a more sensitive scope would enable the identification of smaller structures or similar structures with a reduction in ionizing dose to the patient and clinical staff. Increased sensitivity may be realized with more sensitive optics (such as an F/0.95 lens) or fiber optic glass, which transmits farther into the violet and ultraviolet emissions. The fiberglass used in this experiment was Schott-75 glass, which transmits 40% light at 500 nm; thus, it is not optimized for detecting the short-wavelength-dominant Cerenkov emission. In addition,  $\gamma$ -photons emitted from the radiotracer scintillate impurities in the glass, resulting in undesired background noise. The use of fused silica, which is much more sensitive

to the ultraviolet and violet emissions and has fewer impurities, would improve sensitivity.

As a prototype device, the off-the-shelf optical lens on this system was too large (3-cm diameter) for many endoscopic or laparoscopic applications. However, smaller custom optics could be designed to enable imaging through smaller apertures. Meanwhile, optimized optic lenses and fibers can provide better sensitivity and shorter integration time in upcoming systems. We leave this investigation for future studies using more customized optical systems.

The main advantage of this system over other optical techniques, such as fluorescence imaging, is that it is able to use standard PET tracers, such as  $^{18}\text{F}$ -FDG, which are already available in the clinic. Many novel tracers such as 3'-deoxy-3'- $^{18}\text{F}$ -fluorothymidine, engineered proteins, and labeled arginine-glycine-aspartic acid peptides are in the pipeline of clinical trials required by the Food and Drug Administration because of their utility in PET. This is a significant advantage for this technique, because much effort and innovation is being dedicated to PET tracers. In contrast, because of the lack of a standardized imaging device for optical imaging, optical contrast agents are not being sufficiently developed to keep pace with radiotracers. Thus, the main advantage of a Cerenkov emission surgical scope is that it is readily clinically translatable. The combination of PET and Cerenkov imaging provides an opportunity to use an identical signal origin, and perhaps an identical injection, to localize tumors for excision.

## CONCLUSION

This proof-of-concept study demonstrated the feasibility of using fiber-based CLE for the detection of tumor tissue in vivo and demonstrated its potential use for image-guided surgery. With further improvement in imaging sensitivity and resolution of the current system, it is expected that Cerenkov imaging might soon be translated into clinical applications.

## DISCLOSURE STATEMENT

The costs of publication of this article were defrayed in part by the payment of page charges. Therefore, and solely to indicate this fact, this article is hereby marked "advertisement" in accordance with 18 USC section 1734.

## ACKNOWLEDGMENTS

We acknowledge support from the National Cancer Institute (NCI) (R01 CA128908), the National Institutes of Health (ICMIC P50CA114747), the Department of Defense Breast Cancer Postdoctoral Fellowship (W81XWH-11-1-0087, W81XWH-11-1-0070, and W81XWH-10-1-0506), the Center for Biomedical Imaging at Stanford, the Canary Foundation, and the Friends for an Earlier Breast Cancer Test. No other potential conflict of interest relevant to this article was reported.

## REFERENCES

1. Xu Y, Liu H, Cheng Z. Harnessing the power of radionuclides for optical imaging: Cerenkov luminescence imaging. *J Nucl Med*. 2011;52:2009–2018.
2. Lucignani G. Cerenkov radioactive optical imaging: a promising new strategy. *Eur J Nucl Med Mol Imaging*. 2011;38:592–595.
3. Massoud TF, Gambhir SS. Molecular imaging in living subjects: seeing fundamental biological processes in a new light. *Genes Dev*. 2003;17:545–580.
4. Liu H, Ren G, Miao Z, et al. Molecular optical imaging with radioactive probes. *PLoS ONE*. 2010;5:e9470.
5. Robertson R, Germanos MS, Li C, Mitchell GS, Cherry SR, Silva MD. Optical imaging of Cerenkov light generation from positron-emitting radiotracers. *Phys Med Biol*. 2009;54:N355–365.
6. Boschi F, Calderan L, D'Ambrosio D, et al. In vivo  $^{18}\text{F}$ -FDG tumour uptake measurements in small animals using Cerenkov radiation. *Eur J Nucl Med Mol Imaging*. 2011;38:120–127.
7. Ruggiero A, Holland JP, Lewis JS, Grimm J. Cerenkov luminescence imaging of medical isotopes. *J Nucl Med*. 2010;51:1123–1130.
8. Liu H, Ren G, Liu S, et al. Optical imaging of reporter gene expression using a positron-emission-tomography probe. *J Biomed Opt*. 2010;15:060505.
9. Jeong SY, Hwang MH, Kim JE, et al. Combined Cerenkov luminescence and nuclear imaging of radioiodine in the thyroid gland and thyroid cancer cells expressing sodium iodide symporter: initial feasibility study. *Endocr J*. 2011;58:575–583.
10. Liu H, Zhang XF, Xing BG, Han PZ, Gambhir SS, Cheng Z. Radiation-luminescence-excited quantum dots for in vivo multiplexed optical imaging. *Small*. 2010;6:1087–1091.
11. Dothager RS, Goiffon RJ, Jackson E, Harpstrite S, Piwnica-Worms D. Cerenkov radiation energy transfer (CRET) imaging: a novel method for optical imaging of PET isotopes in biological systems. *PLoS ONE*. 2010;5:e13300.
12. Lewis MA, Kodibagkar VD, Oz OK, Mason RP. On the potential for molecular imaging with Cerenkov luminescence. *Opt Lett*. 2010;35:3889–3891.
13. Sun C, Pratz G, Carpenter CM, et al. Synthesis and radioluminescence of PE-Gylated  $\text{Eu}(3+)$ -doped nanophosphors as bioimaging probes. *Adv Mater*. 2011;23:H195–H199.
14. Holland JP, Normand G, Ruggiero A, Lewis JS, Grimm J. Intraoperative imaging of positron emission tomographic radiotracers using Cerenkov luminescence emissions. *Mol Imaging*. 2011;10:177–186.
15. Park JC, An GI, Park SI, et al. Luminescence imaging using radionuclides: a potential application in molecular imaging. *Nucl Med Biol*. 2011;38:321–329.
16. Hu Z, Liang J, Yang W, et al. Experimental Cerenkov luminescence tomography of the mouse model with SPECT imaging validation. *Opt Express*. 2010;18:24441–24450.
17. Li C, Mitchell GS, Cherry SR. Cerenkov luminescence tomography for small-animal imaging. *Opt Lett*. 2010;35:1109–1111.
18. Spinelli AE, Kuo C, Rice BW, et al. Multispectral Cerenkov luminescence tomography for small animal optical imaging. *Opt Express*. 2011;19:12605–12618.
19. Xu Y, Chang E, Liu H, Jiang H, Gambhir SS, Cheng Z. Proof-of-concept study of monitoring cancer drug therapy with Cerenkov luminescence imaging. *J Nucl Med*. 2012;53:312–317.
20. Kothapalli SR, Liu H, Liao JC, Cheng Z, Gambhir SS. Endoscopic imaging of Cerenkov luminescence. *Biomed Opt Express*. 2012;3:1215–1225.
21. Cho JS, Taschereau R, Olma S, et al. Cerenkov radiation imaging as a method for quantitative measurements of beta particles in a microfluidic chip. *Phys Med Biol*. 2009;54:6757–6771.
22. Levin CS, Hoffman EJ. Calculation of positron range and its effect on the fundamental limit of positron emission tomography system spatial resolution. *Phys Med Biol*. 1999;44:781–799.
23. Allal AS, Slosman DO, Kebdani T, Allaoua M, Lehmann W, Dulguerov P. Prediction of outcome in head-and-neck cancer patients using the standardized uptake value of 2-[ $^{18}\text{F}$ ]fluoro-2-deoxy-d-glucose. *Int J Radiat Oncol Biol Phys*. 2004;59:1295–1300.